UNIVERSIDADE FEDERAL DE UBERLÂNDIA

VINICIUS FAGUNDES DOS SANTOS

Numerical analysis of the effects brought by a twisted tape insert in elbow erosion

Uberlândia – MG – Brasil

07 de Fevereiro de 2018

VINICIUS FAGUNDES DOS SANTOS

Numerical analysis of the effects brought by a twisted tape insert in elbow erosion

Dissertação apresentada ao Programa de Pós-Graduação em Engenharia Mecânica da Universidade Federal de Uberlândia, como parte dos requisitos para a obtenção do título de **MESTRE EM ENGENHARIA MECÂNICA**.

Área de concentração: Transferência de Calor e Mecânica dos Fluidos

Universidade Federal de Uberlândia – UFU

Faculdade de Engenharia Mecânica

Programa de Pós-Graduação

Supervisor: Prof. Dr. Francisco José de Souza

Uberlândia – MG – Brasil

07 de Fevereiro de 2018

Dados Internacionais de Catalogação na Publicação (CIP)
Sistema de Bibliotecas da UFU, MG, Brasil.

S237n 2018

Santos, Vinicius Fagundes dos, 1990
Numerical analysis of the efects brought by a twisted tape insert in elbow erosion / Vinicius Fagundes dos Santos. - 2018.
112 f. : il.

Orientador: Francisco José de Souza.
Dissertação (mestrado) - Universidade Federal de Uberlândia, Programa de Pós-Graduação em Engenharia Mecânica.
Disponível em: http://dx.doi.org/10.14393/ufu.di.2018.135
Inclui bibliografia.

1. Engenharia mecânica - Teses. 2. Erosão - Teses. 3. Acoplamentos - Teses. 4. Partículas - Impactos - Teses. I. Souza, Francisco José de. II. Universidade Federal de Uberlândia. Programa de Pós-Graduação em Engenharia Mecânica. III. Título.

CDU: 621

Angela Aparecida Vicentini Tzi Tziboy – CRB-6/947

SERVIÇO PÚBLICO FEDERAL
MINISTÉRIO DA EDUCAÇÃO
UNIVERSIDADE FEDERAL DE UBERLÂNDIA
FACULDADE DE ENGENHARIA MECÂNICA
PROGRAMA DE PÓS-GRADUAÇÃO EM ENGENHARIA MECÂNICA

ALUNO: Vinícius Fagundes dos Santos

NÚMERO DE MATRÍCULA: 11612EMC015

ÁREA DE CONCENTRAÇÃO: Transferência de Calor e Mecânica dos Fluidos

LINHA DE PESQUISA: Dinâmica dos Fluidos e Transferência de Calor

PÓS-GRADUAÇÃO EM ENGENHARIA MECÂNICA: NÍVEL MESTRADO

TÍTULO DA DISSERTAÇÃO:

"Numerical analysis of the effects brought by a twisted tape insert in elbow erosion"

ORIENTADOR: Prof. Dr. Francisco José de Souza

A Dissertação foi **APROVADA** em reunião pública, realizada no Auditório Laboratório de Mecânica dos Fluidos, Bloco 5P, Campus Santa Mônica, em 07 de fevereiro de 2018, às 14 horas, com a seguinte Banca Examinadora:

NOME	ASSINATURA
Prof. Dr. Francisco José de Souza (Orientador)	UFU
Prof. Dr. Washington Martins da Silva Jr.	UFU
Prof. Dr. Henry França Meier	FURB
Prof. Dr. Carlos Antonio Ribeiro Duarte	UFG

Uberlândia, 07 de fevereiro de 2018

VINICIUS FAGUNDES DOS SANTOS

Numerical analysis of the effects brought by a twisted tape insert in elbow erosion

Dissertação apresentada ao Programa de Pós-Graduação em Engenharia Mecânica da Universidade Federal de Uberlândia, como parte dos requisitos para a obtenção do título de **MESTRE EM ENGENHARIA MECÂNICA**.

Área de concentração: Transferência de Calor e Mecânica dos Fluidos

Trabalho aprovado. Uberlândia – MG – Brasil, 07 de fevereiro de 2018:

Prof. Dr. Francisco José de Souza
Orientador - UFU

Prof. Dr. Washington Martins da Silva Jr,
UFU

Prof. Dr. Carlos Antônio Ribeiro Duarte,
UFG

Prof. Dr. Henry França Meier,
FURB

Uberlândia – MG – Brasil
07 de Fevereiro de 2018

To the most important persons in my life my father José, my mother Maria and my brothers.

Acknowledgements

This thesis would not have been possible without the inspiration and support of a number of wonderful individuals — my thanks and appreciation to all of them for being part of this journey and making this thesis possible.

First and foremost I offer my sincerest gratitude to my supervisor, Prof. Dr. Francisco José de Souza, whose expertise, understanding, and patience, added considerably to my graduate experience when I started in the research field. In the present thesis, he supported me with his patience and knowledge whilst allowing me the room to work in my own way. I appreciate his vast knowledge and skill in many areas and his assistance in writing reports (i.e., publications, conference papers and this dissertation). I can say for sure that one simply could not wish for a better or friendlier supervisor.

I thank my fellow lab mates at MFLab[1]: MSc. Bruno Tadeu, Msc. João Rodrigo and Msc. Carlos Antonio, for the stimulating discussions. However, I am indebted to Carlos Antonio for sharing his knowledge in numerical simulation applied to erosion, helped me get on the road to LATEX and provided an experienced ear for my doubts about writing a thesis and papers. These individuals always helped me to keep my life in context. Became a master is not the most important thing in life, but good friends, good times and happiness are.

My deep and sincere gratitude to my family for their continuous and unparalleled love, help and support. I am grateful to my brothers for always being there for me as a friend. I am forever indebted to my parents for giving me the opportunities and experiences that have made me who I am. They selflessly encouraged me to explore new directions in life and seek my own destiny. This journey would not have been possible if not for them, and I dedicate this milestone to them.

In conclusion, I recognize that this research would not have been possible without the financial assistance of Petróleo Brasileiro (PETROBRAS[2]), the National Council for Scientific and Technological Development (CNPq[3]) , the Federal University of Uberlândia and the Department of Mechanical Engineering, and express my gratitude to those agencies.

[1] MFLAB:<http://mflab.mecanica.ufu.br>
[2] PETROBRAS <http://www.petrobras.com.br/>
[3] CNPq <http://cnpq.br/>

"The true sign of intelligence is not knowledge but imagination."

Albert Einstein

Abstract

Due to the ongoing problem related to erosion caused by the impingement of solid particles in many engineering fields, parts such elbows, for instance, are particularly prone to erosion issues. In this work, the insertion of a twisted tape at different positions upstream of a bend is investigated numerically with the intent of reducing the elbow erosion. To ensure the reliability of the numerical calculations, experimental data were used to validate the CFD model for the standard elbow. Subsequently, simulations considering one, two and four-way coupling were evaluated for both the standard and the twisted tape-equipped elbows. Simulations were run to evaluate the average particle impact angle, impact frequency and impact velocity and the penetration ratio for each geometry. The present work used the finite-volume, unstructured code UNSCYFL3D, which solves the gas flow using the fully coupled Euler-Lagrange approach. The two-layer k-epsilon was used to model turbulence effects. Interestingly, it was found that the swirling motion imparted to the particles by the twisted tape reduces the maximum penetration ratio in the bend. Another important finding is that the farther the insert is placed upstream of the elbow, the lower the erosion in the elbow, although the tape itself becomes more prone to erosion. In general, it was noticed that the fluid-particle and particle-particle interactions are very important and cannot be neglected. Consequently, depending on the mass loading and geometry configuration, elbow erosion can be dramatically reduced.

Key-words: Twisted tape, Elbow erosion, Four-way coupling, Interparticle collisions, Erosion mitigation.

Resumo

Devido ao problema permanente relacionado à erosão provocada pelo choque de partículas sólidas em muitos campos da engenharia, peças como cotovelos de curvas , por exemplo, são particularmente propensos a problemas de erosão. Neste trabalho, a inserção de uma fita torcida em diferentes posições a montante de uma curva é investigada numericamente com a intenção de reduzir a erosão no cotovelo. Para assegurar a confiabilidade dos cálculos numéricos, dados experimentais foram utilizados para validar o modelo de CFD para o cotovelo padrão. Posteriormente, foram realizadas simulações considerando o acoplamento de uma, duas e quatro vias avaliando a curva padrão e as geometrias equipadas com a fita torcida. Foram feitas simulações para avaliar o ângulo de impacto médio de partícula, a frequência de impacto e velocidade de impacto e a taxa de penetração para cada geometria. O presente trabalho utilizou o código de volumes finitos UNSCYFL3D, que resolve o escoamento de gás usando a abordagem de Euler-Lagrange totalmente acoplada. O modelo k-epsilon duas camadas foi usado para modelar os efeitos de turbulência. Curiosamente, verificou-se que o movimento rotativo conferida às partículas pela fita torcida reduz a razão máxima de penetração na curva. Outra descoberta importante é que quanto mais a montante do cotovelo a inserção é colocado, menor a erosão no cotovelo, embora a própria fita se torna mais propensas a erosão. Em geral, observou-se que as interações de fluido-partícula e partícula-partícula são muito importantes e não podem ser negligenciadas. Por conseguinte, dependendo da carga mássica e configuração geométrica a erosão no cotovelo pode ser drasticamente reduzida.

Palavras-chaves:Fita torcida, Erosão em cotovelos, Quatro-vias de acoplamento, Colisões entre partículas, Mitigação da erosão.

List of Figures

List of Tables

List of abbreviations and acronyms

CFD	Computational Fluid Dynamics
ASTM	American Society for Testing and Materials
DES	Detached Eddy Simulation
DNS	Direct Numerical Simulation
FVM	Finite Volume Method
LES	Large Eddy Simulation
MFlab	Laboratory of Fluid Mechanics
NSE	Navier Stokes Equation
NPS	Nominal Pipe Size
PETROBRAS	Petróleo Brasileiro
RANS	Reynolds-Averaged Navier–Stokes equations
RMS	Root Mean Square
SIMPLE	Semi-Implicit Method for Pressure-Linked Equations
TKE	Turbulence Kinetic Energy

List of symbols

δ_{ij}	Kronecker delta
g_i	Gravity component

Contents

1 Introduction

Due to the nature of the conveying process, particles carried by a fluid flow is a common condition in countless engineering structures, for example: piping systems are prone to wear when abrasive particles have to be transported (*cf.* Fig. 1). With this in mind, problems related with multiphase flows nowadays receive considerable attention. In addition, a better understanding of these kind of flows can improve or even reduce some difficulties that afflict the industry.

Figure 1 – Example of worn elbow.

Source: <http://goo.gl/O9LYKR>

Based in the necessity to model and predict flows that cannot be measured without problems experimentally or it is too expensive and laborious. The develop of a new technique named Computational Fluid Dynamics (CFD) was required in the late 70s. This method consists in a subdivision of fluid mechanics that uses numerical investigation with the purposes of simulate flow through numerical procedures aimed to represent a physical phenomenon. Nowadays, with the evolution of processing power and storage of computers, the CFD became an important tool to assist researchers and engineers. Summarizing, this technique have several advantages. First of all, can reduces the time and cost in projects. Furthermore, allows the perfect understanding of fluid dynamics in the equipment and also helps in the comprehension of the phenomenon involved. As a final point, it permits

intervention in operating variables and design to reach the best solution for the problem studied optimizing single and multiphase systems.

In wear-related problems, the CFD is used as a tool for predicting the wear in various environments and due to its complexity unfeasible the use of empirical correlations.

Erosion, as defined by ASTM International G40-13 (ASTM International G40-13, 2014), is the progressive loss of the original material from a solid surface due to mechanical interaction between that surface and a fluid, a multicomponent fluid, an impinging liquid, or impinging solid particles. Nonetheless, the term erosion can be very broad generating the requirement of more specific terms. According to Crook (CROOK, 1991), erosion wear can be divided into four distinct terms, solid particle impingement erosion, slurry erosion, liquid droplet impingement erosion and cavitation erosion. Particularly in the first situation, if the hardness of the particles to be conveyed is higher than that of the system components, such as feeders and pipeline bends, then erosive wear will occur at all surfaces against which the particles impact. In many industrial processes, this type of wear arises from the impingement of solid particles against the surface and has noticeable consequences on equipment reliability and safety. While abrasive wear can be a problem in cyclone separators, propellers, pumps impellers in mineral processing systems (*cf.* Fig. 2), inlet nozzles and choke valves, it can be particularly more serious in pneumatic conveying systems (MILLS, 2003).

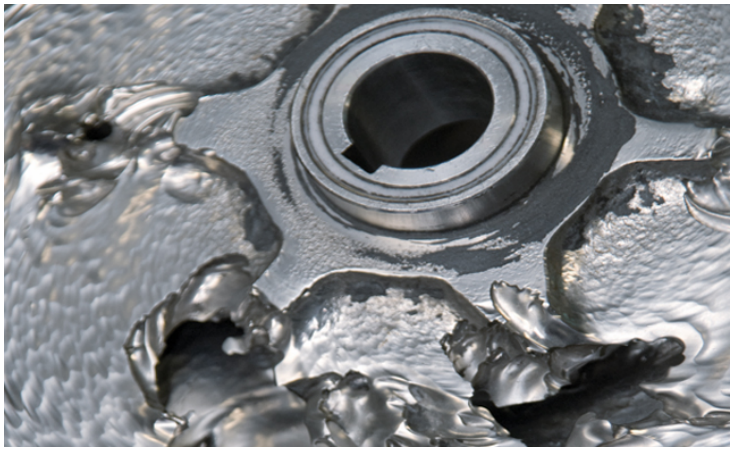

Figure 2 – Example of erosion damage on a pump impeller.

Source: <http://goo.gl/o215ln>

Generally speaking, erosive wear is a problem which industry has learned to coexist. The cost of wear (e.g.,abrasion, erosion, cavitation and others) has been estimated as ranging from 1 to 4% of the gross national product of an industrialized nation (BAYER, 2002). As can be seen in table 1, assuming the worst case of 4% for the Brazilian economy, the cost of wear are pretty high. Which implies in a necessity of more studies regarding the theme, aiming the reduction of this values .

Table 1 – Estimation of expenditure on erosion relative to Brazilian GDP

Source: <https://goo.gl/hCsZN6>

Values relative to nominal GDP		
Year	GDP(R$)	Wear expenses
2015	5,904 trillion	2.3616 billion
2014	5,521 trillion	2.2084 billion
2013	5,316 trillion	2.1264 billion
2012	4,806 trillion	1.9224 billion

As a consequence, the mitigation of the wear magnitude is also a matter of primary importance to the country's economy. Proven to be one of the critical factors for some machinery components, erosive wear is frequently a key factor in defining or restricting the proper lifetime of a component. In addition, maintenance time and operating costs are also important factors that lead companies to decide on the best method for minimizing erosion in their equipment.

The present work aims to analyze the mechanisms responsible for erosion in elbows and gaining a better understand of the effects of the twisted tape insert in pipelines systems with the focus of the research in mitigating erosion. As a consequence, implement it as a passive controller to reduce the undesirable elbow erosion.

The dissertation is organized as follows: In Chapter 2, the background theory is presented as well as an overview of the elbows studied. Chapter 3 presents an overview of the relevant equations for gas/particle phase and erosion prediction. Chapters 4 and 5 describes the type of discretization and the particle phase algorithm, respectively. Chapter 6 presents a summary of the experiments and the numerical approach applied.The dissertation is concluded in Chapter 8 and future research recommendation are given in Chapter 9.

2 Background theory

This chapter is divided in two core topics with subdivisions. Firstly, the existing types of wear mentioned in literature are presented and subsequently the focus of the work, erosion caused by particles, is shown. Afterwards, some parameters (i.e., particles mechanisms and flow influence) are described. Secondly, a brief definition of what is pipe fitting is displayed. Then, the geometries (i.e., Standard elbow and twisted tape) analyzed in the work is exposed.

2.1 Existing classes of wear

The occurrence of wear in the humblest description is the material loss and/or surface damage according to Gahr (1987). However, the fact of the explanation above sounds simplistic can deceive the reader, on the contrary of what can be expected this phenomenon is quite complex. For this reason, seeking a better understanding of this theme different classes of wear were created based on the wear mechanism.

Thus, as described in many books,(GAHR, 1987; HUTCHINGS, 1992; STACHOWIAK; BATCHELOR, 2005; BHUSHAN, 2013), there are many classes of wear but they are basically separated by the material removal mechanisms. According to Gahr (1987) it can be divide in four main classes, as shown in figure. 3, *adhesion wea*r, *abrasion wear*, *tribochemical wear* and *surface fatigue wear*.

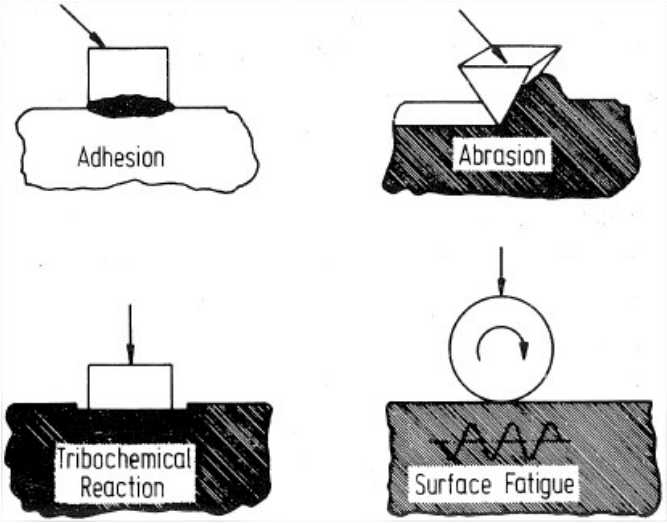

Figure 3 – Description of the four main wear mechanisms, adapted from Gahr (1987).

Nonetheless, before stating the types of wear existing, another point of view of how the wear happens is needed. According to Bhushan (2013), occurs by mechanical and/or chemical means and is usually speeded by frictional heating or some kind of thermal

means. In addition, Bhushan (2013) indicates that wear can be divided in six differents phenomenon. These are: adhesive, abrasive, fatigue, impact by erosion and percussion, chemical and electrical. However, all of them has one thing in common: the subtraction of solid material from rubbing surfaces.

Even though the division made by Gahr (1987) and Bhushan (2013) present the basis of the wear classes. There is another classification proposed by Stachowiak e Batchelor (2005). Where they come up with a dependence of wear on various operating conditions, as can be seen in figure. 4. There are twelve types of wear presented in the flowchart below, in red color: erosive, abrasive, corrosive-erosive, corrosive-abrasive, cavitational, corrosive, melting, fretting, oxidative, frictional, fatigue and fatigue-oxidative.

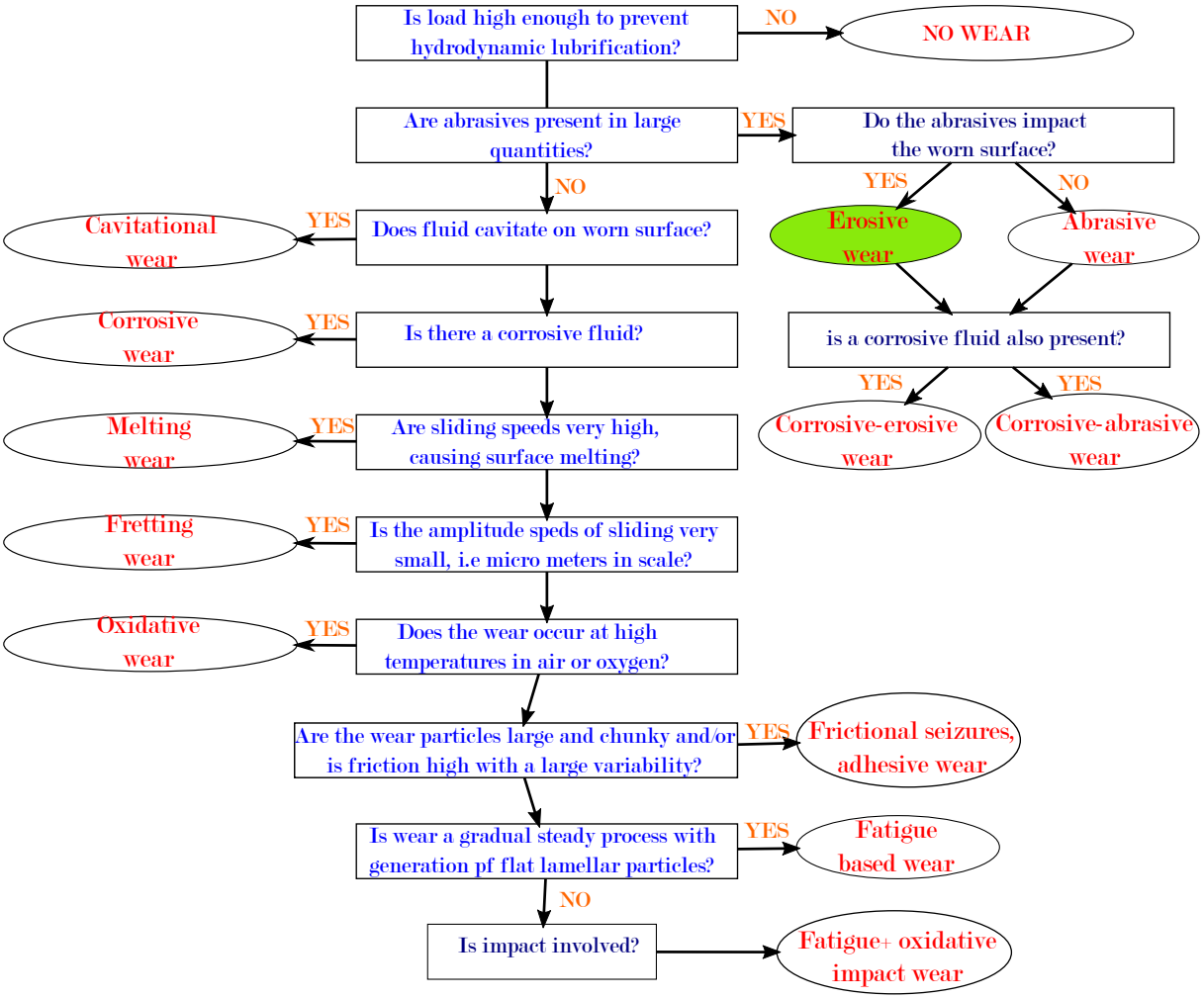

Figure 4 – Flowchart exemplifying the correlation among operating circumstances and types of wear, Adapted from Stachowiak e Batchelor (2005) .

Summarizing, all classes of wear were presented. However, in the present work only erosion wear will be discussed due to impingement of hard particles. It is well known that other kinds of wear can coexist in the same system. Nevertheless, carry out a study using more than one category of wear at the same period can considerably increase the difficulty to find precise mathematical models. With this in mind, all analyzes presented in this

work do not take into account the interference of other types of wear, which contributes to the precision of the models used in the simulation.

2.1.1 Erosion caused by particles

The characterization of erosive wear was already presented in the first chapter following the definition of ASMT. Nevertheless, the definition of this term can be found in many books, (GAHR, 1987; HUTCHINGS, 1992; STACHOWIAK; BATCHELOR, 2005; BHUSHAN, 2013), with a small difference from each other. According to Gahr (1987), in general, erosive wear is caused on a solid body by the sliding or impacting action of solid particles, liquids, gases or a combination of these. Also, it can be classified in six modes: *blast erosion*, *cavitation erosion*, *flush erosion*, *erosion-corrosion*, *rain erosion* and *thermal erosion*, as shown in figure. 5.

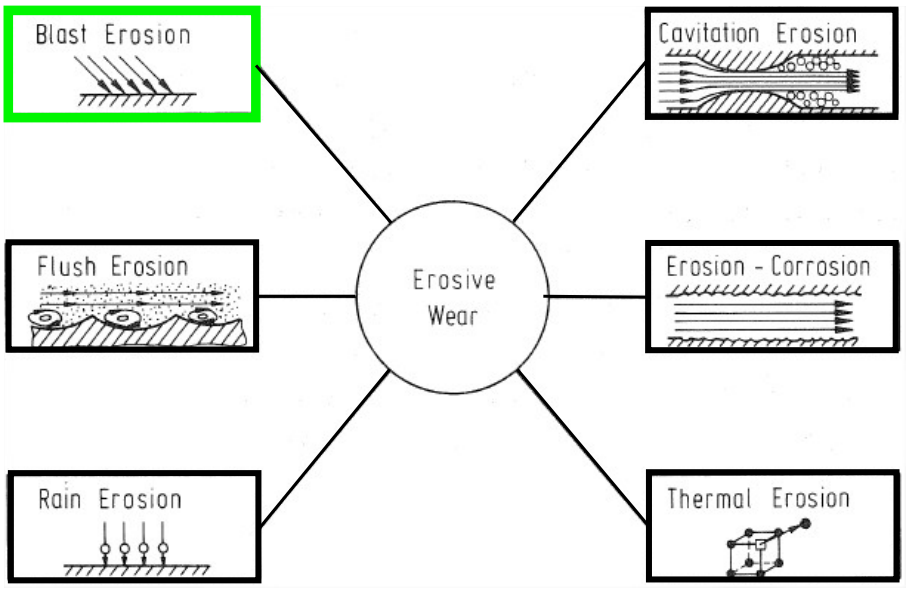

Figure 5 – Erosive wear modes, Adapted from Gahr (1987).

However, as mentioned in the previous section and the title of this section suggests, only erosion caused by solid particles will be addressed. Taking a look in figure. 5, this kind of erosion can be represented by the blast erosion. It is important to have in mind that other modes can have solid particle, but all of them are a mix of particles with another type of erosion (corrosion, cavitation and flush) and that is not the focus of this work.

Figure. 6 exemplifies a jet of particles with high velocity impacting against a surface, this schematic can be seen as a blast erosion. When particles touches the surface removes some portion of the material. In relation to period of time, the longer the exposure the greater will be the particle erosion.

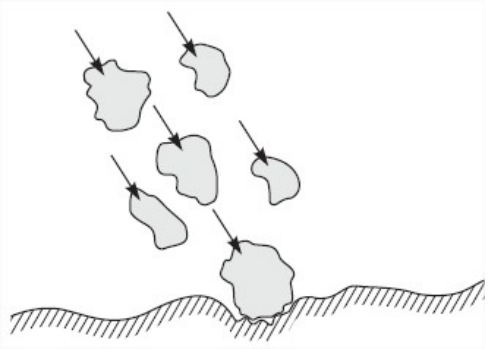

Figure 6 – Jet of abrasive particles hitting a surface at high velocity, Adapted from Bhushan (2013).

2.1.2 Erosion mechanisms

Erosive wear involves several wear mechanisms which are largely controlled by the particles material, the angle of impingement, the impact velocity, the particle size and the frequency of impact Stachowiak e Batchelor (2005). According to Stachowiak e Batchelor (2005), the known mechanisms of erosive wear are shown in figure. 7.

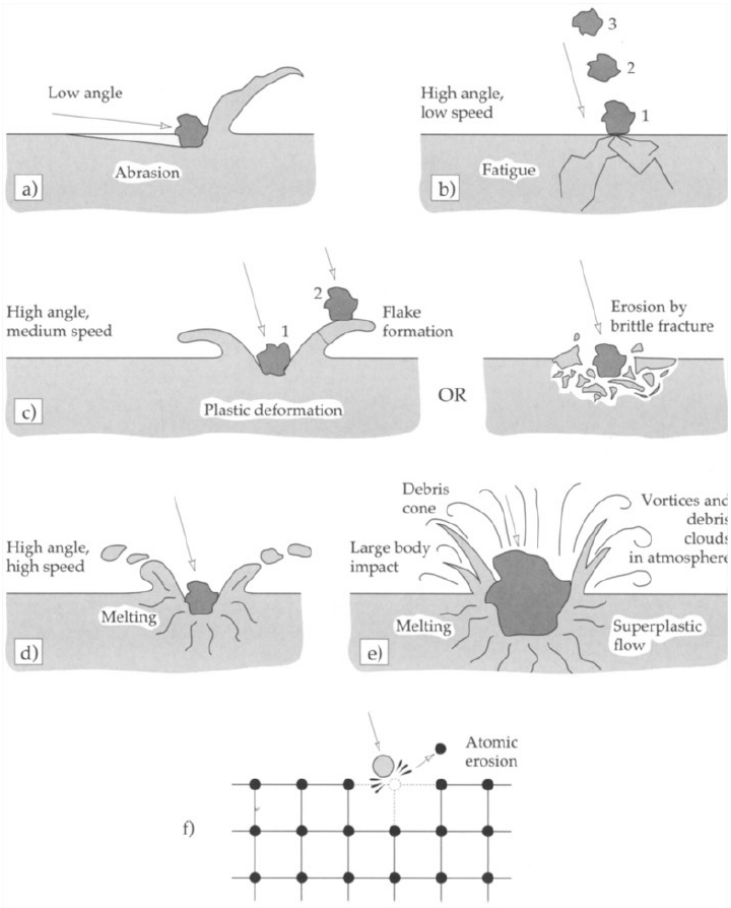

Figure 7 – Possible mechanisms of erosion: (a) abrasion at low impact angle; (b) surface fatigue; (c) brittle fracture; (d) surface melting; (e)macroscopic erosion and (f) crystal lattice degradation from impact by atoms, Adapted from Stachowiak e Batchelor (2005).

In order to understand this phenomenon, each one of the parameter mentioned in the previously paragraph will be analyzed. First, the effect of the impingement angle. Subsequent, the material and shape of the particles. Then, the impact velocity. And finally, the frequency of impact.

The angle of impingement is the angle flanked by the eroded surface and the path of the particle instantly before impact, as shown in figure. 8. A low angle of impingement favors wear process comparable to abrasion for the reason that the particles have a tendency to track across the worn surface after impact. On the other hand, a high angle of impingement causes wear mechanism which are characteristic of erosion.

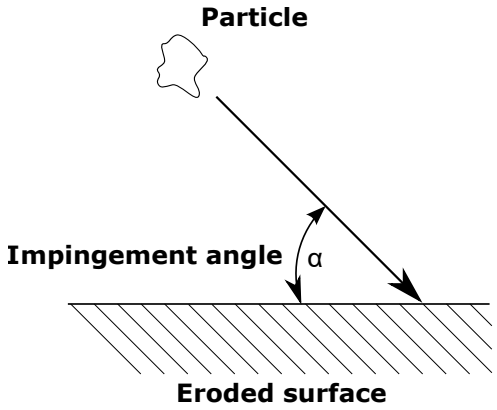

Figure 8 – Scheme of impingement angle of particle.

The behavior of the impact angle can be different in relation of the properties of the material, as can be seen in figure. 9.

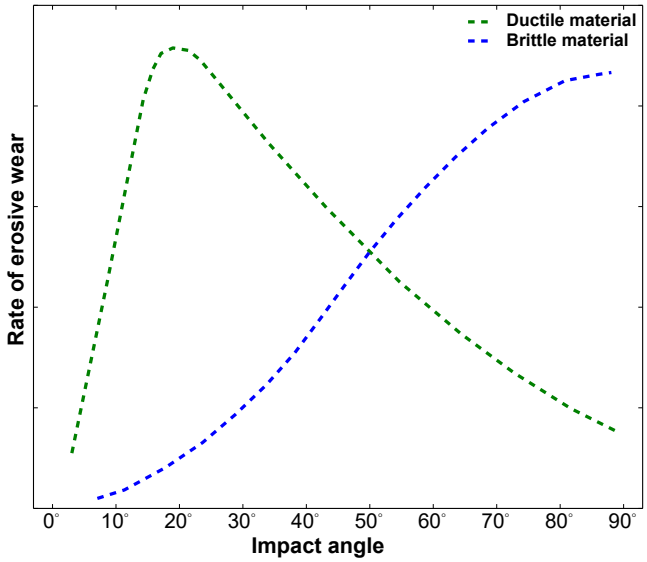

Figure 9 – Rate of erosive wear as a function of angle of impingement.

For a ductile material the highest rate of erosion occurs between 15 degrees and decreases until the lowest value in 90 degrees. In the case of brittle material the behavior

is the opposite, where the highest values of erosion occurs at an impact angle near 90 degrees and the lowest value of erosion near 0 degrees.

The velocity of the erosive particle is a very important parameters and in consequence have a strong effect in the wear process. According to Stachowiak e Batchelor (2005), at very low velocities the stresses at the impact are insufficient for plastic deformation to occur and wear proceeds by surface fatigue. In the other hand, at a high velocity the eroded material can deform plastically on the particle impact and consequently the wear occur by repetitive plastic deformation.

Particle characteristic (i.e., shape, hardness and size) are an important but relatively poorly researched aspect of the erosion problem. It is known that hard particles cause higher wear hates than soft particles. The sharpness of the particle has also been recognized as accelerating erosive wear. Both of these parameters have been included in numerical models of erosive wear. The effect of particle hardness on wear depends on the particular mode of erosive wear taking place (e.g., ductile or brittle). In the brittle mode the effect of hardness is much more pronounced than in the ductile mode Stachowiak e Batchelor (2005).

The impact frequency at which particles strike the eroded surface is one of the most significant factors to explain some parameters, such as the penetration ratio. Because the more frequently particles strike the same part of the surface, the higher will be the penetration ratio and mass loss at that location.

2.1.3 Effect of flow on erosive wear

Basically most erosive agents are conveyed by a fluid (e.g., water or air). The characteristics of the flow have a strong effect on the final erosion rate. Depending of some properties of the fluid, such as: density, viscosity and turbulence.

In order to comprehend the effects of turbulence in erosive wear, figure. 10 became necessary. Where is possible to observe that turbulent flow accelerates erosive wear, since more particles collide against the eroded surface in function of the change in the stream. In counterpart, the laminar flow tend to keep the particles parallel to the surface, as a result, retaining a lower erosion rate.

Regarding the viscosity of the fluid, the effect of the drag force caused by a different viscosity can effect wear by altering the impingement angle Stachowiak e Batchelor (2005).

Figure 11 shows four flow configurations commonly found in engineering applications. The first configuration illustrates an impinging jet, which covers a wide range of applications, representing from research configurations to abrasion machining; Figure 11b shows the flow configuration found in flows over turbine blades and turbo machinery; Figure 11c shows the flow configuration that occurs in pneumatic transport of solids and in piping;

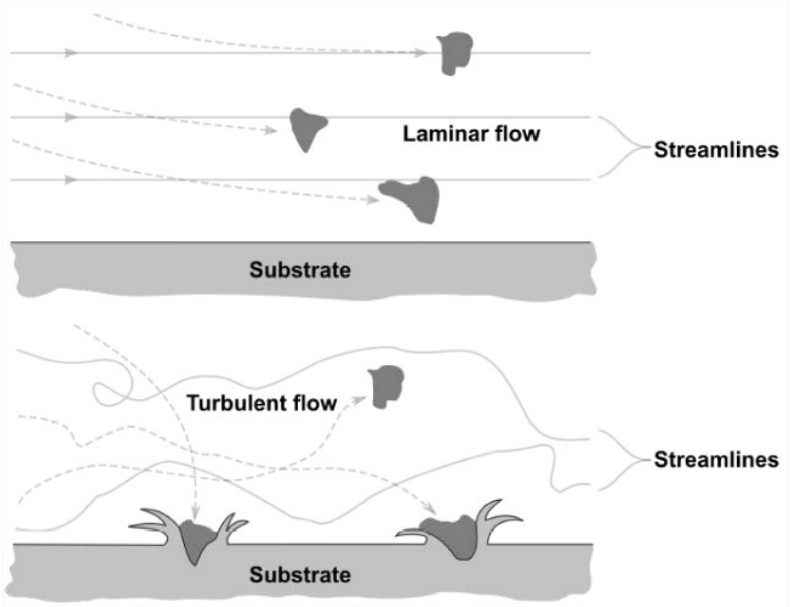

Figure 10 – Effect of flow on erosive wear, Adapted from Stachowiak e Batchelor (2005) .

Figure 11d represents the flow configuration found in heat transfer devices (HUMPHREY, 1990).

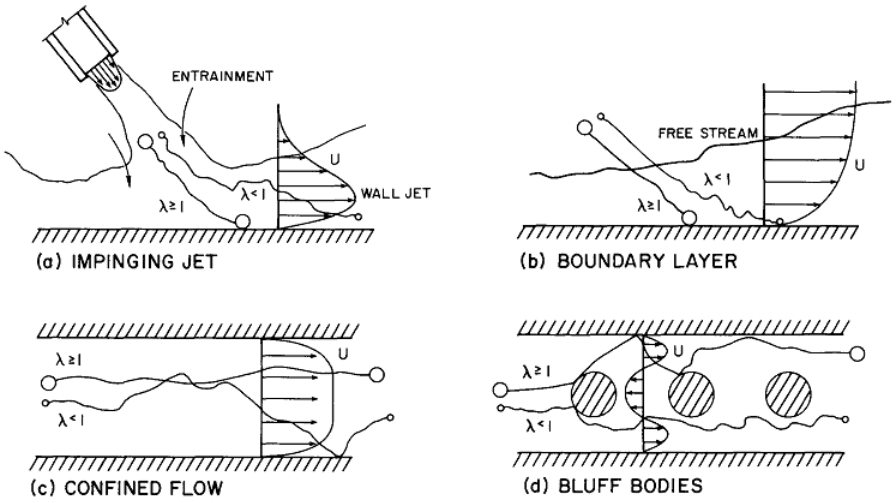

Figure 11 – Examples of flow configurations related to erosion due to impact by solid particles (HUMPHREY, 1990).

The dynamic behavior of large and small particles is interpreted briefly in Fig. 11. The ability of a particle to respond to changes imposed by the flow, and therefore, change its trajectory is characterized by the number λ, which is defined by the ratio of two time scales that characterizes the dynamics of both solid and fluid phases, respectively. In Fig. 1, this number simply represents the particle dimension; for $\lambda >> 1$, particles have high momentum and respond slowly to flow changes; on the other hand, for $\lambda << 1$, particles tend to follow the flow, being an alternative to flow visualization. This is analogous to the Stokes number, classically used in particulate systems research.

The incident velocity magnitude of a particle depends on its interaction with the fluid, with other particles, and with the wall. The behavior of these interactions depends of the flow viscous regime (laminar or turbulent), as well as the size, shape and density of particles. Interactions between particles are strongly related to the local particle concentration, potentially causing low or high concentration regions (PEREIRA et al., 2014).

2.2 Pipeline fittings

Pipe fittings are extensively required for any piping and plumbing systems used in industrial and commercial applications. Thus, fittings allow pipelines to be combined or installed in the suitable place and can be terminated or sealed anywhere. Also, fittings are available in various shapes and sizes, as shown in figure 12. Basically, they are a crucial part of piping and plumbing systems.

The basic purposes of any pipe fitting are: connect the bores of two or more pipes or tubes, connect pipe sections, connect a pipe to a different apparatus, change the direction of fluid flow, maintain or regulate the flow and close or sealing a pipe.

Figure 12 – Examples of pipe fittings.

Source: <http://vdpf.in>

In a first moment, the term piping and plumbing can be mistaken as the same thing. Although, both terms refers to tubes they are different from each other. Essentially, the term plumbing is generally used to describe conveyance of water, gas, or liquid waste in ordinary domestic or commercial environments, whereas piping is often used to describe high-performance (*e.g.*, high pressure, high flow, high temperature, hazardous materials) conveyance of fluids in specialized applications (PARISHER; RHEA, 2012). Pipe fittings are

commonly used in flow systems and can strongly influence flow (DESHPANDE; BARIGOU, 2001).

Even though several types of pipe fitting has been used in industries, only two types will be discussed in the present work, which is the standard elbow and an inserted elbow with a twisted tape. Both types are explained in the following sections.

2.2.1 Standard elbow

Piping Elbows and Bends are very significant pipe fitting (described in the previous section) which are used very often for altering course in piping system. It is essential to have in mind that the term elbow and bend are not the same, even though sometimes these two terms are interchangeably used. A bend is simply a generic term in piping for an “offset” – a change in direction of the piping. It signifies that there is a “bend” i.e, a change in direction of the piping but it lacks specific, engineering definition as to direction and degree. Bends are usually made by using a bending machine (hot bending and cold bending) on site and suited for a specific need. Use of bends are economic as it reduces number of expensive fittings. An elbow, on the other hand, is a specific, standard, engineered bend pre-fabricated as a spool piece (based on ASME B 16.9) and designed to either be screwed, flanged, or welded to the piping it is associated with (TOBERGTE; CURTIS, 2013).

An elbow is a pipe fitting installed between two lengths of pipe or tubing to allow a change of direction, usually a 90° or 45° angle. A 90 degree elbow (Fig. 13) is also called a "90 bend" or "90 ell" but in this report the name ”standard elbow” is used in order to facilitate the treatment.

Figure 13 – Example of a 90 degree elbow.

Source: <http://goo.gl/ysJx0O>

The function of an elbow is to change direction or flow in a piping system. By default, there are 5 opportunities, the 45°, 90° and 180° elbows, all three in the "long radius" version, and in addition the 90° and 180° elbows both in the "short radius" version.

Elbows are often used in oil and gas production systems, and they cause redistribution of gas and liquid which can affect distribution of corrosion inhibitors within and downstream of the bends. Elbows are also a location susceptible to the impact of particles along the outer radius (VIEIRA et al., 2014).

2.2.2 Elbow with a twisted tape insert

There are many principles and ideas that can be used to reduce bend wear due to particles, as stated by Mills (MILLS, 2003). One of the methods is the insertion of a twisted tape, as shown in figure 14, or a spiral inside the pipe, upstream of the bend. Mills (MILLS, 2003) noticed a considerable reduction in the bend erosion, indicating that the method can be effective. Other works related to the erosion mitigation in pipelines using twisted tape insert were carried out by Ionescu (IONESCU, 2012) and Wood et al. (WOOD et al., 2001), where the authors found potential benefits generated by the swirl created by the insert. In 2013, Kadyirov (KADYIROV, 2013) investigated only the swirl flow in detail. On the other hand, inserts are commonly used in heat transfer equipments (KANIZAWA et al., 2016; BHUIYA et al., 2013; ZHANG et al., 2016) to improve heat transfer rates.

Figure 14 – Example of a twisted tape in pipe.

Source: <http://goo.gl/gk5XvO>

Despite the apparent benefits of the twisted tape insert, there is virtually no data on its performance in the open literature related to erosion in elbows. Thus, the main goal of this work is to quantitatively investigate the erosion reduction brought about by the

twisted tape placed at four different positions upstream of the bend. The standard elbow at the same mass loading is used as a reference. The effects of the insert are studied in order to identify a potential reduction in the penetration ratio in the bend.

By gaining a better understanding of the effects of the twisted tape insert in pipelines systems, it is possible to implement it as a passive controller to reduce the undesirable elbow erosion, besides reducing maintenance costs or even preventing more expensive measures, such as replacing the curve part worn by erosion.

3 Numerical approach

This chapter is divided in three main topics with the appropriated subdivisions. First, Section 3.1 presents the flow equations. Which describe the RANS (Reynolds averaged navier-stokes) equations of motion for the fluid and the two-layer k-epsilon turbulence model. Second, Section 3.2 shows the dispersed phase motion equations. Where the particles is approached in a Lagrandian framework and for the movement of the particulate Newton's second law are used. Finally, the employed erosion model is presented in Section 3.3. Addressing the equations used to predict the erosion, by experience of the author (SANTOS et al., 2016; DUARTE et al., 2016b; DUARTE et al., 2015; DUARTE et al., 2016a) and works carried by (PEREIRA et al., 2014) the erosion models and correlations used in this work seems to be the most accurate.

3.1 Gas phase equations

Simulations of fluids are based on the Navier Stokes Equations (NSE). In tensor notation the continuity and Cauchy momentum equation are respectively,

$$\frac{\partial \rho}{\partial t} + \frac{\partial (\rho u_i)}{\partial x_i} = 0 \tag{3.1}$$

$$\frac{\partial (\rho u_i)}{\partial t} + \frac{\partial (\rho u_i u_j)}{\partial x_j} = -\frac{\partial p}{\partial x_i} + \frac{\partial \tau_{ij}}{\partial x_j} + f_i \tag{3.2}$$

where p is the pressure, ρ is the fluid density, u_i represents the i component of the velocity vector, τ_{ij} denotes the molecular viscous tensor and f_i is the component i of the source term.

For a Newtonian fluid, where ν represents the the kinematic viscosity of the fluid, the tensor is modeled with the Stokes model of viscous stress,

$$\tau_{ij} = \nu \left(\frac{\partial u_i}{\partial x_j} + \frac{\partial u_j}{\partial x_i} \right) - \frac{2}{3} \mu \delta_{ij} \tag{3.3}$$

For the present study, an Unsteady-Reynolds-Averaged Navier-Stokes (URANS) approach is adopted in this investigation:

$$\frac{\partial (\rho u_i)}{\partial (x_i)} = 0 \tag{3.4}$$

$$\frac{\partial}{\partial t}(\rho u_i) + \frac{\partial}{\partial x_j}(\rho u_i u_j) = -\frac{\partial p}{\partial x_i} + \frac{\partial}{\partial x_j}\left[(\mu + \mu_t)\left(\frac{\partial u_i}{\partial x_j} + \frac{\partial u_j}{\partial x_i}\right)\right] + Su_{ip} + \rho g_i \qquad (3.5)$$

where ρ is the fluid density, u_i is the Reynolds-averaged velocity component, p is the mean pressure, μ the gas dynamic viscosity and μ_t is the turbulent viscosity. The additional source terms due to phase interaction is represented by Su_{ip}.

The numerical solution of the conservation equations for the momentum and turbulence, is accomplished by the computational code UNSCYFL3D (De Souza et al., 2012). This in-house tool is based on the finite volume method in unstructured three-dimensional grids. The SIMPLE (Semi-Implicit Method for Pressure-Linked Equations) algorithm is used to couple the velocity and pressure fields. The collocated arrangement is used for all variables, with the conventional Rhie-Chow interpolation scheme for the computation of the mass flow rate through each element face. The discretization procedure described above generates a linear system of equations for each variable at each element center. The biconjugate gradient and the algebraic multigrid (AMG) methods are used to efficiently solve the linear system resulting from the discretization of the conserved and turbulence properties. The main advantage of this approach is that it does not depend on the element shape, as the data structure is based on element faces. For storing the coefficients of the linear systems for the velocity components, pressure correction and turbulence variables, the CSR (Compressed Sparse Row) format is used. More details of the solution method can be found in De Souza et al. (De Souza et al., 2014).

The second-order upwind scheme was employed for the advective term, whereas the centered differencing scheme was used for the diffusive terms of the momentum equations and turbulence model equations.

The above presented set of equations allows the flow to experience turbulent behavior. Hence the flow contains turbulent kinetic energy (E) that is distributed over eddies with varying sizes. When all the turbulence is resolved, the mesh should be fine enough to capture even the smallest eddies. This technique is called Direct Numerical Simulation (DNS). However with the current available hardware this is only possible with very simple geometries and low Reynolds number flows. In order to get a clearer view of which eddies are resolved using various methods, a logarithmic plot of this energy with respect to the reciprocal of the Eddy size, the wavenumber (k), is given in Fig. 15.

From this figure it can be seen that DNS resolves all the turbulent kinetic length scales and thus all the turbulence. On the other hand RANS simulations model all the turbulence and thus non of the eddies are resolved. It can be seen that most of the kinetic energy is located in the large eddies. Large Eddy Simulation (LES) is based on this fact and resolves the large scales while the small scales are approximated using mathematical

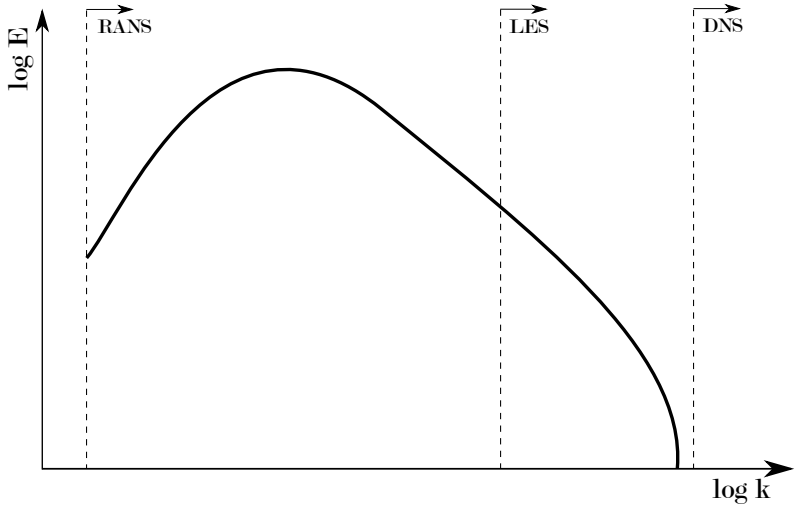

Figure 15 – The turbulent kinetic energy distributed over eddies of different sizes (FROHLICH; TERZI, 2008).

models. In some regions of a flow field, like the boundary layer, the large eddies become very small as well, requiring very small cell sizes.

For the current study, a confined flow is considered. Since high Reynolds number is present and complex flow phenomena occur, DNS is not an option for solving the flow. LES is also discarded as an option due to its high computational costs. Since RANS uses the least computational resources while still providing sufficiently accurate results, the main focus lies on this technique. The next section shows more detail about this method.

3.1.1 Turbulence model

The standard k-epsilon model is the most widely known and extensively used two-equation eddy viscosity model (BARDINA et al., 1997). It was originally developed to improve the mixing-length model and to avoid the algebraic prescription of the turbulence length scale in complex flows. Transport equations are solved for two scalar properties of turbulence, the turbulence kinetic energy, k, and its dissipation rate, epsilon:

$$\frac{\partial}{\partial t}(\rho k) + \frac{\partial(\rho u_j k)}{\partial x_j} = \frac{\partial}{\partial x_j}\left[\left(\mu + \frac{\mu_t}{\sigma_k}\right)\frac{\partial k}{\partial x_j}\right] + P - \rho\epsilon \tag{3.6}$$

$$\frac{\partial}{\partial t}(\rho \epsilon) + \frac{\partial(\rho u_j \epsilon)}{\partial x_j} = \frac{\partial}{\partial x_j}\left[\left(\mu + \frac{\mu_t}{\sigma_\epsilon}\right)\frac{\partial \epsilon}{\partial x_j}\right] + C_{\epsilon 1}\frac{\epsilon}{k}P - C_{\epsilon 2}\,\rho\,\frac{\epsilon^2}{k} \tag{3.7}$$

where P is the production term, given by:

$$P = (\mu_t + \mu)\left[\left(\frac{\partial u_i}{\partial x_j} + \frac{\partial u_j}{\partial x_i}\right)\frac{\partial u_i}{\partial x_j}\right] \tag{3.8}$$

The eddy-viscosity in the standard k-epsilon model is defined as a function of the turbulent kinetic energy and the turbulent dissipation rate as:

$$\mu_{t,standard} = C_\mu \, \rho \, \frac{k^2}{\epsilon} \tag{3.9}$$

Although widely used, the standard k-epsilon displays some weaknesses, such as the assumption that the flow is fully turbulent. To circumvent this issue, the 2-layer k-epsilon model was employed, as it can handle well both the core flow and the near wall region. Essentially, it consists in solving the standard model for the turbulent flow region and a one-equation model for the region affected by the viscosity. In the one-equation k-epsilon model, the conservation equation for k is retained, whereas epsilon is computed from:

$$\epsilon = \frac{k^{3/2}}{l_\epsilon} \tag{3.10}$$

The length scale that appears in Eq. (3.10) is computed from:

$$l_\epsilon = y \, C_l \, (1 - e^{-Re_y/A_\epsilon}) \tag{3.11}$$

In Eq. (3.11), Re_y is the turbulent Reynolds number, defined as:

$$Re_y = \frac{\rho \, y \sqrt{k}}{\mu} \tag{3.12}$$

where y is the distance from the wall to the element centers. This number is the demarcation of the two regions, fully turbulent if $Re_y > Re_y^*$, $Re_y^* = 200$ and viscosity-affected, $Re_y < 200$. For the one-equation model, the turbulent viscosity is computed from:

$$\mu_{t,2layer} = \rho \, C_\mu \, l_\mu \sqrt{k} \tag{3.13}$$

The length scale in the equation above is computed as below:

$$l_\mu = y \, C_l \, (1 - e^{-Re_y/A_\mu}) \tag{3.14}$$

In UNSCYFL3D, both the standard k-epsilon and the one-equation model described above are solved over the whole domain, and the solutions for the turbulent viscosity and the turbulence kinetic energy dissipation rate provided by both models are smoothly blended:

$$\mu_t = \lambda_\epsilon \, \mu_{t,standard} + (1 - \lambda_\epsilon) \, \mu_{t,2layer} \tag{3.15}$$

A blending function, λ_ϵ, is defined in such a way that it is equal to unity far from walls and is zero very near walls. The blending function used here is:

$$\lambda_\epsilon = \frac{1}{2}\left[1 + \tanh\left(\frac{Re_y - Re_y^*}{A}\right)\right] \tag{3.16}$$

The constant A determines the width of the blending function:

$$A = \frac{0.20\, Re_y^*}{\operatorname{artanh}(0.98)} \tag{3.17}$$

The purpose of the blending function λ_ϵ is to prevent solution divergence when the solution from both the standard and the one-equation models do not match. The constants in the length scale formulas, Eqs. (3.11) and (3.14), are taken from:

$$C_l = 0.4187\, C_\mu^{-3/4} \quad A_\mu = 70 \quad A_\epsilon = 2\, C_l \tag{3.18}$$

It is very important to refine the grid so as to have $y+ < 1$ in the first element away from the wall and ensure accurate results for the fluid flow. The models for both the fluid and particle have been validated in another publication (De Souza et al., 2012).

The analyses carried out in this work are limited to slightly swirling flows, since highly swirling flows are known to be anisotropic, thus requiring more advanced turbulence modeling (Reynolds Stress Model, for instance). The condition is met for all the cases illustrated, as the maximum swirl number (S_n) is lower than 1.0. Therefore, the 2 layer k-epsilon model, although isotropic, is expected to produce good results.

3.2 Dispersed phase motion equations

As mentioned in the previous section, the dispersed phase is treated in a Lagrangian framework, in which each particle is tracked through the domain and its equation of motion is based on Newton's second law. The trajectory, linear momentum and angular momentum conservation equations for a rigid, spherical particle can be written, respectively, as:

$$\frac{dx_{pi}}{dt} = u_{pi} \tag{3.19}$$

$$m_p \frac{du_{pi}}{dt} = m_p \frac{3\rho C_D}{4\rho_p d_p}(u_i - u_{pi}) + F_{si} + F_{ri} + \left(1 - \frac{\rho}{\rho_p}\right) m_p g_i \tag{3.20}$$

$$I_p \frac{d\omega_{pi}}{dt} = T_i \tag{3.21}$$

In the above equations, $u_i = U_i + u_i^{'}$ are the components of the instantaneous fluid velocity. The average fluid velocity U_i is interpolated from the resolved flow field, whereas the fluctuating component $u_i^{'}$ is calculated according to the Langevin dispersion model. d_p is the particle diameter and $I_p = 0.1\, m_p\, d_p^2$ is the moment of inertia for a sphere. Unlike most commercial CFD codes, UNSCYFL3D solves for the particle rotation. This is particularly important when dealing with large particles, which frequently collide with walls.

The empirical correlation proposed by Schiller and Naumann (SCHILLER; NAUMANN, 1933) is used to evaluate the drag coefficient past each particle:

$$C_D = 24\, Re_p^{-1}(1 + 0.15\, Re_p^{0.687}) \quad \text{if} \quad Re_p < 1000 \tag{3.22}$$

$$C_D = 0.44 \quad \text{if} \quad Re_p > 1000 \tag{3.23}$$

In Eqs. (3.22) and (3.23), Re_p is the particle Reynolds number $Re_p = \rho\, d_p\, |u_i - u_{pi}|/\mu$.

The calculation of the shear-induced lift force is based on the analytical result of Saffman (SAFFMAN, 1965) and extended for higher particle Reynolds numbers according to Mei (MEI, 1992):

$$F_{si} = 1.615\, d_p\, \mu\, Re_s^{1/2}\, C_{ls}\, \frac{[(u_i - u_{pi}) \times \omega_i]}{|\omega_i|} \tag{3.24}$$

$\vec{\omega}$ is the vorticity, $Re_s = \rho\, d_p^2\, |\vec{\omega}|/\mu$ is the particle Reynolds number of the shear flow and $C_{ls} = F_{ls}/F_{ls,Saff}$ represents the ratio of the extend lift force to the Saffman force:

$$C_{ls} = (1 - 0.3314\, \beta^{0.5}) e^{-0.1 Re_p} + 0.3314\, \beta^{0.5} \quad \text{if} \quad Re_p < 40 \tag{3.25}$$

$$C_{ls} = 0.0524\, (\beta\, Re_p)^{0.5} \quad \text{if} \quad Re_p > 40 \tag{3.26}$$

β is a parameter $\beta = 0.5\, Re_s/Re_p$ $(0.005 < \beta < 0.4)$.

The rotation-induced lift is computed based on the relation given by Rubinow and Keller (RUBINOW; KELLER, 1961), which was extended to account for the relative motion between particle and fluid:

$$F_{ri} = \frac{\pi}{8}\, \rho\, d_p^3\, \frac{Re_p}{Re_r}\, C_{lr}\, \frac{[\Omega_i \times (u_i - u_{pi})]}{\Omega_i} \tag{3.27}$$

In Eq. (3.27), $\Omega_i = 0.5\,\nabla_i \times u_i - \omega_{pi}$ and $Re_s = \rho\, d_p^2\, |\Omega_i|/\mu$. The lift coefficient C_{lr} is obtained from the correlation proposed by Lun and Liu (LUN; LIU, 1997):

$$C_{lr} = \frac{Re_r}{Re_p} \quad \text{if} \quad Re_p < 1 \tag{3.28}$$

$$C_{lr} = \frac{Re_r}{Re_p}\,(0.178 + 0.822\, Re_p^{-0.522}) \quad \text{if} \quad Re_p > 1 \tag{3.29}$$

Also, the rotating particle experiences torque from the fluid flow. The correlation of Rubinow and Keller (RUBINOW; KELLER, 1961) was extended to account for the relative motion between fluid and particle at higher Reynolds number:

$$T_i = C_r\, \frac{\rho\, d_p^5}{64}\, |\Omega_i|\, \Omega_i \tag{3.30}$$

The coefficient of rotation, C_r, was obtained from the following correlation, derived from and the direct numerical simulations of Dennis et al. (DENNIS, 1980):

$$C_r = \frac{64\pi}{Re_r} \quad \text{if} \quad Re_r < 32 \tag{3.31}$$

$$C_r = \frac{12.9}{\sqrt{Re_r}} + \frac{128.4}{Re_r} \quad \text{if} \quad Re_r > 32 \tag{3.32}$$

Forces such as Basset and virtual mass have been neglected. This is a reasonable assumption since the particle material density is over 1000 times the gas density (CROWE et al., 1998; C. Crowe, E. Michaelides, 2005).

Diluted flow is assumed, so that the correlations for the forces on the particles are based on a single isolated sphere. This is not expected to impact the results, because the overall mass loading of the present work is only 0.013. Even though there are some high concentration regions, the local volume fraction still remains low enough so that such correlations apply.

The extension of the Euler-Lagrange approach to unstructured meshes requires the use of accurate interpolation schemes, since in the above equations the continuous phase properties must be determined at the particle center. A few interpolation schemes have been tried out, and the best compromise between accuracy and cost was obtained with the Sheppard's scheme. Basically, the velocity and vorticity components at the particle position are calculated by weighing the neighboring element values with their inverse distances from their centers to the particle position. For integrating the ordinary differential equations (3.19), (3.20) and (3.21), the analytical scheme was used for the linear and angular velocities.

Upon a particle colliding with a wall, the new particle linear and angular velocities after rebound are calculated according to the following conservation equations (BREUER et al., 2012):

Nonsliding collision:

$$\vec{u}_p^{+} = \vec{u}_p^{-} - (1 + e_{par}) \frac{2}{7} \vec{u}_{pr}^{-} - (1 + e) (\vec{u}_p^{-} \cdot \vec{n}) \vec{n} \tag{3.33}$$

$$\vec{\omega}_p^{+} = \vec{\omega}_p^{-} - \frac{10}{7} \left(\frac{1 + e_{par}}{d_p} \right) \vec{n} \times \vec{u}_{pr}^{-} \tag{3.34}$$

Sliding collision:

$$\vec{u}_p^{+} = \vec{u}_p^{-} - (1 + e) (\vec{u}_p^{-} \cdot \vec{n}) \left[\mu_d \frac{\vec{u}_p^{-}}{|\vec{u}_p^{-}|} + \vec{n} \right] \tag{3.35}$$

$$\vec{\omega}_p^{+} = \vec{\omega}_p^{-} - \frac{5}{d_p} (1 + e) (\vec{u}_p^{-} \cdot \vec{n}) \frac{\mu_d}{|\vec{u}_p^{-}|} \vec{n} \times \vec{u}_{pr}^{-} \tag{3.36}$$

In the above equations, the superscripts $^{-}$ and $+$ denote values prior to and after the collision, respectively, e_{par} is the parallel restitution coefficient, e is the normal restitution coefficient and μ_d is the dynamic friction coefficient. $\vec{n}$ is the normal unit vector pointing outwards of the element face being impacted. $\vec{u}_{rp}$ is the relative velocity at the contact point:

$$\vec{u}_{pr} = \vec{u}_p - (\vec{u}_p \cdot \vec{n}) \vec{n} + \frac{d_p}{2} \omega_p \times \vec{n} \tag{3.37}$$

Inter-particle collisions are modeled with a stochastic, hard-sphere model. As described by Oesterle and Petitjean (OESTERLE; PETITJEAN, 1993) and Sommerfeld (SOMMERFELD, 2001), for each computational particle, a fictitious collision partner is generated, and the probability of a collision is checked based on an analogy with kinetic theory of gases. This in turn requires that the average and RMS linear and angular velocities, as well as the particle concentration in each control volume, be sampled and stored every Lagrangian calculation. Although demanding a lot of memory, the method is rather economical and effective, and avoids the use of a deterministic collision model, which is quite expensive computationally.

When a structured grid is used, it is simple to determine the element hosting the particle, as there exists a straightforward relationship between the element index and its physical location. Because an unstructured grid is used in this work, there is the need for a specific algorithm to locate the particle after its final position is calculated by the integration of Eq. (3.19). For that purpose, the particle-localization algorithm proposed

by Haselbacher et al. (HASELBACHER et al., 2007) was implemented. This algorithm is based on tracking a particle along its trajectory by computing the intersections of the trajectory and the element faces. Since it does not depend on the element topology, it is suitable for use in unstructured grids. Furthermore, it was observed to be much faster than costly, direct-search algorithms.

The coupled solution of the continuous and particle phases is summarized as follows: first the steady-state solution for the single fluid phase flow is computed. Subsequently, the unsteady-state solution is initialized and the computational particles are injected at each timestep and tracked throughout the domain. For each control volume, the average and RMS linear and angular velocities, the particle concentration and the source-terms for the fluid momentum equation are stored at each timestep. These are employed in the next time step for the fluid flow solution and inter-particle collisions. Both fluid flow and particle motion are then solved until statistical convergence is achieved. Normally, nearly four residence times are sufficient for smooth statistics.

The mass loading represented by the symbol ϕ, is presented in equation 3.38. Basically, defined as the ratio of solid phase mass flow rate ($\dot{m}_p$) to gas phase mass flow rate ($\dot{m}_f$). This relation, along with other parameters, determines the effects of the interactions between the phases.

$$\phi = \frac{\dot{m}_p}{\dot{m}_f} \tag{3.38}$$

Figure 16 shows the schematic representation of a mixture of particles dispersed in a fluid with diluted concentration, intermediate concentration and high concentration. Looking at those representations, which differ from one another is the number of particles in the domain (cube) and the classification of the mixture is based on the Lp that refers to the free distance between the particles. Consequently, minor my Lp more concentrated will be my mixture.

The density of the phases as well as the distance between particles provide essential information for determining how the dispersed phase should be treated. Depending on the mass loading, the degree of interaction between the phases can be interpreted in three different ways:

- **One-way coupling:** Very low mass loadings ($\phi << 1$). The gas phase completely influences the motion of the particles via drag and other forces and the particles do not affect the carrier fluid flow. This condition is typical for dilute suspensions.
- **Two-way coupling:** Intermediate mass loadings ($\phi \approx 1$). The gas phase influences the particle motion and particles influence back the carrier fluid by attenuating or enhancing the mean moments and turbulence effects.

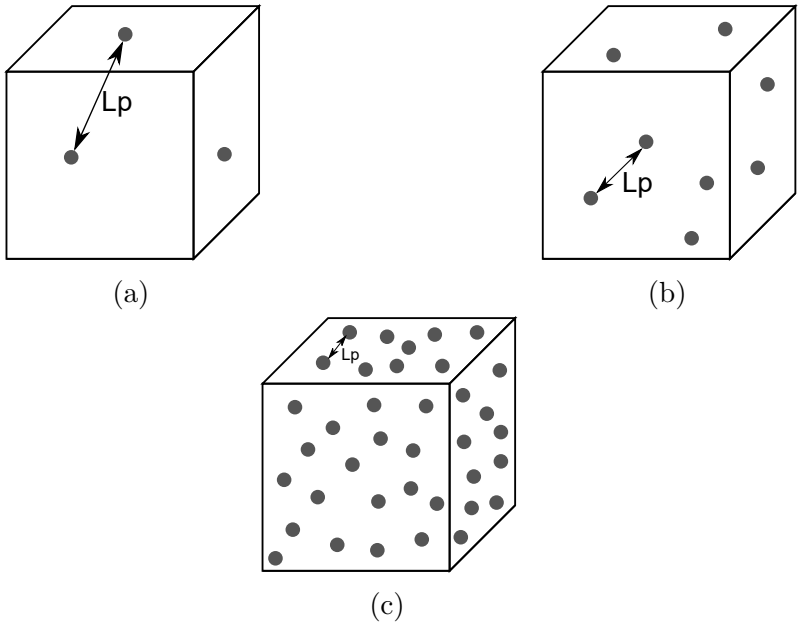

Figure 16 – Schematic representation of a mixture of particles dispersed in a fluid: (a) Diluted mixture; (b) Intermediate mixture and (c) Dense mixture.

- **Four-way coupling:** High mass loadings ($\phi >> 1$). Besides effects on the carrier fluid, particle-to-particle collisions are also relevant. Obviously, it is impossible to avoid the inter-particle collisions in an experiment, which makes it difficult to understand its consequences in a gas-solid flow, for instance. On the other hand, CFD enables the analysis of such effects, since the inter-particle collision model can be turned off.

Figure 17 presents in a schematic way how both phase (i.e., continuous and dispersed) interact with one another, summarizing the definitions given in the previously paragraphs of one-way, two-way and four-way coupling.

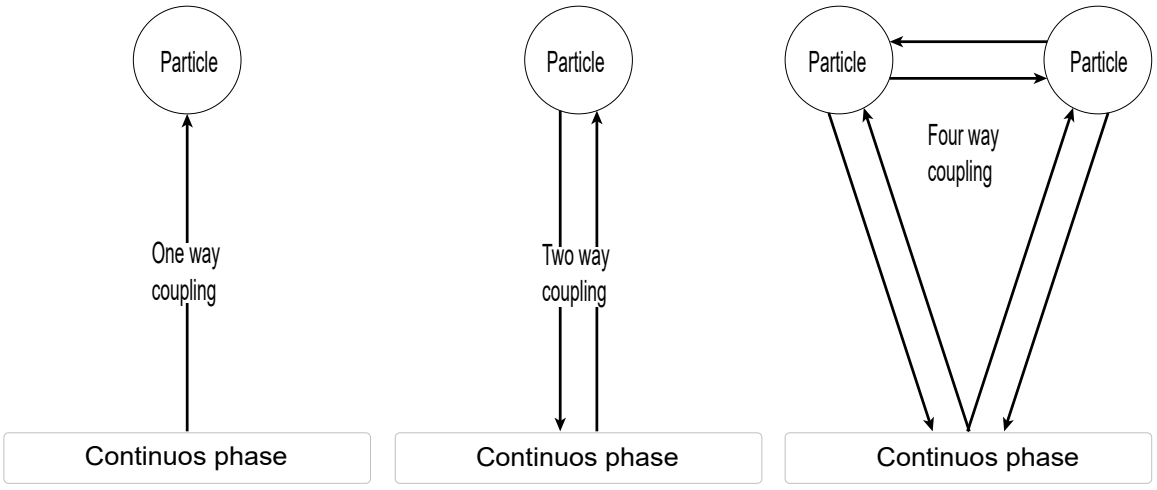

Figure 17 – Schematic representation of the coupling between dispersed and continuous phases.

3.3 Erosion prediction equation

It is well known that many correlation model to estimate the erosion ratio exist in literature, such as: the correlation proposed by Ahlert (1994), the correlation proposed by Neilson e Gilchrist (1968), the correlation proposed by Zhang et al. (2016) and the correlation proposed by Oka et al. (2005b). However, in the work carried by Pereira et al. (PEREIRA et al., 2014; DUARTE et al., 2015; SANTOS et al., 2016) it was found that the correlation proposed by Oka et al. (OKA; YOSHIDA, 2005) seems to be the best when utilized with the restitution model of Grant e Tabakoff (1975) once applied to predict erosion in ninety-degree-elbows. As a result, these models were used in this work. Both models (i.e., (OKA; YOSHIDA, 2005) and Grant e Tabakoff (1975)) will be described below and are also implemented in UNSCYFL3D, working alongside the fluid and particle models.

The erosion rate is defined as the mass of removed material per unit of area per unit of time. It is calculated on the walls by accumulating the damage each particle causes when colliding against the wall surface. It is given by:

$$E_f = \frac{1}{A_f} \sum_{\pi(f)} \dot{m}_\pi \, e_r \tag{3.39}$$

in which A_f is the face area, $\dot{m}_\pi$ is the particle mass flow rate represented by each computational particle that collides with the face and e_r is the erosion ratio, which consists in the ratio of mass of eroded material over mass of erodent material and must be computed by a correlation.

The erosion is formulated in terms of the penetration ratio, accordingly to the expression:

$$\text{Penetration Ratio} = \frac{E_f}{\dot{m}_p \, \rho} \tag{3.40}$$

where $\dot{m}_p$ is the inlet particle mass flow rate (kg/s) and ρ is the elbow material density (kg/m^3). The penetration ratio represents the thickness of material removed from the wall over the mass of particle injected into the elbow.

The predictive equation for erosion damage proposed by Oka et al. (OKA et al., 2005a) can be expressed as:

$$E(\alpha) = g(\alpha) \, E_{90} \tag{3.41}$$

$E(\alpha)$ and E_{90} denote a volume of eroded material per mass of particles (mm^{3}kg^{-1}). $g(\alpha)$ is the impact angle dependence expressed by two trigonometric functions and by the initial

eroded material Vickers hardness number (Hv) in unit of GPa, as in Eq. (3.42):

$$g(\alpha) = (\sin\alpha)^{n_1}(1 + \mathrm{Hv}\,(1 - \sin\alpha))^{n_2} \tag{3.42}$$

n_1 and n_2 are exponents determined by the eroded material hardness and other impact conditions such particle properties and shape. These exponents show the effects of repeated plastic deformation and cutting action, and for particles of SiO_2-1 are expressed by:

$$n_1 = 0.71\,(\mathrm{Hv})^{0.14} \tag{3.43}$$

$$n_2 = 2.4\,(\mathrm{Hv})^{-0.94} \tag{3.44}$$

The reference erosion ratio E_{90} (erosion damage at normal impact angle) is related to the impact velocity, particle diameter and eroded material hardness, and can be expressed as follows:

$$E_{90} = K\,(a\,\mathrm{Hv})^{k_1 b}\left(\frac{u_p}{u_{ref}}\right)^{k_2}\left(\frac{D_p}{D_{ref}}\right)^{k_3} \tag{3.45}$$

u and D are the impact velocity ($\mathrm{m\,s^{-1}}$) and particle diameter (μm), respectively, and u_{ref} and D_{ref} are the reference impact velocity and the particle diameter used in the experiments by Oka et al. (OKA et al., 2005a). k_3 is an exponent and is determined by the properties of the particle. The exponent k_2 can be determined by the eroded material Vickers hardness and the particle properties, as shown in Eq. (3.46)

$$k_2 = 2.3\,(\mathrm{Hv})^{0.038} \tag{3.46}$$

According to Oka et al. (OKA et al., 2005a) the term $K\,(a\,\mathrm{Hv})^{k_1 b}$ is highly dependent on the type of the particle and eroded material Vickers hardness, which are not correlated with the impact conditions and other factors. The present work used the experimental data from Oka et al. (OKA et al., 2005a) to derive a function and obtain the relationship between eroded material Vickers hardness and E_{90} at the reference impact velocity. The function obtained by the curve fitting shown in Fig. 11 of Oka and Yoshida (OKA; YOSHIDA, 2005) for the pair SiO2-aluminum is provided below:

$$K\,(a\,\mathrm{Hv})^{k_1 b} \approx 81.714\,(\mathrm{Hv})^{-0.79} \tag{3.47}$$

Is important to emphasize that this function holds for the pair sand-aluminum and may change for other materials. As a result, E_{90} can be expressed as follows:

$$E_{90} = 81.714\,(\mathrm{Hv})^{-0.79}\left(\frac{u_p}{u_{ref}}\right)^{k_2}\left(\frac{D_p}{D_{ref}}\right)^{k_3} \tag{3.48}$$

The purported strength of the Oka model is that the coefficients for a particular combination of eroded material and eroding material can be derived from more fundamental coefficients, which are specific to either the eroded material or the eroding material. Hence, the fundamental coefficients for sand can serve as a basis for both sand-steel erosion and sand-aluminum erosion, for instance. The fundamental coefficients for the eroding material, in turn, are shown to be derivable from measurable properties such as its Vickers hardness. Table 2 summarizes all the constants used in this work.

Table 2 – Constants used in the erosion ratio correlation (OKA et al., 2005a).

Eroded material type	Aluminum (6061-T6)
Eroded material Vickers hardness (H_v)	1.049 Gpa
Particle type	Angular SiO_2-1
Reference impact velocity (u_{ref})	104 m/s
Reference particle diameter (D_{ref})	326 μm
k_2	2.3042
k_3	0.19
n_1	0.7148
n_2	2.2945

3.3.1 Coefficients of restitution

The necessity of predict how particles behave after collisions with walls, led the development of the restitution models. In order to predict this behavior and be faithful to what occurs in reality, all of models were derived from experimental studies. The importance of these models is due to particles loss of energy and the rebound velocity been lower than the incident velocity. Summarizing, the reason to utilize a restitution models for the particle is basically because, the model provides an accurate prediction of the particle trajectories in the simulation.

Grant and Tabakoff (GRANT; TABAKOFF, 1975) proposed the restitution model after treating the post collisional particle movement dynamics in a statistical approach. Based on experimental data for aluminum and sand, they proposed equations (3.49) and (3.50) for the restitution coefficients:

$$e = 0.993 - 1.76\,\alpha + 1.56\,\alpha^2 - 0.49\,\alpha^3 \tag{3.49}$$

$$e_{par} = 0.998 - 1.55\,\alpha + 2.11\,\alpha^2 - 0.67\,\alpha^3 \tag{3.50}$$

It is noteworthy, that other restitution models exist, such as: the model proposed by Forder et al. (1998), and the model proposed by Sommerfeld e Huber (1999). Nonetheless, as already mentioned in section 3.3, the best model used for elbows is the one proposed by Grant and Tabakoff (GRANT; TABAKOFF, 1975) and for this reason utilized in this work.

3.3.2 Coefficients of friction

Friction is another important effect to be accounted for in particle-wall interactions. Depending on the static and dynamic coefficients, particles can lose energy and velocity, directly affecting the erosion. In UNSCYFL3D, $\mu = 0.25$ was adopted, as it was seen to provide the best fit to the experimental result (PEREIRA et al., 2014). Numerical experiments revealed that when friction is increased, the penetration ratio reduces slightly, and vice-versa. In any event, the curve is qualitatively similar.

Friction is not itself a fundamental force but arises from forces between the two contacting surfaces. The complexity of these interactions makes the calculation of friction from first principles impractical and necessitates the use of empirical methods for analysis and the development of theory.

An empirical model proposed by Sommerfeld e Huber (1999) described below:

$$\mu = \max(0.5 - 0.175\alpha, 0.15) \tag{3.51}$$

It is worth noticing that the static and dynamic coefficients of friction were assumed to be equal. No considerable difference was noticed by prescribing the dynamic coefficient lower than the static one.

4 Finite volume discretization

In this chapter a short summary about numerical methods will be presented, highlighting the finite volume method. In order to facilitate the comprehension , in section 4.1 a brief explanation of the solution method components are presented.

For the current research the UNSCYFL3D code is employed. UNSCYFL3D, amongst many other CFD packages, uses a Finite Volume Method (FVM) in order to resolve a flow field depending on its geometrical boundaries and their respective boundary conditions. For this approach the equations presented in the previous chapter have to be discretized in space.

Throughout the sections a brief overview of the discretization methods employed for the current research are presented. It is largely based on the information in the Fluent Guide (2005), supplemented with the work of Ferziger e Peric (2002) and Mathur e Murthy (1997). The methods outlined below may not be optimal, but they have proven to deliver sufficiently accurate results within a reasonable amount of time for the problem at hand.

Section 4.1 presents the components of the solution model, section 4.2 introduces the FVM. Then Sections 4.3 present the spatial discretization. The pressure-velocity coupling is presented in Section 4.4 and the solution procedure is elaborated in Section 4.5.

4.1 Components of a Solution Method

Prior to start the discussion about finite volume method some bases of a numerical approach have to be briefly discussed below.

The components of a solution method can be summarized as follows:

- **Mathematical model:** The starting point of any numerical method is the mathematical model. Trying to produce a general method of solution in a way that is applicable to all types of flows is impractical or even impossible, and as the most universally applicable tool, would probably not be able to provide optimum results for any particular flow;
- **Discretization Method:** The discretization method is a way of approaching the partial differential equations by algebraic equations into a set of discrete points in space and time. Several methods can be found in the literature, however, most approaches used are: Finite Difference, Finite Element and Finite Volume. Each of the aforementioned approaches tends to cause the same solution as the mesh

is refined. However some methods are more suitable for certain applications than others. In this work only the finite volume method is considered and discussed in section 4.2;

- **Numerical mesh:** The numerical mesh is in essence a discrete representation of the geometric domain where the problem should be solved. Having in mind that there are different types of mesh, such as: structured mesh, structured mesh by block and unstructured mesh. Nonetheless, in the present work the unstructured mesh is used. Because, this type of mesh better fits the finite element and finite volume approach;

- **Solution Method:** The discretization generates a large system of nonlinear algebraic equations. The choice of solver depends on the type of mesh used and the number of elements involved in each algebraic equation. In this work the solution methods used are just mentioned, in a way that the theory associate is not presented here.

4.2 Finite Volume Method

According to Maliska (2004), all methods that, to obtain the approximate equations satisfies the conservation property at a level of an elementary volume is a finite volume method. The author states that there are two ways to get the approximate equations in the finite volume method. First, is the realization of balances of the properties in question, in the elementary volumes, or finite volume. Second, is integrates about the elementary volume, in space and in time the equations in conservative form.

The finite volume method can be used with any type of mesh, in such way that it can be applicable with complex geometries. It is important to have in mind that the mesh only defines the boundaries of the volume control, and it is not necessarily related to a coordinate system.

The Finite Volume Method (FVM) is a method for representing and evaluating partial differential equations in the form of algebraic equations (LEVEQUE, 2002; TORO, 2009). Similar to the finite difference method or finite element method, values are calculated at discrete places on a meshed geometry. In the finite volume method, volume integrals in a partial differential equation that contain a divergence term are converted to surface integrals, using the divergence theorem. These terms are then evaluated as fluxes at the surfaces of each finite volume. Because the flux entering a given volume is identical to that leaving the adjacent volume, these methods are conservative. Another advantage of the finite volume method is that it is easily formulated to allow for unstructured meshes (VERSTEEG; MALALASEKERA, 2007).

4.3 Spatial discretization

The conservation equations for the continuity, velocity components and for the turbulence variables in unsteady state can be written generically as:

$$\underset{(1)}{\frac{\partial \rho\phi}{\partial t}} + \underset{(2)}{\frac{\partial}{\partial x_j}(\rho u_j \phi)} = \underset{(3)}{\frac{\partial}{\partial x_j}\left(\Gamma \frac{\partial \phi}{\partial x_j}\right)} + \underset{(4)}{S_\phi} \tag{4.1}$$

where, ρ is is the density of the fluid, ϕ is the variable to be transported and Γ is the diffusion coefficient.

Each term of Eq. 4.1 can be described as follows:

- **(1):** The first term on the left represents the variable accumulation over time in the considered volume control;
- **(2):** The second term on the left represents the convective flow (or advective), which considers the transport of the variable due to the existence of a velocity field;
- **(3):** First term on the right side represents the diffusive flux, which considers the transport of variables due to its gradients;
- **(4):** The last term of the right side represents the inclusion of a source term .

By integrating the general conservation Eq. 4.1 over the control volume V, we obtain:

$$\oint_V \frac{\partial \rho\phi}{\partial t} \cdot dV + \oint_A \rho\phi\vec{V} \cdot d\vec{A} = \oint_A \Gamma \text{grad}\phi \cdot d\vec{A} + \oint_V S_\phi dV \tag{4.2}$$

where V is the volume of the control volume.

Note that, for the terms involving surface integrals in Eq. 4.2, the Gauss Divergence Theorem was applied to convert the volume integrals into surface integrals (FERZIGER; PERIC, 2002):

$$\int_V \frac{\partial \phi}{\partial x_i} dV = \oint_A \phi\vec{l_i} \cdot d\vec{A} \tag{4.3}$$

For the element L shown in Fig. 18, the discretization of Eq. 4.3 yields:

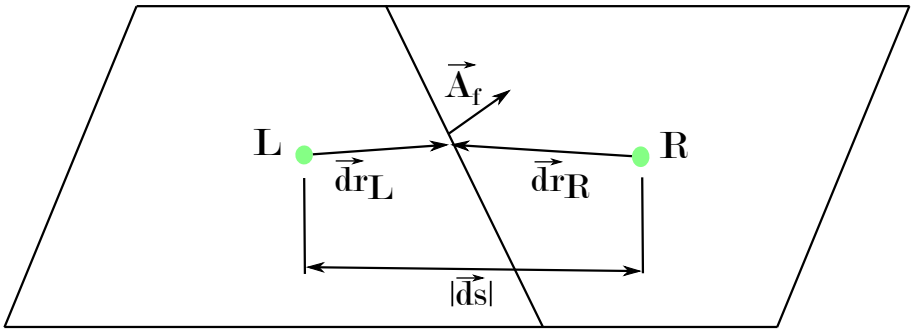

Figure 18 – Schematic representation of two elements separated by one face. Any face in the field will always have an element in the left "L" and an element in the right "R".

$$\left(\frac{\partial \rho\phi}{\partial t}\right)_L \Delta V_L + \sum_f J_f \phi_f = \sum_f D_f + (S_\phi \, \Delta V)_L \tag{4.4}$$

in which J_f is the mass flow rate, $(\rho_f \vec{V_f} \cdot \vec{A_f})$, across face f, Γ_f the diffusion coefficient at the that face and $D_f = \Gamma_f (\text{grad}\phi)_f \cdot \vec{A_f}$ is the diffusive flux across face f. The summations above apply to all the faces of element L. $\vec{A_f}$ is the normal area vector of face f, which is directed from the element L to the element R. Next, the discretization of each term of Eq. 4.4 is detailed.

The advection term

Regarding the advective term in Eq. 4.4, when the first-order upwind scheme is employed, ϕ_f is assigned the value of the element center at element L if J_f is positive. Otherwise, the value of element R is set to the face. Because first-order schemes are usually very diffusive for many applications of interest, a second-order upwind scheme was used in this work:

$$\phi_f = \phi_L + (\text{grad}\phi)_{rL} \cdot \vec{dr}_L \tag{4.5}$$

if $J_f > 0$. If $J_f < 0$ applies Eq. 4.5 considering the element to the right of the face f, R. In the above equation, the value of the variable in the face is obtained by extrapolation of the second order from the value in the *upwind*. The vector $\vec{dr}_L$ is directed from the geometric center of element L to the face f center. $(\text{grad}\phi)_{rL}$ is the reconstructed gradient at element L, which is again computed by means of the Gauss Divergence Theorem:

$$(\text{grad}\phi)_r = \frac{1}{\Delta V} \sum_f (\bar{\phi}_f \vec{A_f}) \tag{4.6}$$

where $\bar{\phi}_f$ is the average of ϕ the element centers sharing face f.

The first term on the right side of Eq. 4.6 is always implicitly treated, whereas the second term is treated as source term and therefore calculated explicitly.

The diffusion term

It can be proven that the diffusive flux for face f is given by (MATHUR; MURTHY, 1997):

$$D_f = \Gamma_f \frac{(\phi_R - \phi_L)}{|\vec{ds}|} \frac{\vec{A}_f \cdot \vec{A}_f}{\vec{A}_f \cdot \vec{e}_s} + \Gamma_f \left[\overline{\text{grad}\phi} \cdot \vec{A}_f - \overline{\text{grad}\phi} \cdot \vec{e}_s \frac{\vec{A}_f \cdot \vec{A}_f}{\vec{A}_f \cdot \vec{e}_s} \right] \tag{4.7}$$

In Eq. 4.7, $\vec{e}_s$ is the unit vector connecting the centers of elements R e L, $\vec{e}_s = \frac{\vec{ds}}{|\vec{dr}|}$. The first term at the RHS of Eq. 4.7 is treated implicitly, whereas the remaining terms, which represent the secondary diffusion, are calculated explicitly and therefore incorporated into the source-term S in Eq. 4.4. The secondary diffusion is null for hexahedra for instance, because vectors $\vec{A}_f$ and $\vec{e}_s$ are collinear. The gradient at face f, $\overline{\text{grad}\phi}$, is calculated as the average of the gradients at the adjacent elements. The treatment above is equivalent to the application of the second-order, centered differencing scheme in structured meshes and is advantageous in the sense that it does not depend on the element shape.

4.4 Pressure-velocity coupling

So far, it was proved that the momentum equations can be discretized via finite volume in unstructured meshes. Note that the set of Eqs. 3.4 and 3.5 forms a system of four equations (continuity, momentum for u, v and w) and four unknowns (u, v, w and p), thereby forming a given system. The velocity components must be determined by the respective conservation equations, but restricted with the imposed continuity. There is no explicit equation for the pressure, which requires the deduction of an equation for this variable so a segregated method of solution can be employed. The UNSCYFL3D uses the SIMPLE method (Semi-Implicit Pressure-Linked Equations, (FERZIGER; PERIC, 2002)) to generate this equation and ensure that the continuity equation is also satisfied.

In the SIMPLE method, the procedure solution of the equations for u, v, w and p is said segregated, which means that a system of linear equations for each of these variables are resolved independently by linear system solution methods, and sequentially. The process is repeated until all the standard equations residues is reduced until the specified tolerance. Several global iterations, with the solution of linear systems for u, v, w and p, may be necessary due to the nonlinear nature of the Navier-Stokes equations and the coupling between the variables. Since the variables converge at different speeds, it is necessary under-relaxed the system solutions. For the case of transient problems, global

iterations should be performed at each time step, and the process is repeated at each time step.

A more detailed discussion on pressure-velocity coupling can be found in (FERZIGER; PERIC, 2002).

4.5 Solution procedure

For the current study, only steady simulations are performed. For steady simulations the SIMPLE algorithm by Patankar (1980) is employed and briefly discussed below.

The SIMPLE algorithm can be summarized as follows:

1. Start-up the values of the velocities components and pressure in the elements and the mass flow rates across the faces of the calculation area, including the boundaries. These fields do not necessarily satisfy the conservation equations;
2. solves the linear system of equations for each component of the velocity vector, this corresponds to the predictor step. UNSCYFL3D uses biconjugated gradient method;
3. with the predicted velocity field, the mass flow rates is calculated on the faces of all the elements. It is then solved the linear system for the pressure correction. Normally, it is necessary to use an efficient solver based on multigrid methods, for example;
4. by knowing the pressure correction, the mass flow rates are corrected on the faces, the pressure in each element, and the velocity components in each element;
5. evaluate the residues and the momentum equations after the corrector step and if they are satisfied according to the tolerance specified by the user, declares the convergence of the set of equations. Due to the couplings between the variables, a global iteration of SIMPLE is usually not sufficient to ensure that all equations are satisfied simultaneously. In this case, the solver returns to the step 2 and the process continues until the convergence of all the equations.

It is important to remember that for transient problems, the above procedure is performed for each time step. The flowchart solution of SIMPLE method is shown in Fig. 19:

4.6 Solver UNSCYFL3D

The UNSCYFL3D is an ”in-house” code developed in the Laboratory of Fluid Mechanics (MFlab) from the Federal University of Uberlândia in partnership with PETROBRAS. The code is capable of simulating laminar and turbulent flows with particles. In

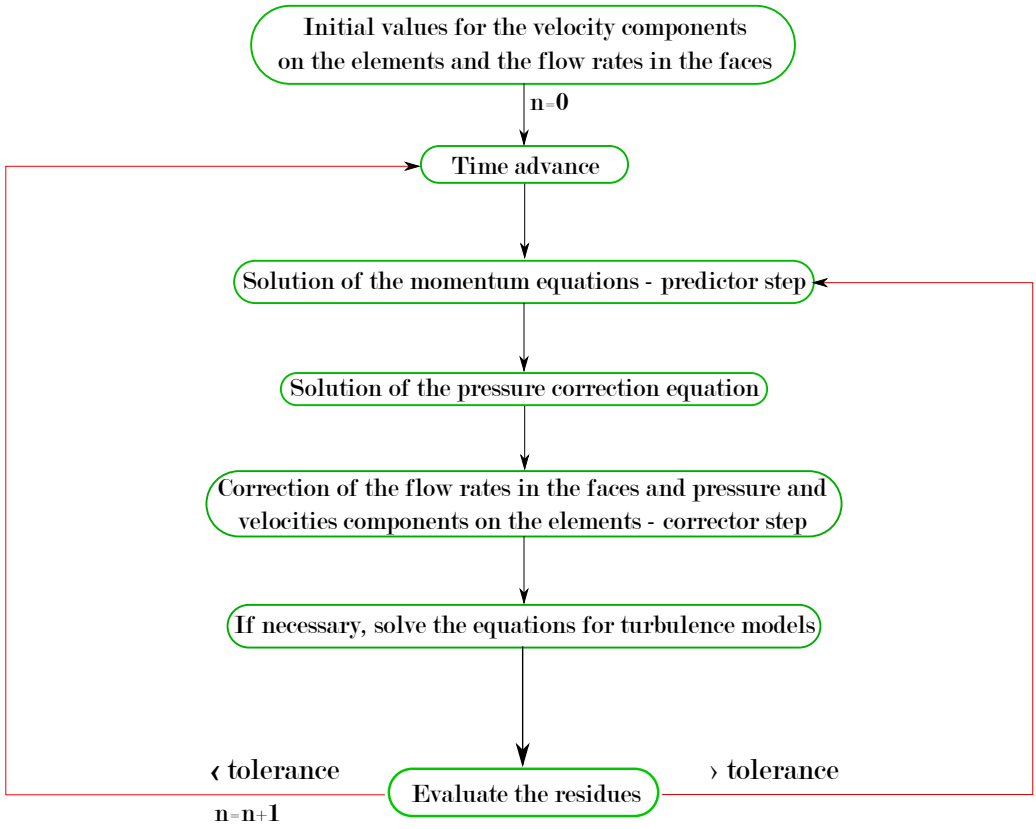

Figure 19 – Flowchart solution of SIMPLE method implemented in UNSCYFL3D.

UNSCYFL3D, the Navier-Stokes equations in the incompressible formulation are solved numerically using the finite volume method of Ferziger e Peric (2002) in unstructured meshes, which can be composed of hexahedra, tetrahedra, prisms, pyramids and wedges. For the disperse phase modeling, a Lagrangian formulation is employed, where the particles are individually tracked in the flow. For the pressure-velocity coupling, the SIMPLE algorithm is used. Flow in both permanent and transient regimes can be simulated, and 6 boundary conditions can be prescribed: imposed velocity, symmetry, outflow, non-slip, imposed pressure and frequency.

The diffusive terms are discretized by 2^{nd} order centered differences, for the advective terms, the *upwind* scheme and the 1^{st} order centered scheme or *upwind* scheme 2^{nd} order can be combined. The large scale turbulence models are: Smagorinsky, dynamic and Yakhot. The SST and DES-SST models are also available. For the integration of the motion equations of the particles, it uses the analytical model. Particles can be injected into faces in which the boundary condition of imposed velocity is applied. The following boundary conditions for the particles are possible: reflection, escape and frequency.

For the erosion-related problems the correlations from: Ahlert (1994), Neilson e Gilchrist (1968), Zhang et al. (2007) and Oka e Yoshida (2005) can be employed. The coefficients of restitution can be selected from: Forder et al. (1998), Sommerfeld e Huber (1999) and Grant e Tabakoff (1975) models.

For time advance of the flow equations, the implicit Euler scheme 1^{st} and three levels in time 2^{nd} can be used. The mesh converter was developed in C language, and the solver in FORTRAN 90 language. Both flow and particles can be post processed using Paraview and VisIt tools.

5 Particle phase algorithm

According to Elghobashi (1993), when starting a single-phase flow into a flow with a high particle loading, four different regimes will be achieved, and these arrangements relate to the manner in which the flow "feels" the presence of the dispersed phase (type of coupling) and the manner in which the dispersed phase interferes with the turbulence of the continuous phase (attenuating or increasing the turbulence levels).

To illustrate this relationship, Elghobashi (1993) created a map, Fig. 20, based on the volume fraction of the particulate phase ϕ_p; number of particles N_p; the volume occupied by the particles V_p; the distance between the centers of two neighboring particles S; the particle diameter d; the particle response time T_p, the Kolmogorov timescale T_k and the turnover time of large scale T_e.

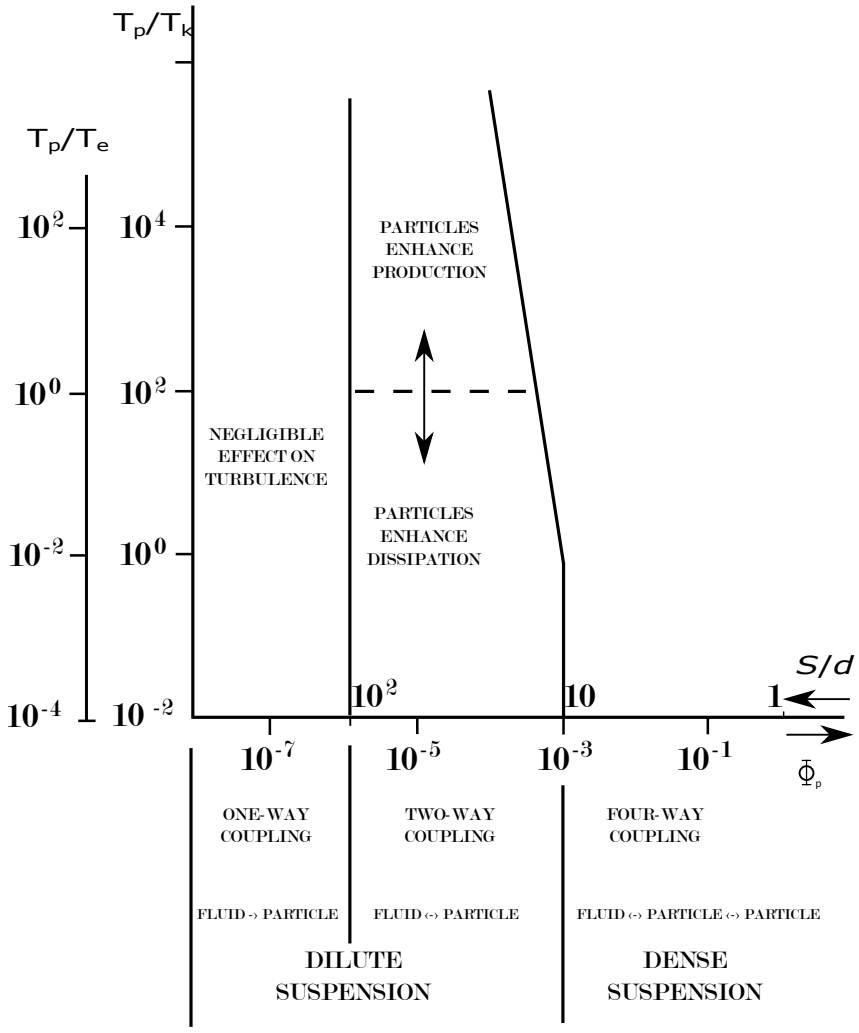

Figure 20 – Diagram showing the flow regimes. Adapted from Elghobashi (1993).

According to the diagram proposed by Elghobashi (1993) the flows with a volume

fraction higher than 10^{-6} should be treated using two-way coupling and flows with a volume fraction superior to 10^{-3} using four-way coupling. In the other hand, for the volume fraction between 10^{-6} and 10^{-3}, it is possible to notice at Fig. 20, that the dispersed phase can act to mitigate the turbulence of the continuous phase, or increase the turbulence. Depending of the relationship between the relaxation time of the particle and the turnover time of the large scale of the flow.

For both Lagrangian and Eulerian approaches, it should be noted that the two-way coupling requires the description of the coupling between the phases and the particle. This interaction occurs through the tension between the phases at the particle surface. In particular, the coupling strength between the phases is the force acting on a single particle due to pressure and viscous tension caused by the disturbed fluid around. This force is equal in magnitude and opposite in direction to hydrodynamic force of the particle acting on the continuous phase. The coupling strength between the phases is the hydrodynamic forces on the surface less the contributions of the tensions of the undisturbed fluid (*e.g.*, less forces due to the pressure gradients which occur regardless of the presence of the particle).

The next section will briefly explain the coupling procedure used in UNSCYFL3D.

5.1 Coupling procedure

The coupled solution of the continuous and particle phases is summarized as follows (LAÍN; SOMMERFELD, 2012): first the steady-state solution for the fluid phase without particles is computed. Subsequently, particles are injected and tracked throughout the domain. For each control volume, the average and RMS linear and angular velocities, the particle concentration and the source-terms for the fluid momentum equation are stored.

After all the particles have left the domain, the fluid flow is solved again, now considering the source-terms sampled during the previous particle calculation. This process is repeated, taking the particle-to-particle collision into account, until a converged solution for both phases is reached. It is important to bear in mind that the particle statistics must be corrected during each particle calculation. Another important detail is that the particle source term must be under-relaxed, for achieving convergence. The present work used 0.1 as under-relaxation factor for all the cases, and the quality of convergence was measured based on the standard deviation of average velocities, which should be close to 0.001. Normally, 100 coupling iterations are sufficient for convergence of both phases. A detailed information about this method is given by (LAÍN; SOMMERFELD, 2013).

The scheme of this procedure is presented in Fig. 21.

To solve the differential equations, it is important to know the location of each

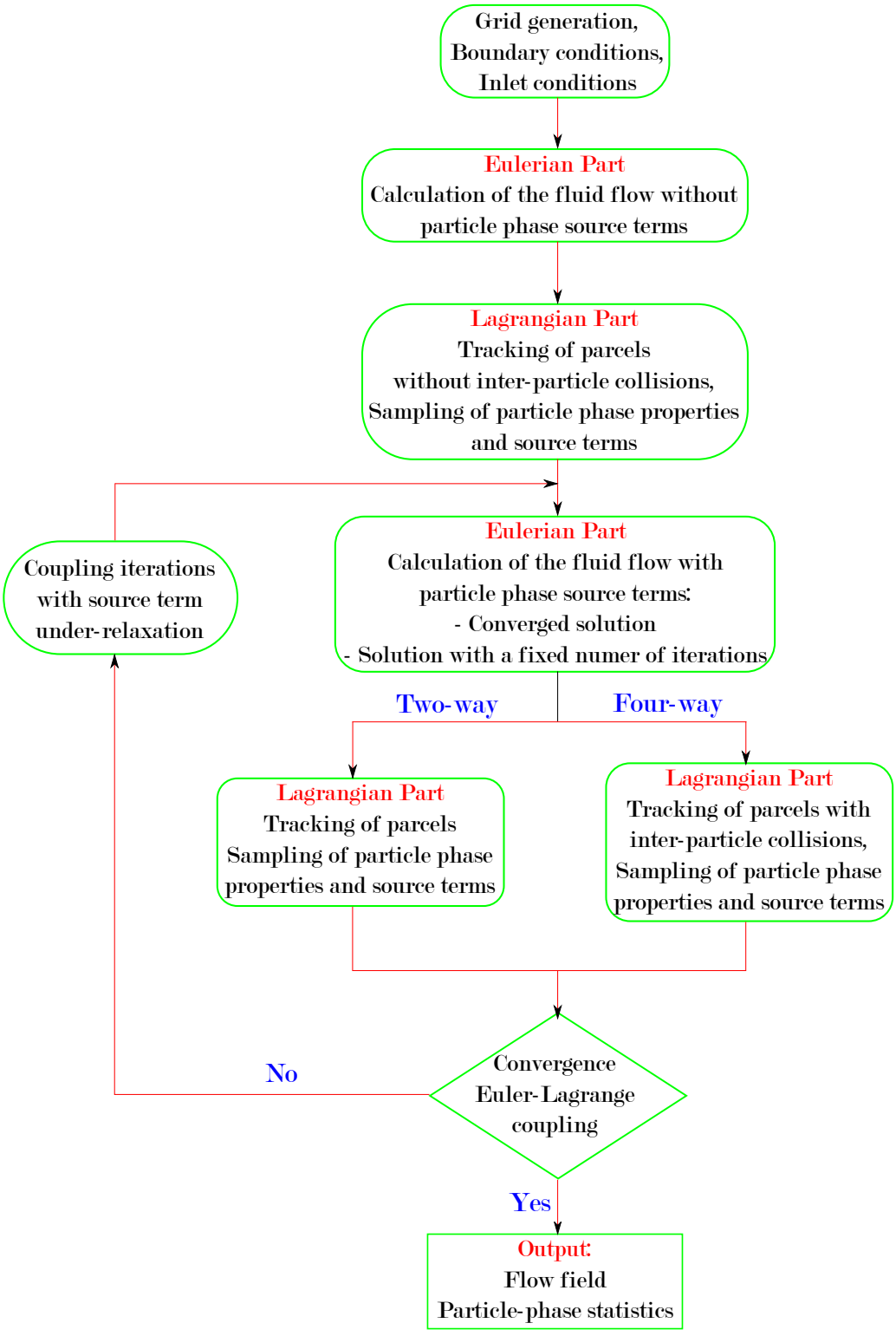

Figure 21 – Flow chart of fully coupled Euler-Lagrange calculations (LAÍN; SOMMERFELD, 2013).

particle within the Eulerian mesh. This occurs because to calculate the variation of velocity and position of the particles is necessary to interpolate the fluid properties to the position of its center of mass. Usually, the computational determination of the cell in which a particle is can be done quickly and efficiently by using a particle locator and a mesh

mapping in cartesian uniform meshes. However, this approach can not be directly used in unstructured grids (PENG et al., 2009), making the particle tracking problem an important element. Next section is dedicated to briefly explain the particle-location algorithm used in the present report.

5.2 Particle-tracking algorithm

The UNSCYFL3D code uses the algorithm proposed by Haselbacher et al. (2007). This choice was due to some specific features of this algorithm:

- this algorithm is robust enough to allow a particle to crosses more than one computational cell in a single step and time, in other words, the algorithm enables the particle to go through long distances, which is a limiting factor for a number of algorithms;
- the algorithm is based on distances intersection rather than time intersection, which is much more natural, once the particle tracking problem should be primarily a spatial problem, not temporal;
- the algorithm can be applied to Eulerian meshes consisting of polyhedral elements;
- according to the author, this algorithm is faster and more efficient than other published algorithms.

The complete procedure of particle-location as well as the algorithms used are not presented here because it differ completely from the main theme of the dissertation. A detailed information about the algorithm and its implementation can be found in the publication of Haselbacher et al. (2007).

All the information presented until now allow the reader to familiarize themselves with the problem analyzed and the procedure used for its solution. With this in mind, will be presented in the following chapters the numerical setup and procedure (Chap. 6) and the results (Chap. 7) obtained, respectively.

6 Numerical setup and procedure

Experimental studies of erosion on different elbow configurations have been carried out (SELMER-OLSEN, 1987; EYLER, 1987; CHEN et al., 2006). Mazumder et al. (MAZUMDER et al., 2008) provide a good database, limited to very low mass loadings. According to the experimental setup described by Mazumder et al. (MAZUMDER et al., 2008), in which aluminum elbow specimens were used, sand particles were injected in the horizontal pipe at about 48 in (1.22 m) below the test piece. Fig. 22 shows the schematics of the standard elbow. The respective dimensions are presented in Table. 3. The erosion data was measured along the outer bend surface, represented by the blue color in the scheme of Fig. 22. Hence, a comparison of the calculations with the measurements is made at this location.

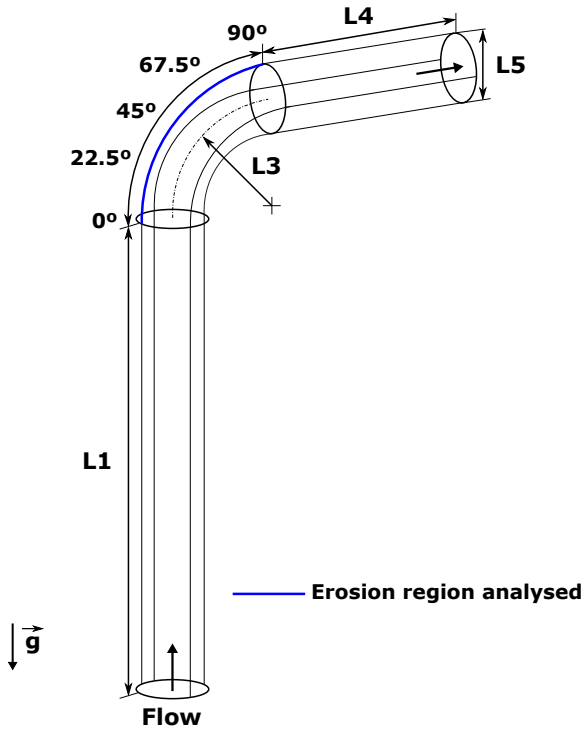

Figure 22 – Schematics of the simulated standard elbow.

For all the simulations, the fluid phase was treated as air with constant density and viscosity. At the pipe inlet, the fluid is injected with a mean conveying velocity of 34.1 m/s and a turbulence intensity of 0.1%. At the pipe walls a no-slip condition is applied while at the pipe exit the static pressure is prescribed. Table. 4 summarizes the properties of the fluid, particle and pipe used in all computations. They yield a Reynolds number of 5.93×10^4. The particle Stokes number based on the mean particle diameter is 3.66.

Table 3 – Dimension of the elbow and twisted tape insert, as shown in Fig. 22 and Fig. 23.

Pipe diameter ($D = L5$)	0.0254 m
Elbow curvature ($1.5D$)	0.0381 m
Inlet till the beginning of the bend ($L1$)	1.22 m
End of the bend till the outlet ($L4$)	0.1016 m
Tape thickness ($0.1D$)	0.00254 m
Tape length ($3D = L6$)	0.0762 m
Tape twist	180 degrees
Twisted tape insert position ($L2$)	$0D, 1D, 2D, 3D$

Table 4 – Simulation conditions for erosion prediction.

Fluid	Air
Fluid density	$1.225\,\mathrm{kg/m^3}$
Fluid viscosity	1.79×10^{-5} Pa.s
Bulk fluid velocity at inlet	34.1 m/s
Material of specimen	Aluminum (6061-T6)
Material density	$2,700\,\mathrm{kg/m^3}$
Particle type	Angular SiO_2-1
Particle density	$2,600\,\mathrm{kg/m^3}$
Average particle size	$182\,\mu$m
Mass loading	$0.013\,\mathrm{kg}_p/\mathrm{kg}_g$

Regarding the two-phase flow simulations, the mass loading ratio investigated in the experiments was $\phi = 0.013$. For all cases investigated, the mean particle diameter was 182 μm and the pipe material was Aluminum (6061-T6). The wall pipes were assumed to be perfectly smooth. However, as investigated by Solnordal et al. (SOLNORDAL et al., 2015), the wall roughness apparently has a very important role in the erosion patterns. Therefore, the numerical penetration patterns may depart from experiments, since actual pipes are always rough. This has been investigated by the authors in (DUARTE et al., 2016a). Regarding the particle tracking, 300 particles are injected at each fluid time step, which was 10^{-4} s. The particle time step is 10^{-5} s. By the end of the simulation, nearly 6,000,000 particles paths have been tracked, which provide converged statistics and erosion profiles. The simulations were run for 2 physical seconds. It is important to bear in mind that each computational particle represents a number of real particles with the same properties (i.e. velocity and size). Once the validation of the standard elbow was done, a twisted tape was added to the original geometry at four different positions upstream of the elbow, namely at 0, 1, 2 and 3 diameters away from the bend inlet. Figure 23 represents the schematics for the twitsed tape placed one diameter upstream of the bend. The main geometric features (i.e. pipe diameter, curvature radius, domain size) and remaining simulation setup were preserved. The flat spiral tested was twisted through 180 degrees with a thickness of 0. 1D and a total length of 3D, as shown in Fig. 24, for the purpose of generating swirling flow upstream of the bend.

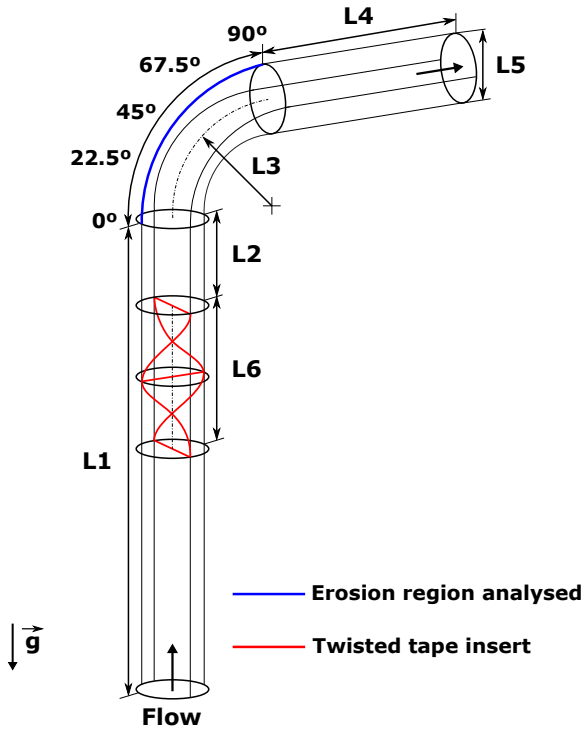

Figure 23 – Schematics of the elbow with a twisted-tape.

Moreover, to quantitatively compare the "twisted-elbow" results (e.g., penetration ratio, the particles impact angle, impact frequency and impact velocity) with the standard elbow results, the penetration ratio profiles were extracted from the symmetry plane along the bend outer wall.

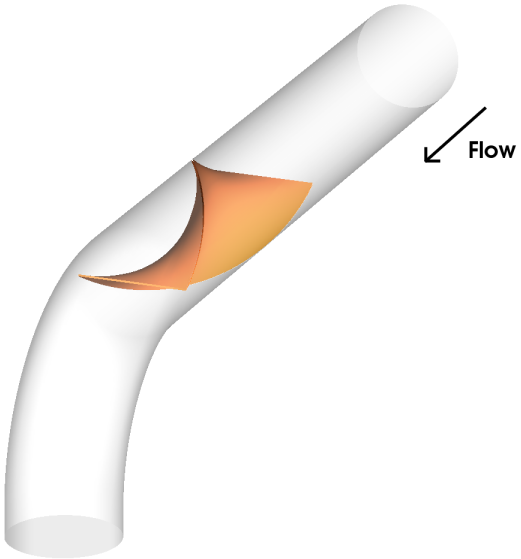

Figure 24 – Twisted tape geometrically.

When constructing the grids, special care must be taken to guarantee that the maximum element orthogonality is achieved, as low quality elements are known to deteriorate the accuracy of the calculations. Fundamental to the precise calculation near wall behavior

the refinement in the boundary layer zone (Fig. 25e and Fig. 25f) is needed. The refinement close to the walls was the same for all cases so that the dimensionless wall distance (y+) was kept below 1 for first cell adjacent to the wall. Only hexahedra were used in the mesh construction, which generate less numerical diffusion than elements such as tetrahedra and pyramids. Hexahedra also allow the generation of higher quality meshes, with fewer distorted elements than one would obtain with tetrahedra, for example. An effort was made to generate less distorted elements inside the twisted elbow. As a final remark, the grids presented in Fig. 25 are multiblock structured grids with O-type structures composed of 8 and 5 blocks for the twisted-tape-equipped elbow and the standard elbow, respectively, resulting in approximately 650,000 hexahedral control volumes.

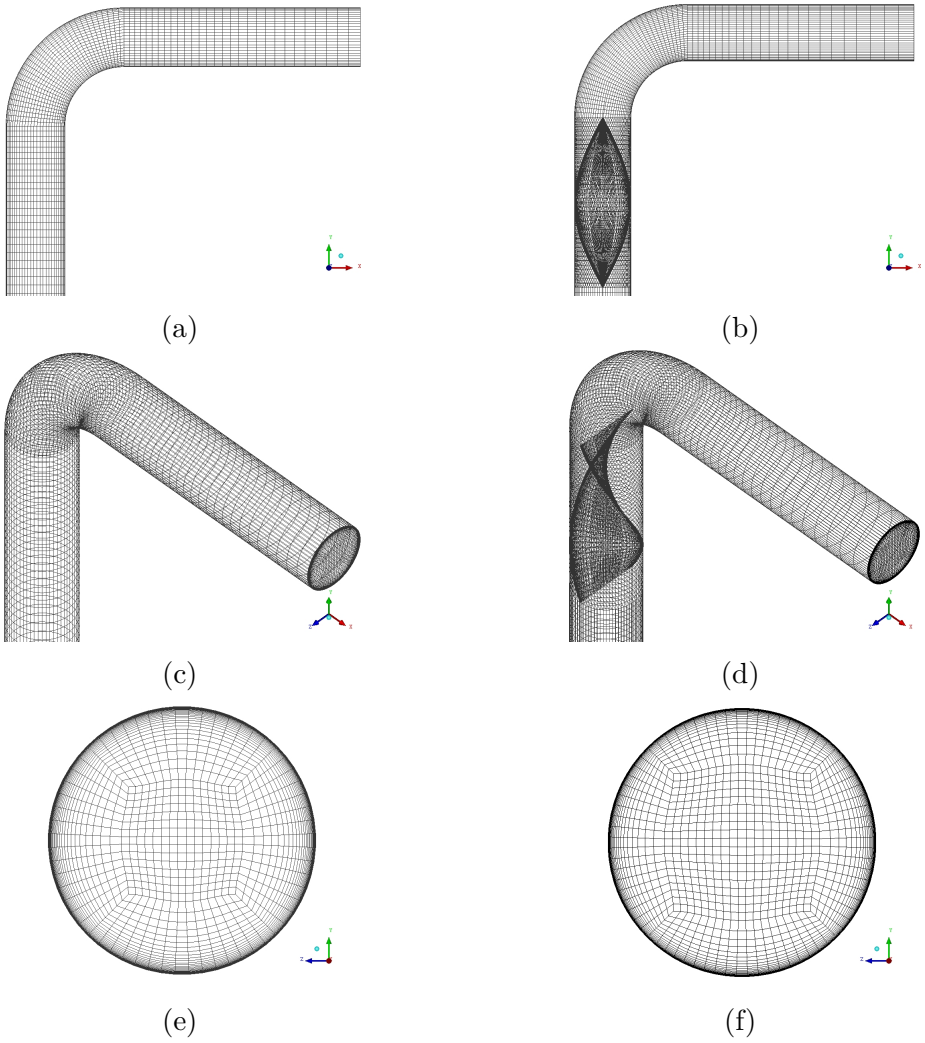

Figure 25 – Mesh used in the simulations: (a), (c) and (e) Standard elbow mesh; (b), (d) and (f) Twisted tape elbow mesh with the insert at 0D.

7 Results

This section is divided into three main topics. First, the standard elbow is used to validate the computational models employed. The most important parameters related to the particle mechanisms and erosion are also presented for future reference and comparison with the modified geometries. Subsequently, a twisted tape is added to the original pipeline at different locations and the investigation of the best position is carried out considering one-way coupling. Then, an analysis of the two-phase effects is done for the best position and compared to the standard elbow.

7.1 Standard elbow results

Figure 26 shows the streamlines of the velocity field inside the standard elbow. This figure illustrate the fluid behavior inside the bend and give an initial idea about the studied problem.

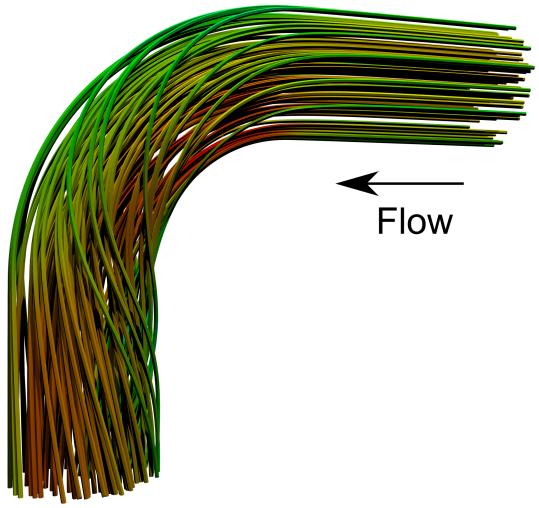

Figure 26 – Streamlines of the velocity field inside the standard elbow.

7.1.1 Validation - one, two and four-way coupling

For these tests, the friction coefficient was set as 0.25 and the restitution model of Grant and Tabakoff (GRANT; TABAKOFF, 1975) was used. Since this restitution model was formerly obtained from experiments with sand particles hitting against an aluminum surface, it is the most appropriate correlation for the current investigations.

In order to validate the numerical models, the experiments by Mazumder et al. (MAZUMDER et al., 2008) were used. Figure 27 displays the contours of the penetration ratio for the different phase interaction regimes, as seen from the opposite side of the domain inlet. Quantitatively speaking, the erosion contours are quite similar for all cases, as well as the magnitude of the penetration ratio. This was somewhat expected, since the mass loading (0.013) is not high enough to cause any significant coupling between the gas and the particles. Nevertheless, it is possible to notice a slight decrease in the penetration magnitude when the phase interactions are accounted for.

On the part to compare the erosion profile with the experimental data, the origin (0°) of the local coordinate system is set at the elbow inlet, whereas 90° corresponds to the elbow flow outlet (Fig. 22). Figure 28 shows the penetration ratio profile for one, two and four-way couplings, as well as the experimental data by Mazumder et al. (MAZUMDER et al., 2008), which also display the uncertainty for each experimental point. Visibly, the results agree with the experiment.

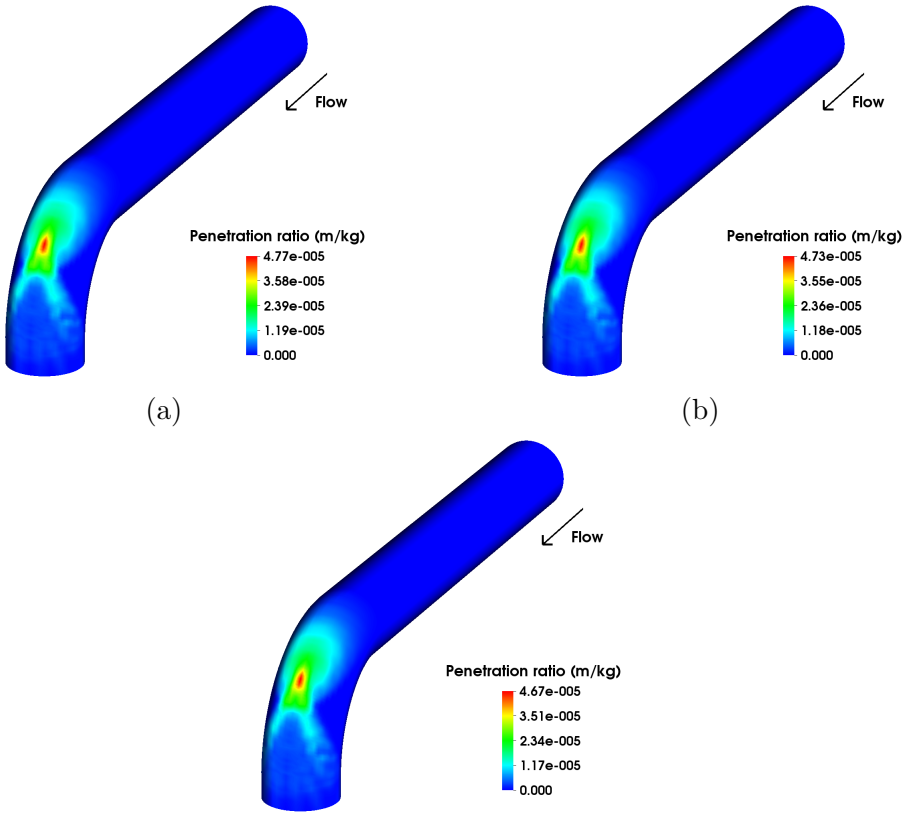

Figure 27 – Penetration ratio for the standard elbow: (a) One-way coupling; (b) Two-way coupling and (c) Four-way coupling.

Note that the one-way coupling model would have been sufficient to provide a first impression of the problem with good results for a simple geometry operating with low mass loading. This is advantageous from the computational point of view, since one-way

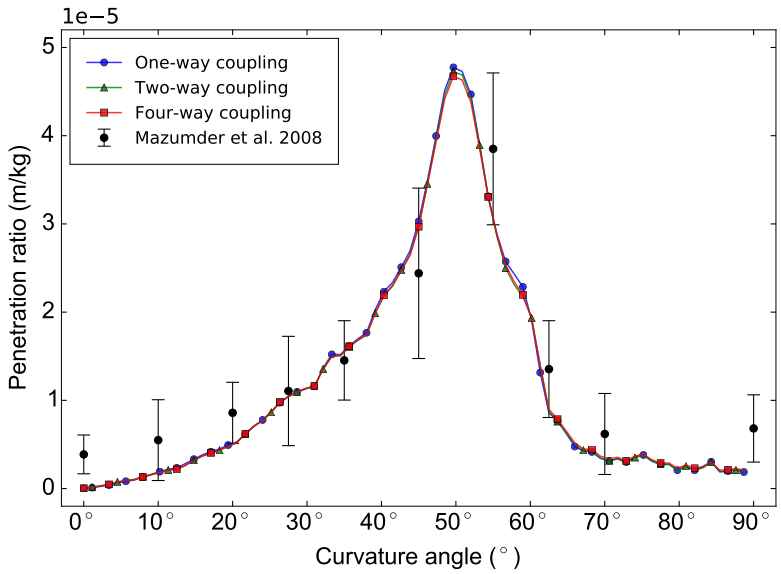

Figure 28 – Penetration ratio versus curvature angle for standard elbow.

coupling calculations can be up to 100 times faster when compared with two and four-way coupling calculations. However, as shown by Duarte et al. (DUARTE et al., 2015), as the mass loading increases, interphase coupling becomes increasingly important, dramatically modifying the erosion contours and magnitude for the standard elbow.

7.1.2 Particle erosion mechanisms

For a given pair of materials, the penetration magnitude is a function of three variables: particle impact velocity, particle impact angle and particle-wall impact frequency, as most correlations reveal. Thus, with those three parameters at hand, the erosion behavior resulting from geometry changes can be explained based on the particle mechanics. The contours for such variables are shown in the next sub-sections.

7.1.2.1 Impact frequency

The frequency at which particles collide with the elbow wall is one of the most important factors to explain the penetration ratio, because the more often particles strike the same spot, the higher will be the penetration ratio and mass loss at that location.

As a reference for the effects of the twisted tape, the contours for the particle-to-wall impact frequency are shown in Fig. 29 for each phase interaction regime.

Although very similar, a slight reduction can be noticed in the four-way case as compared to the one-way results. This is shown in Fig. 29, which shows the contours of the impact frequency along the elbow. Such a reduction, although not quantitavely important, as can be seen in the profiles presented in Fig. 30, is due to the inter-particle collisions

and the interaction between gas and the particles, which causes the particles to spread in a more realistic way within the flow.

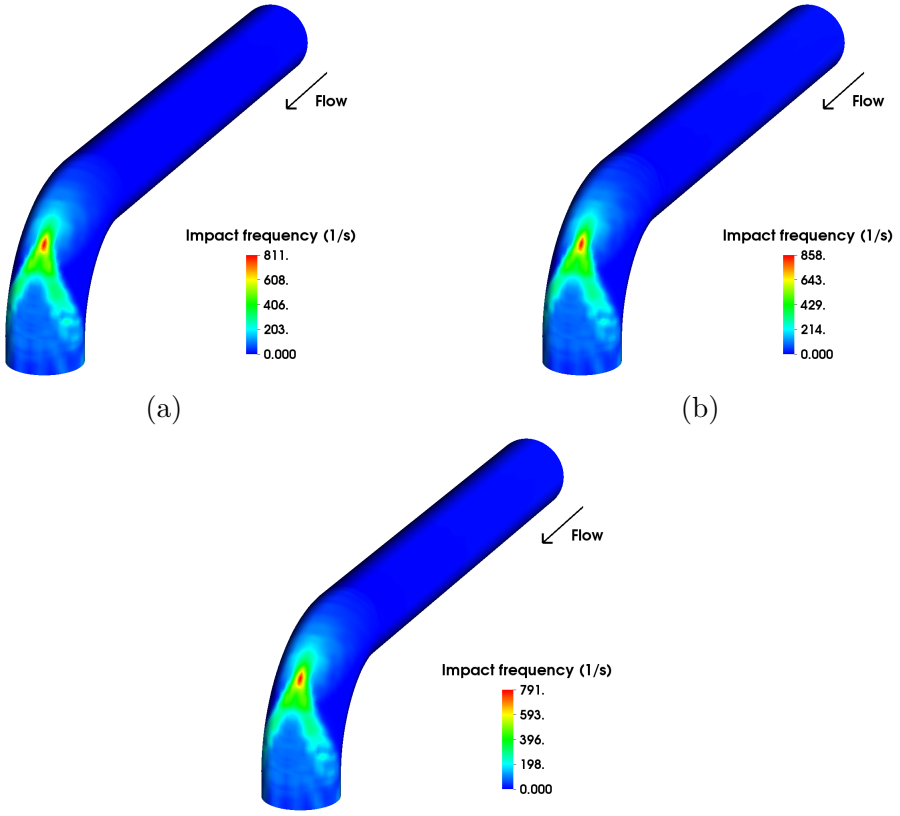

Figure 29 – Impact frequency for the standard elbow: (a) One-way coupling; (b) Two-way coupling and (c) Four-way coupling.

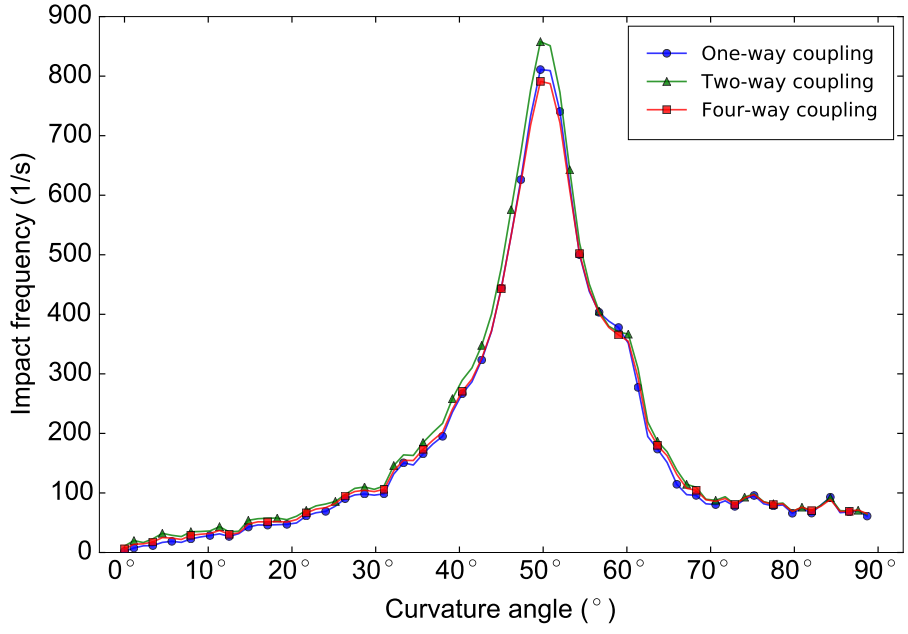

Figure 30 – Impact frequency versus curvature angle for standard elbow.

7.1.2.2 Impact velocity

Since the erosion ratio is proportional to a power of the impact velocity, it might be expected that it is the most influential parameter on the penetration ratio. In Fig. 31 the contours for the impact velocity are presented. It is possible to notice that the maximum velocity is the same for one, two and four-way calculations, although the erosion patterns are different, demonstrating the influence of the particle-particle and fluid-particle interactions.

When inter-particle collisions are accounted for, the contours of the impact velocity are more homogeneously distributed along the bend. In the case of one and two-way couplings (Fig. 31a and Fig. 31b) there is a region opposing the bend where there is no particle. In contrast, if interparticle collisions are included (Fig. 31c), the same region is hit by the particles, because of the dispersion owing to the impacts between particles and pipe walls as well as among particles. Regarding Fig. 32, the impact velocity increases between curvature angles of 0° and 35°. This is expected, since this region experiences the first impact of the particles with maximum velocity. Downstream of this region, the impact velocity decays up to 90°, as the particles now move adjacently to the bend wall.

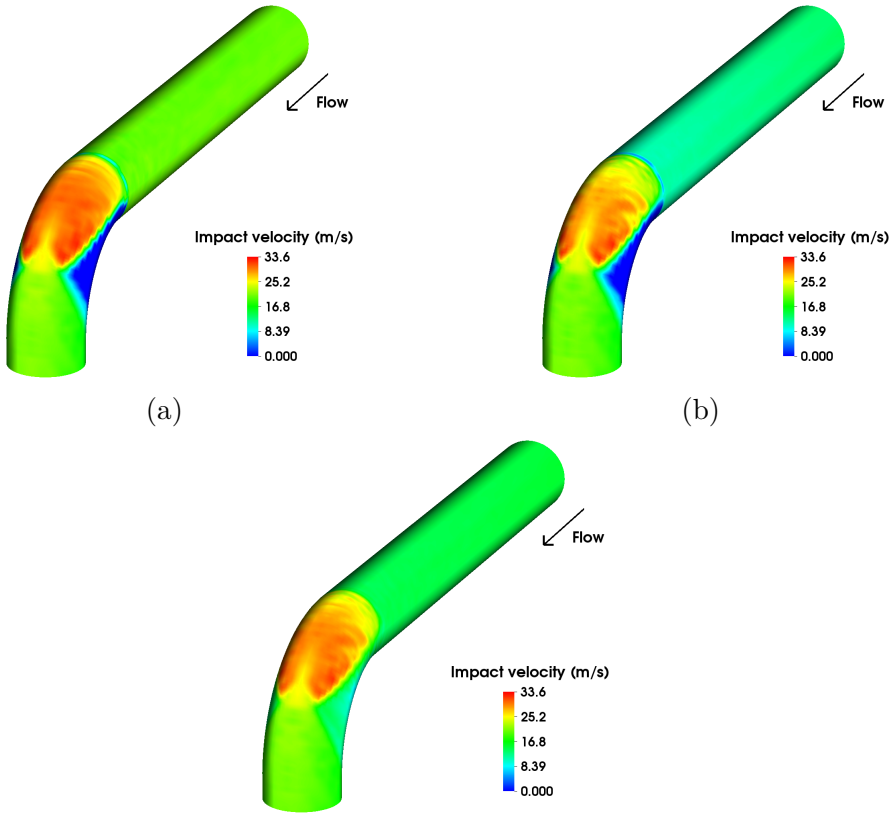

Figure 31 – Impact velocity for the standard elbow: (a) One-way coupling; (b) Two-way coupling and (c) Four-way coupling.

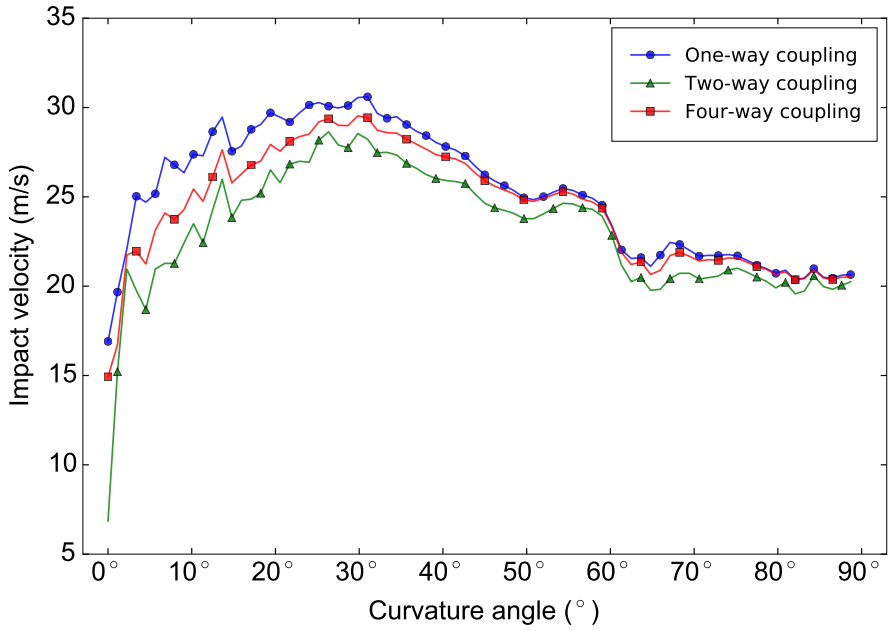

Figure 32 – Impact velocity versus curvature angle for standard elbow.

7.1.2.3 Impact angle

The fragility and ductility of the material play an important role regarding the impact angle. As mentioned in the previous sections, we simulate an aluminum elbow, which is classified as a ductile material. In the research carried out by Finnie (FINNIE, 1960) the maximum erosion ratio occurs at an impact angle of 16° for aluminum. In Fig. 33 the contours of this parameter are presented. It is shown that when the interactions between the gas and the particles are taken into account the maximum impact angle is decreased. This can be attributed to the momentum exchange with the flow as well as to the more homogeneous particle distribution. Regarding the profile shown in Fig. 34 it can be noticed that there is a valley between 45° and 55°, i.e., in the midst of the two peaks. As presented in the previous analysis in this section, the maximum values for the penetration ratio and impact frequency lie in the very same region. Thus it can be said that the maximum erosion ratio occurs at an impact angle between 13° and 16°.

Interestingly, as shown in the above figures, the maximum erosion region may not coincide with the impact velocity peak, as one might naively expect. Instead, it is necessary to analyze the three parameters, namely impact velocity, impact angle and impact frequency to explain the erosion patterns and mechanism. As a summary of this section, the computational models have been validated based on experiments for a standard elbow considering interphase coupling effects. This adds confidence to the models used. Apparently, the main parameter affecting the penetration ratio is the wall collision frequency, whose peak coincides with the maximum penetration ratio. A slight reduction in the peak penetration ratio was found to result from the phase momentum interchange,

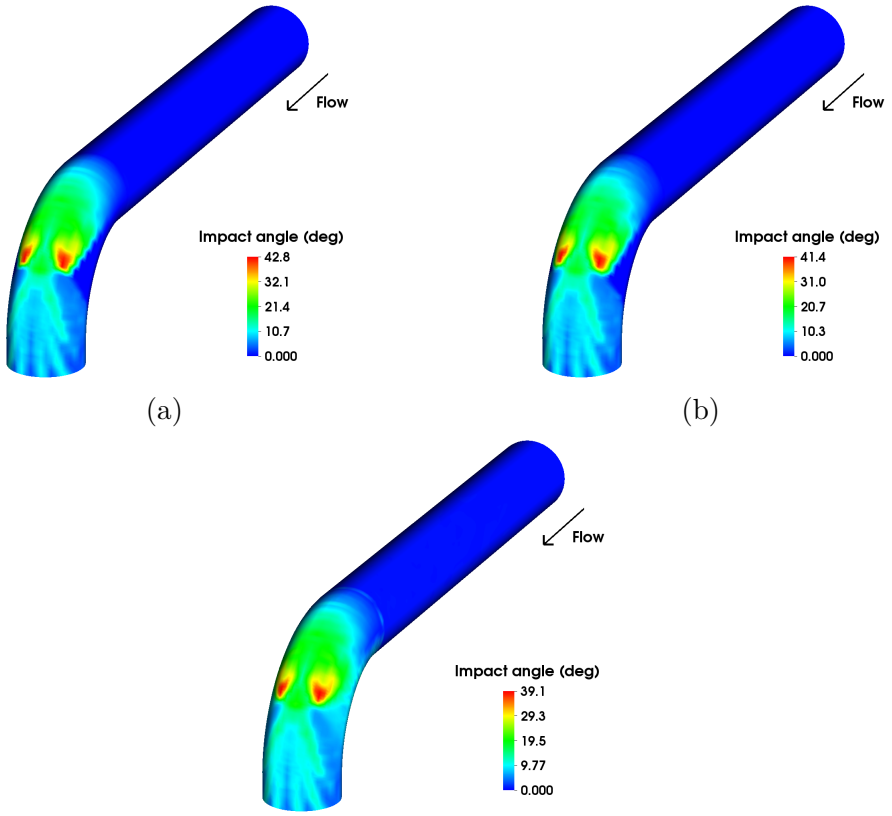

Figure 33 – Impact angle for the standard elbow: (a) One-way coupling; (b) Two-way coupling and (c) Four-way coupling.

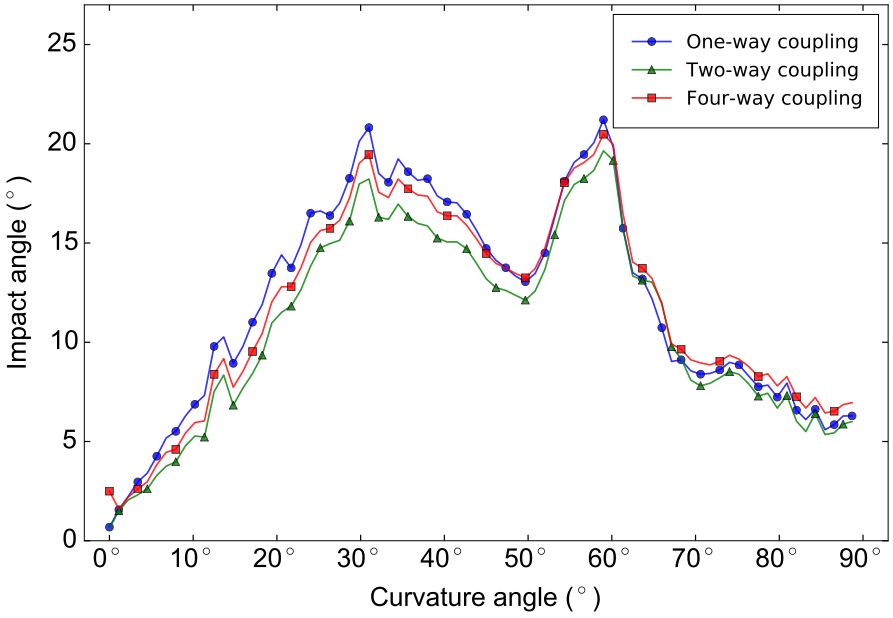

Figure 34 – Impact angle versus curvature angle for standard elbow.

even at the low mass loading simulated. Based on the validated models, the same elbow equipped with a twisted tape can now be investigated.

7.2 Results for the elbow with a twisted tape insert

7.2.1 General flow impression

Before seeking for the best position of the twisted tape in the pipe line with the intention of reducing elbow erosion, we present the contours of the gas velocity magnitude at different cut planes along the pipeline in Fig. 35.

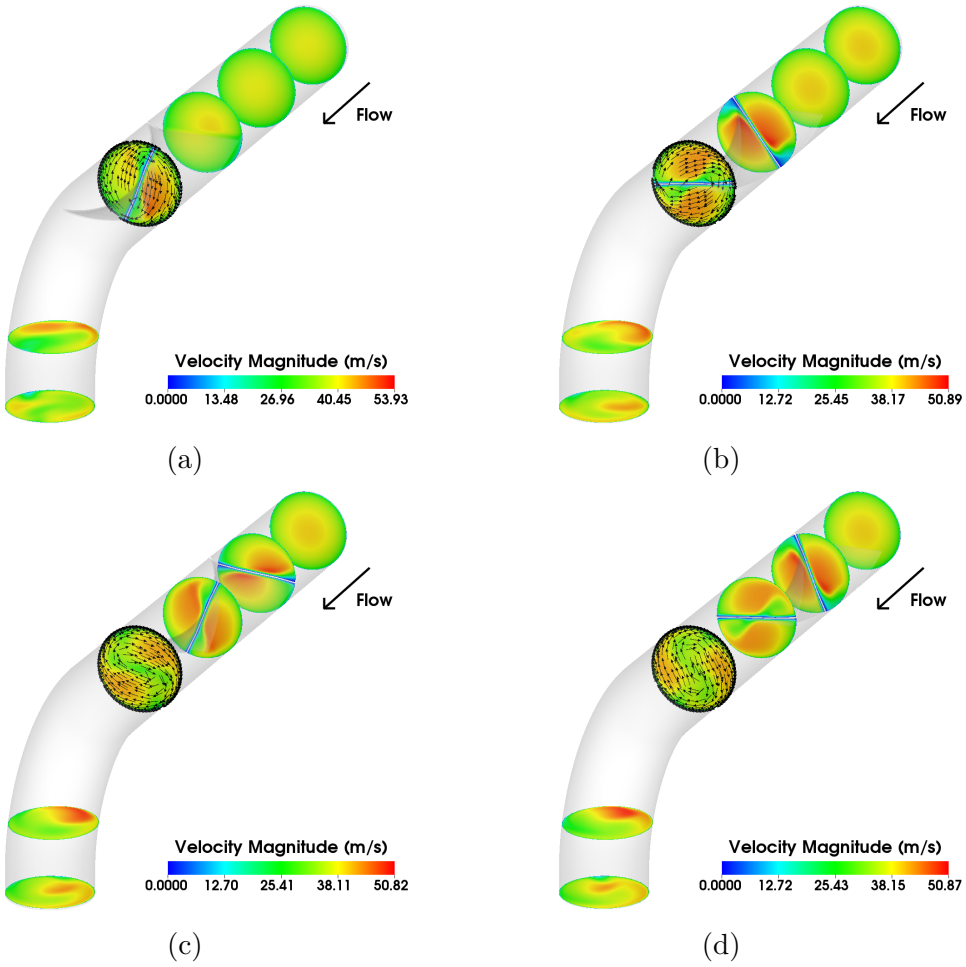

Figure 35 – Velocity magnitude along the curve with different cut planes for all twisted tape insert in positions (a) 0D; (b) 1D; (c) 2D and (d) 3D.

It is possible to observe that the maximum velocity is nearly the same for all positions, although the velocity profiles change considerably depending on where the insert is placed. The incoming gas flows from the domain inlet until it reaches the insert, where it is split into two parts across the pipe section, therefore creating a swirling motion. The swirl imparted by the twisted tape lasts for some pipe length, during which the rotating motion is dissipated by friction with the pipe/bend walls. Fig. 35 also shows the velocity vectors at the bend inlet. Visible from the velocity magnitude is that the insert increases the air velocity in the core flow due to the rotational flow created by the insert. Another important result directly affecting erosion is the mixing promoted between the fluid in

the core flow region and the near wall regions. This has important consequences on the particle motion, as will be shown in the next sections, especially if the effects of coupling between the gas and the particles is taken into account. Figure 36 shows the streamlines for the clean air flow. As expected, a well-defined, swirling flow is generated by the insert, that moves down-stream of the elbow.

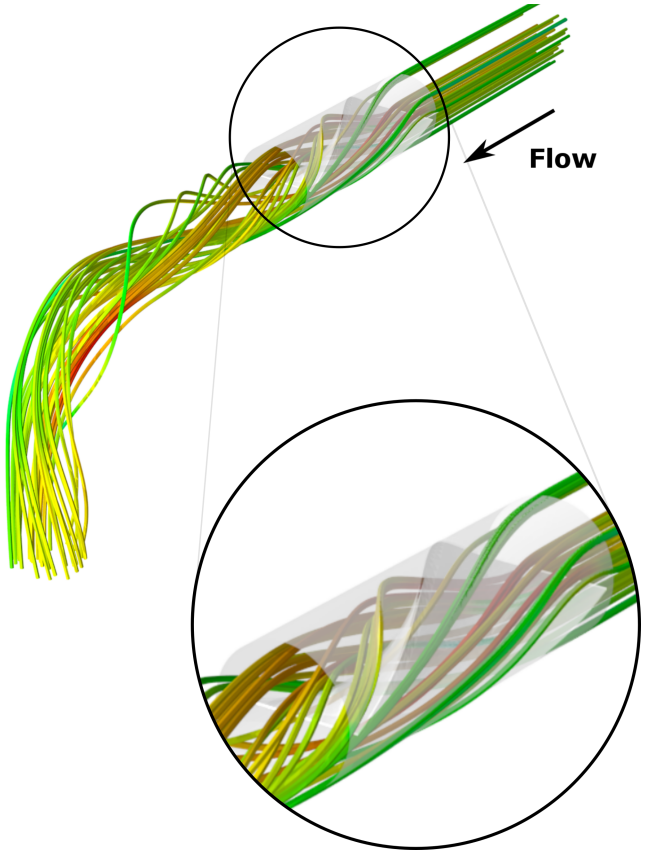

Figure 36 – Streamlines of the velocity field with twisted tape insert.

The effect of the swirl generated by the tape on the particles can be observed in Fig. 37, in which both standard and tape-equipped-elbow are shown. By comparing the standard elbow (Fig. 37e) with the others (Figs. 37a, 37b, 37c, 37d), it is discernible that the disturbance generated in the flow creates a better distribution of the particles reaching the elbow wall, avoiding concentration in a single region. Regarding the position where the insert lies, it follows that the farther away the twisted tape is located, the longer the helical flow will affect the flow, causing mixing between the core flow and near wall regions. A distinct change in the particle path is visible during the impact with the twisted-tape. The twisted tape force the particles towards the wall so there is a greater concentration of particles downstream of the tape insert. The difference generated by the effect mentioned above can be better visualized by the particle flow before the shock against the insertion in Fig. 37a compared to Fig. 37e, where the concentration is visually the same. On the other hand, after the impact with the twisted tape Figs. 37b, 37c, 37d represent the effect previously mentioned, according to which particles tend to accumulate close to

the pipe walls. Noticeably, the insert homogenizes the particle distribution upstream and downstream of the main impact region. In the latter, the redistribution effect triggered by the twisted-tape causes the erosion to decrease, as will be shown later in the next section.

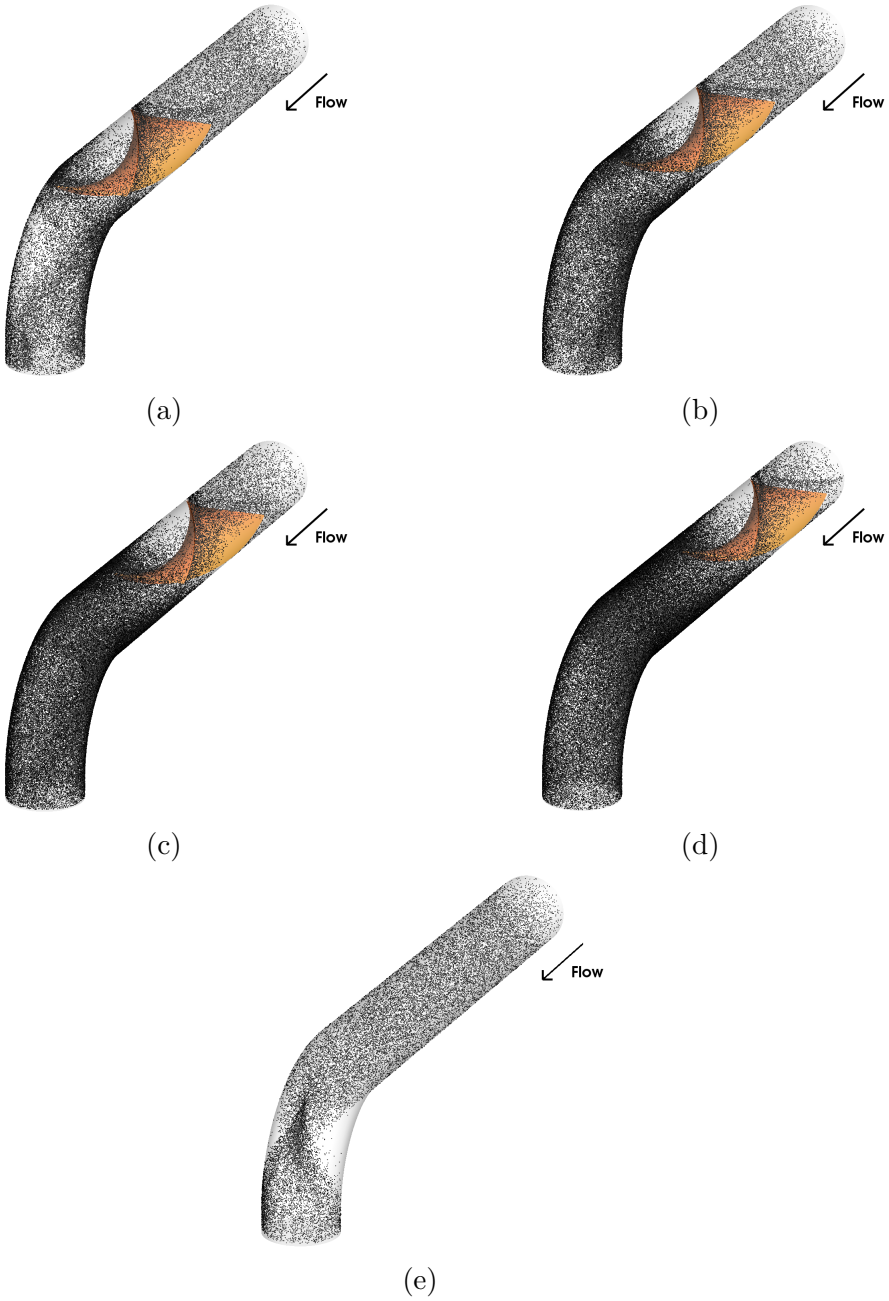

Figure 37 – Particle dynamics for one-way coupling at all positions: (a) 0D; (b) 1D; (c) 2D; (d) 3D and (d) standard elbow.

7.3 Effects of tape position - one-way coupling

In order to have an insight on the mechanisms for erosion reduction brought about by the twisted tape, a first investigation was carried out. The purpose is to find an optimal position for the insert inside the pipe that minimizes the elbow erosion. As a

quantitative measure of the elbow erosion, the penetration ratio was calculated. This study was accomplished disregarding the interaction between the gas and the particles.

Figure 38 shows the contours of penetration ratio. It is possible to realize that the maximum value is almost the same in all cases, although the extent of the eroded regions appears to be more limited with the insert at position 3D. This is more evident from Fig. 39, which shows the penetration ratio along the elbow symmetry line for the standard elbow and all the insert positions investigated. The most important finding is that, with reference to the standard elbow, the penetration is considerably decreased for all insert positions. Despite the complex trends and the many differences among all positions studied, insert position 3D apparently generates lower penetration for most of the elbow curvature.

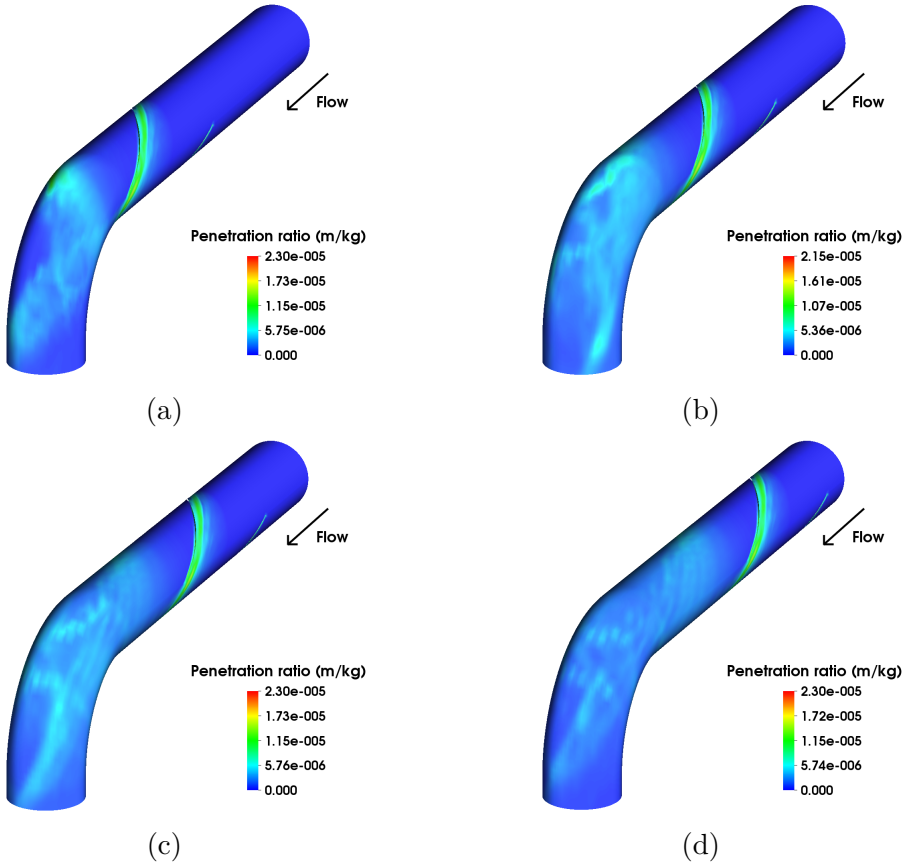

Figure 38 – Penetration ratio for one-way coupling at all insert positions: (a) 0D; (b) 1D; (c) 2D and (d) 3D.

The inclusion of the twisted tape causes important modifications to the erosion patterns observed for the standard elbow, as can be observed by comparing Fig. 27 and Fig. 38. The maximum penetration region is no longer focused on a spot in the bend, but rather it is spiral-shaped in the upstream pipeline. Furthermore, the penetration is reduced for all tape positions, which suggests the potential of such devices. Typically, the standard elbow will fail because of repetitive particle collisions at the same point. With

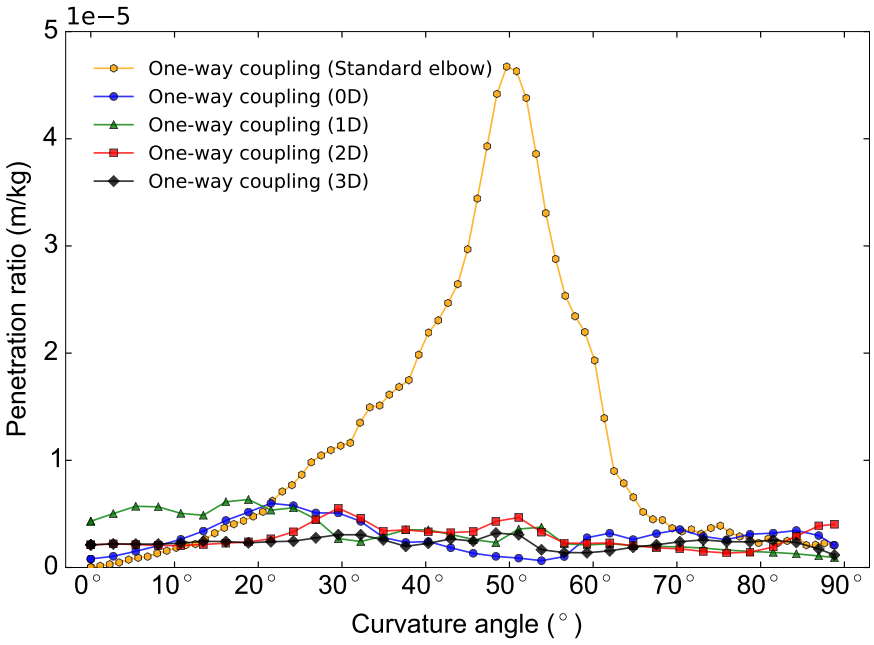

Figure 39 – Penetration ratio versus curvature angle for one-way coupling at all positions.

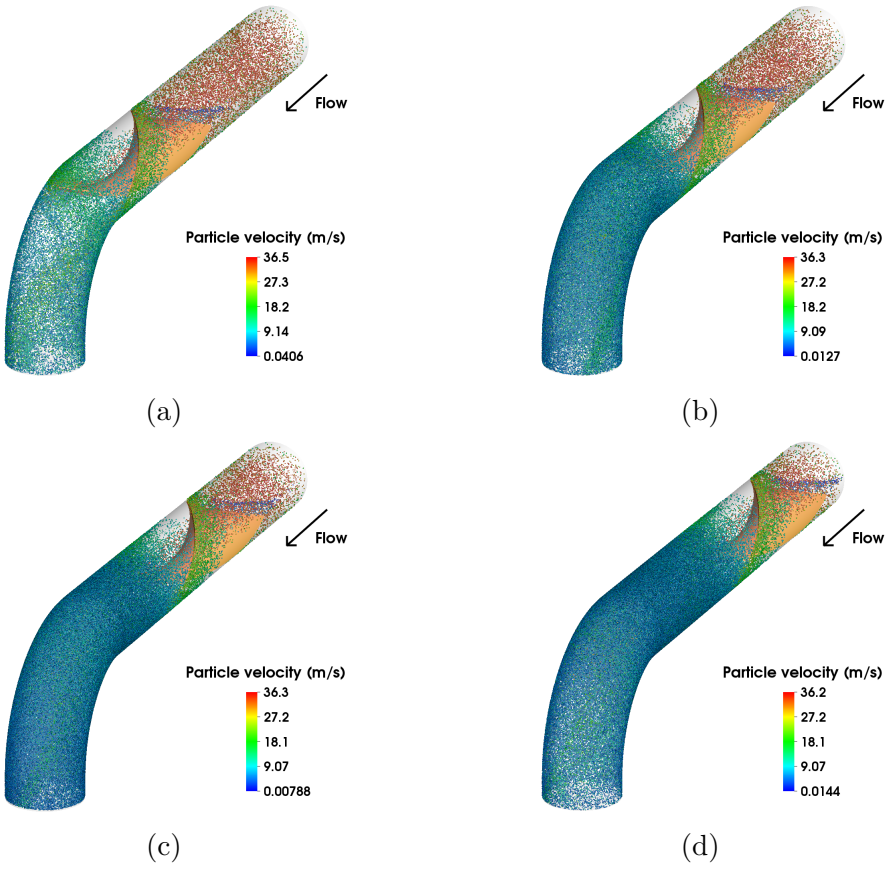

Figure 40 – Particle velocity one-way coupling for all positions: : (a) 0D; (b) 1D; (c) 2D and (d) 3D.

the insertion of the twisted tape, the bend life can be extended considerably, as indicate by the penetration ratio values in Fig. 39.

Such a change in the erosion patterns can be explained based on the particle mechanics. In the standard elbow, the particles flow from the inlet of the pipeline, develop a parabolic-like profile and collide directly against the bend walls. Typically, because of the particle velocity profile, the main collision region is focused on a point on the bend wall, as shown in Fig. 37e. As the twisted tape is inserted in the upstream pipeline, the particles first collide against the tape, lose momentum, as shown in Fig. 40, and acquire a swirling motion. This, in turn, causes the patterns displayed in Fig. 38. The erosion contours are more widespread on the bend wall, sparing it from the more severe damage as would occur otherwise.

7.3.1 Particle erosion mechanisms

As previously mentioned, for a given pair of materials, the penetration ratio can be explained in terms of particle impact velocity, impact angle and wall collision frequency. In the following sections, such variables and their role in the penetration patterns for the elbow with the spiral insert are assessed.

7.3.1.1 Impact velocity

Figure 41 shows the contours of the impact velocity at the different insert positions. It is possible to notice that, as the twisted tape is positioned closer to the domain inlet, the impact velocity on the elbow surface gradually decreases, even though the maximum velocity for all cases are very close. Since the particles primarily slam into the twisted tape, it is expected that the impact velocity in the elbow will decrease considerably when compared to the standard elbow. The differences observed for each position can be explained by the helical flow created by the insert. However, when the fluid leaves the twisted tape and the insert is located near the elbow, as shown in Fig. 41a, the particles directly hit the bend wall, resulting in a higher impact velocity in this region. The profiles presented in Fig. 42 confirm this behavior. In any event, the impact velocities are considerably lower than those for the standard elbow, which contributes to reduce the erosion rate in the elbow.

7.3.1.2 Impact angle

Regarding the impact angle, a similar trend for the insert position is observed in Figs. 43 and 44. Because the differences are rather small, it is assumed that this parameter has a secondary importance in explaining the erosion patterns, mainly considering that the model employed in this work does not take into account the deformation and possible changes in the geometry of each particle caused by the particle to the bend wall. To the best of the authors' knowledge, none of the currently used erosion models can accommodate

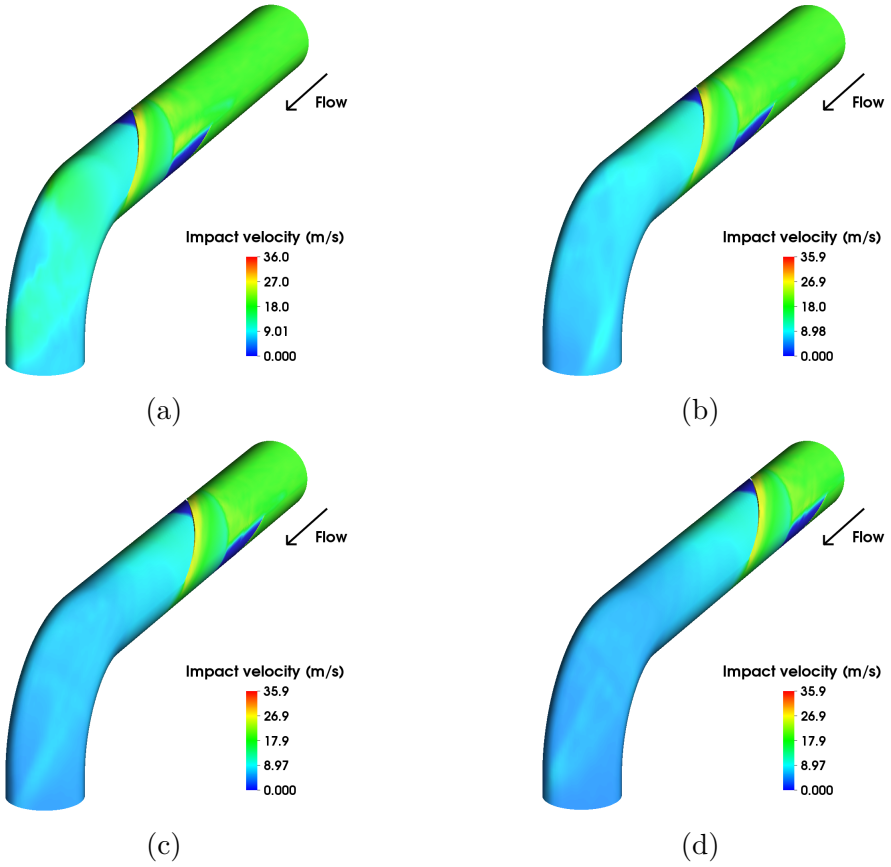

Figure 41 – Impact velocity for one-way coupling at all insert positions: (a) 0D; (b) 1D; (c) 2D and (d) 3D.

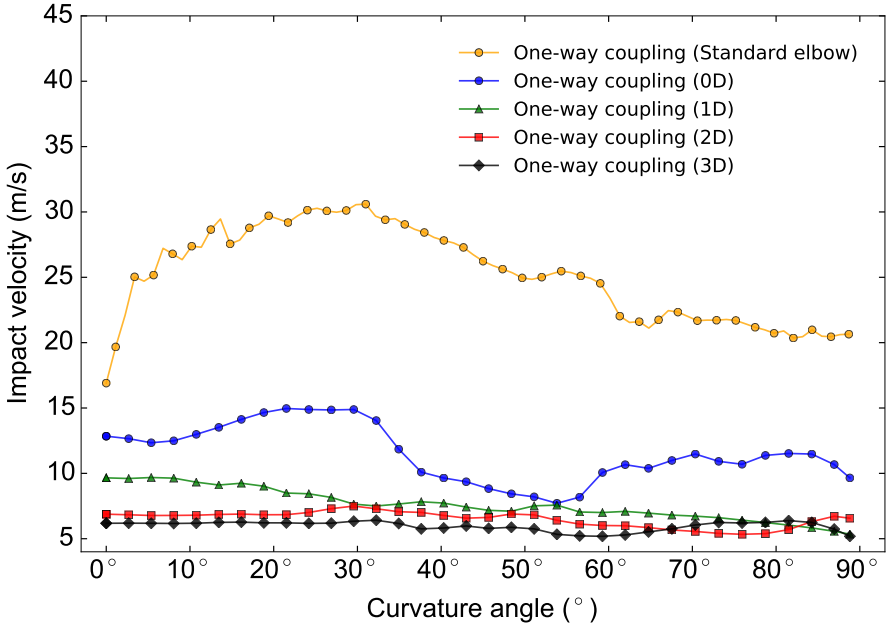

Figure 42 – Impact velocity versus curvature angle for one-way coupling at all positions.

such geometry changes. Again, the magnitudes are lower than those observed for the standard elbow.

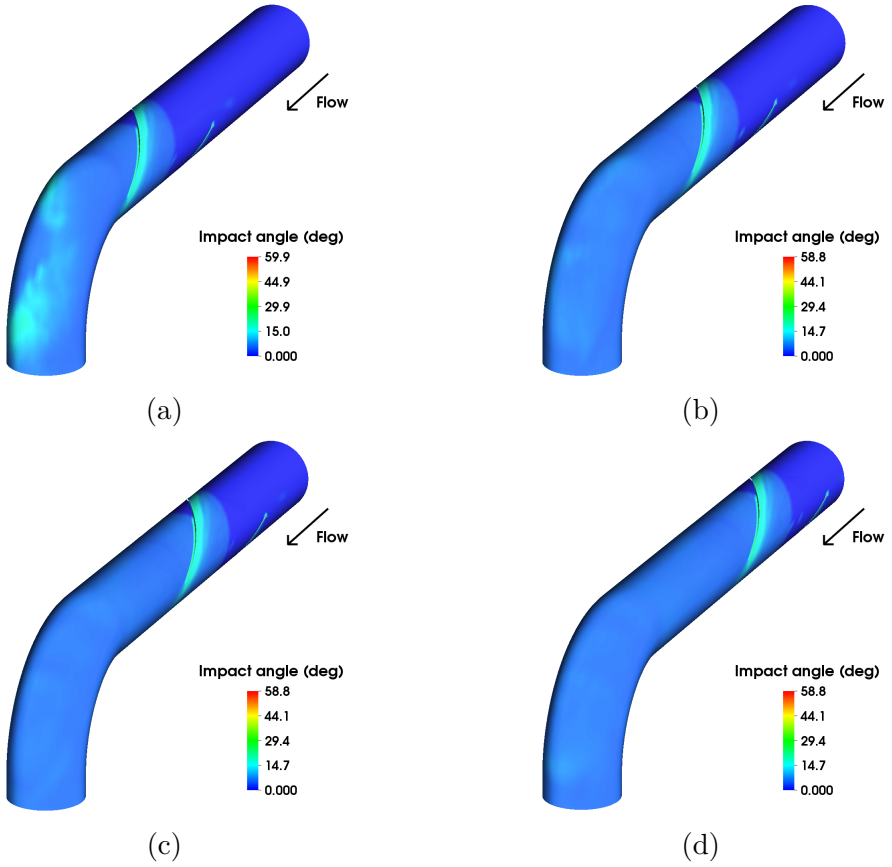

Figure 43 – Impact angle for for one-way coupling at all insert positions: (a) 0D; (b) 1D; (c) 2D and (d) 3D.

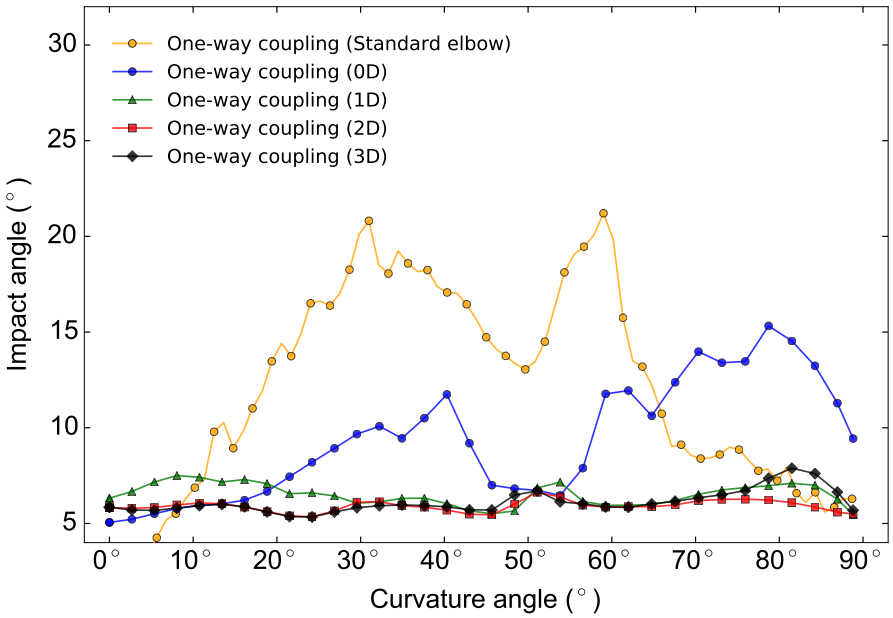

Figure 44 – Impact angle versus curvature angle for one-way coupling at all positions.

7.3.1.3 Impact frequency

Figure 45 displays the contours of the particle-to-wall impact frequency for insert positions 0D (Fig. 45a), 1D (Fig. 45b), 2D (Fig. 45c) and 3D (Fig. 45d), respectively. The insert position is seen to remarkably modify the impact frequency patterns. In contrast to the effects on impact velocity and impact angle, the tape position increases the maximum wall collision frequency as it is placed farther away from the elbow. This is due to the swirl decay, which causes the particles to move away from the inlet pipe walls. The particles, in turn, tend to recover the original parabolic velocity profile. Thus it is expected that the contours tend to approach those observed for the standard elbow. When referring to elbow erosion, this is obviously undesirable, since more collisions imply on more erosion. This leads to the conclusion that there is an upper limit for the tape position to be beneficial. Interestingly, position 3D was again found to be potentially the best place for the insert, as can be verified in Fig. 46. This suggests that, although the elbow collision frequency was increased regarding the standard elbow for most of the bend curvature, its effect was overwhelmed by the reduction in the impact velocity, resulting in a net decrease in the penetration ratio. It is important to bear in mind that the penetration ratio varies with a power of the impact velocity, therefore this variable is expected to be the most influential on the phenomenon

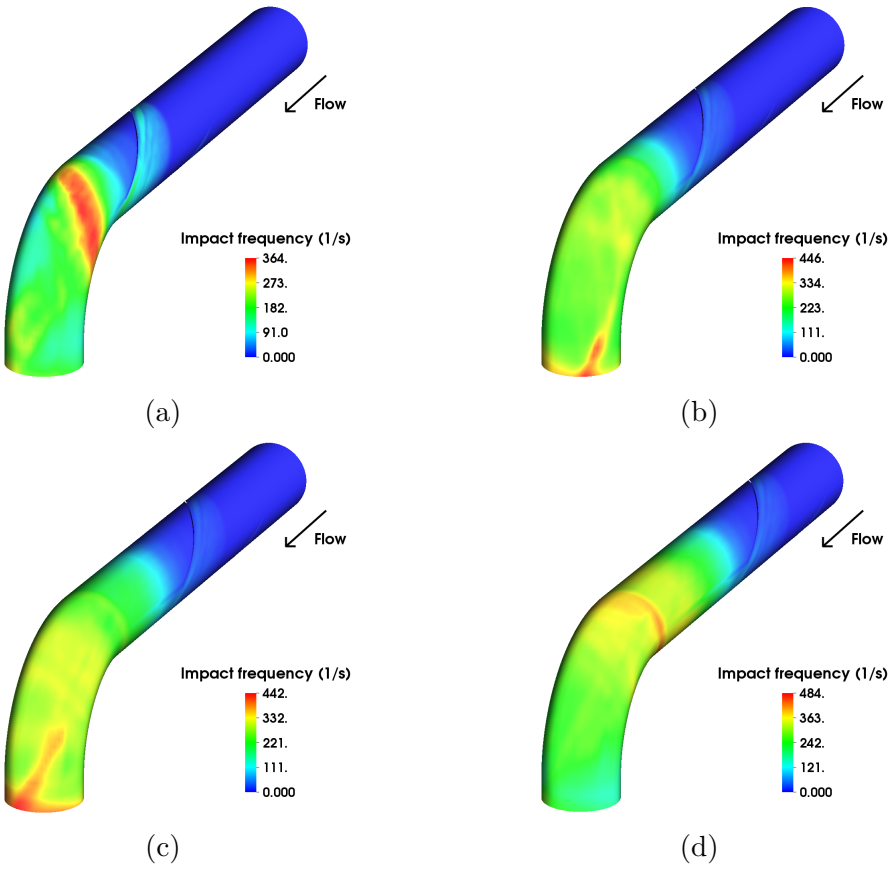

Figure 45 – Impact frequency for one-way coupling at all insert positions: (a) 0D; (b) 1D; (c) 2D and (d) 3D.

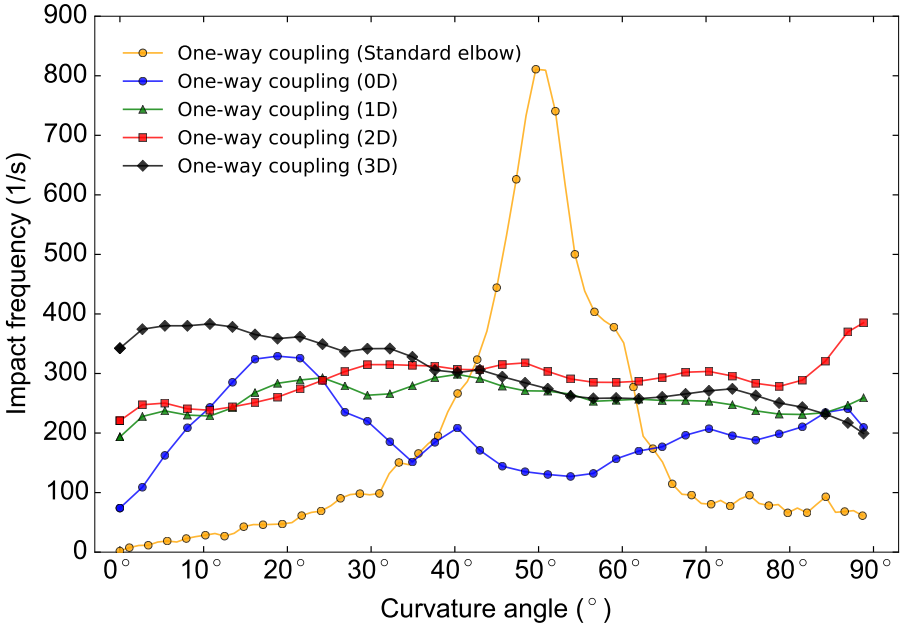

Figure 46 – Impact frequency versus curvature angle for one-way coupling at all positions.

Up to this point, all analyses were done disregarding interactions between the carrier fluid and the particles, as well as interparticle collisions. Although these were shown not to be relevant in the case of the standard elbow at the same mass loading, they turn out to be crucial when locally high particle concentration regions exist, such as with the twisted tape insert. This has been explored in previous publications by Duarte et al. (DUARTE et al., 2015; DUARTE et al., 2016a). In the next sections, these effects are investigated for the twisted tape placed 3D upstream of the bend, which was found to be the best position among those studied.

7.4 Phase interaction effects

In this section the effects of the gas and particle interactions are taken into account for the twisted tape inserted 3 pipe diameters away from the bend. Figure 47 shows the contours of the penetration ratio for one and four-way couplings. Although the maximum penetration ratio is higher with interparticle collisions (Figs. 47c, 47d), the damaged areas are apparently reduced when compared to the one-way calculation. This reduction can be seen more clearly in Fig. 48, in which the profiles evidence the reduction in elbow erosion brought about by the interactions between the carrier fluid and the particles and interparticle collisions. Another important finding is related to the standard elbow. When comparing Fig. 27c and Fig. 47c, both for four-way simulations, it is noticed that the insertion of the tape brings a decrease of an order of magnitude in the penetration ratio. Unlike the regular elbow, for which the effects of two and four-way couplings were negligible, the twisted-tape-equipped elbow results are highly sensitive to such phase

interactions. This is a consequence of the flow pattern, which induces locally high particle concentration regions.

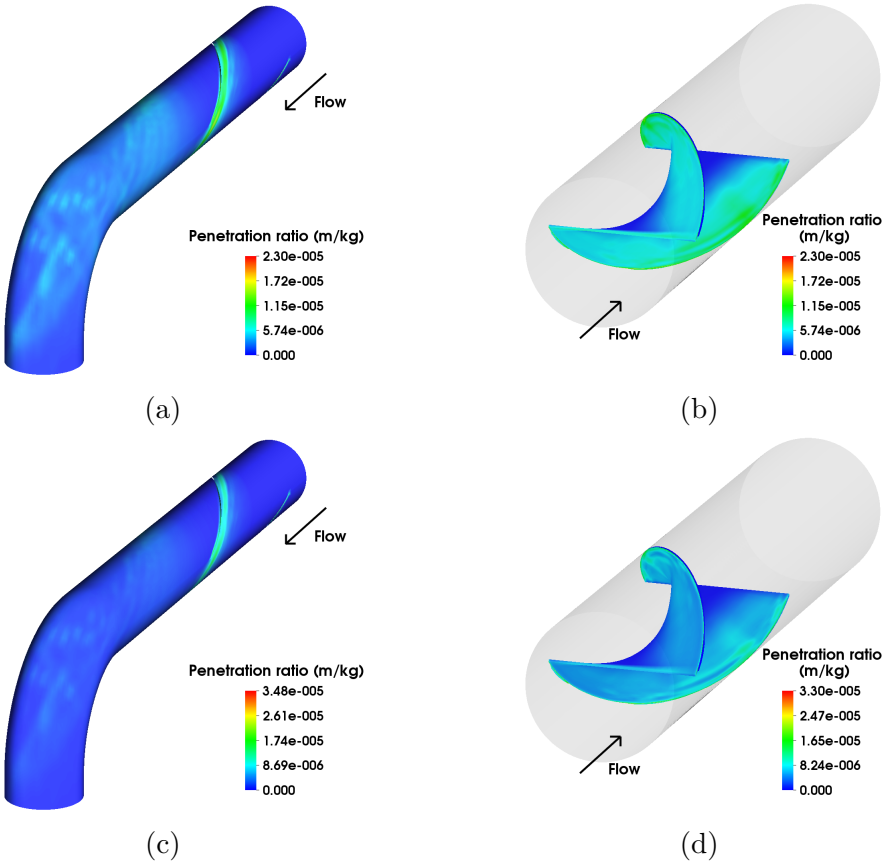

Figure 47 – Penetration ratio for the insert at 3D with isolated twisted tape for each case: (a) and (b) One-way coupling; (c) and (d) Four-way coupling.

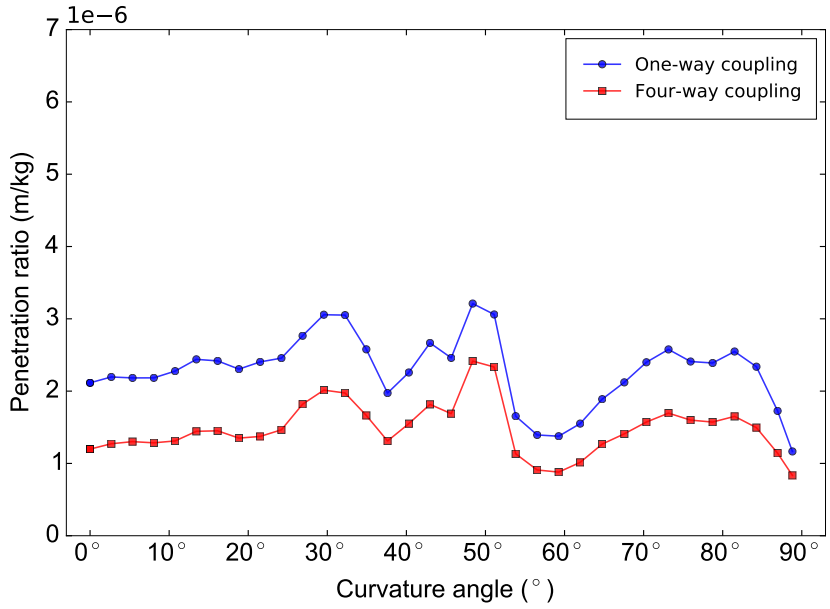

Figure 48 – Penetration ratio versus curvature angle for the twisted tape at 3D.

It can also be noticed that the particle-to-particle collisions appear to enhance the damage observed in one-way calculations. In addition, in both one and four-way calculations, considerable penetration is observed in the twisted tapes (Fig. 47b, 47d), although the peak value is not found in the insert, but rather in the pipeline upstream of the bend. In order to explain these findings, the variables affecting erosion, namely impact frequency, impact velocity and impact angle are analyzed again in the next sections.

7.4.1 Particle erosion mechanisms

7.4.1.1 Impact frequency

As far as the impact frequency is concerned, the contours shown in Fig. 50 for one and four-way couplings display remarkable differences for both the elbow and the twisted tape. By comparing Fig. 50a and Fig. 50c, it is noticeable that there is a reduction in the maximum value of the particle-to-wall impact frequency and also the particle spreading caused by the helical flow when particle-to-particle collisions are included in the model. The same logic applies to the inserts (Fig. 50b and Fig. 50d). Figure 49 shows the profile of the impact frequency in the elbow, evidencing the higher values for the one-way case. When compared to the standard elbow, Fig. 31c and Fig. 50c show the dispersion of the impact frequency when the twisted tape is used. Essentially, the particles no longer hit the same spot and the penetration ratio is consequently reduced, as shown in Fig.48. Also, the highest value for this variable in the standard elbow is over twice that of the inserted elbow.

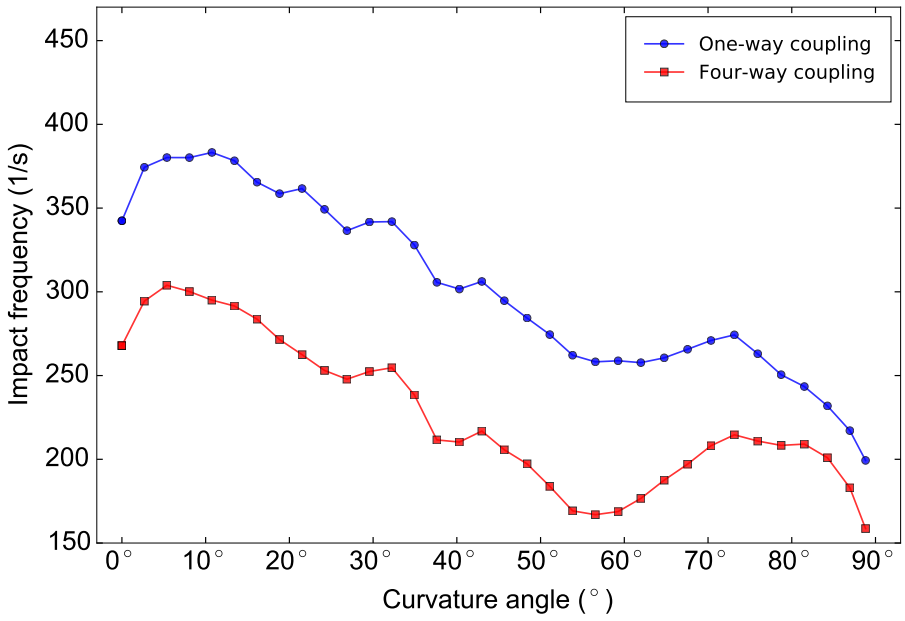

Figure 49 – Impact frequency versus curvature angle for the twisted tape at 3D.

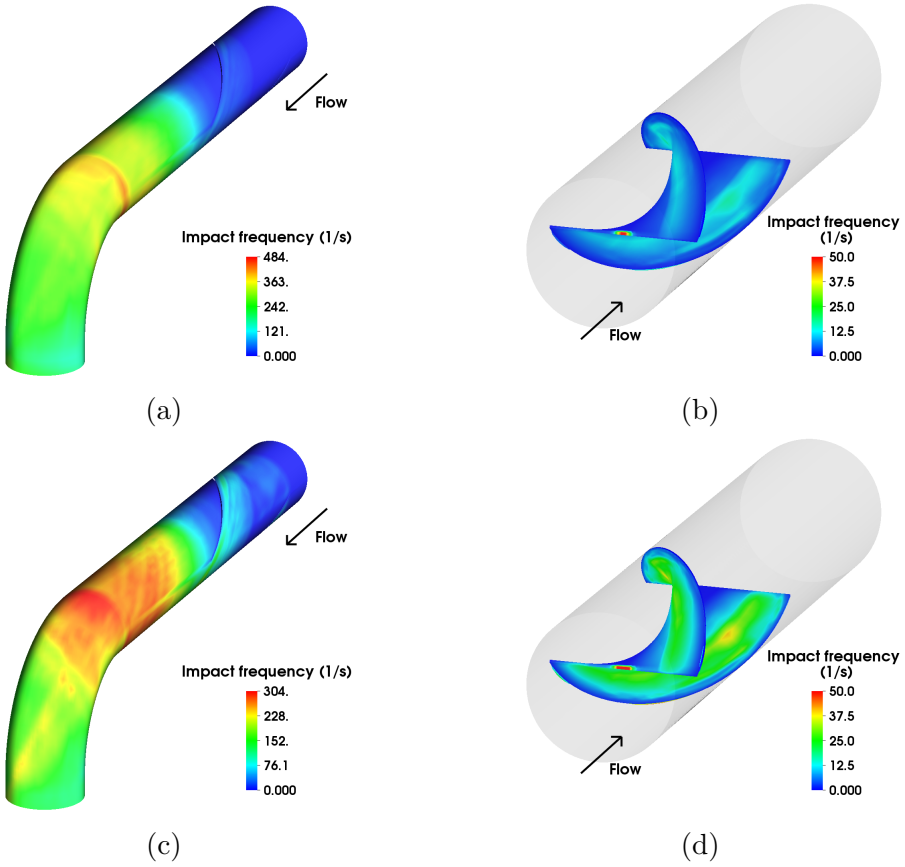

Figure 50 – Impact frequency for the insert at 3D with isolated twisted tape for each case: (a) and (b) One-way coupling; (c) and (d) Four-way coupling.

7.4.1.2 Impact velocity

Regarding the impact velocity of the particles against the pipeline walls, Fig. 51 demonstrates that the maximum velocity for both one and four-way couplings are nearly the same, although the particles are better distributed along the pipe cross-section in the four-way case.

Nevertheless, when inter-particle collisions are considered, the overall impact velocity in the elbow is seen to increase (Fig. 51c). This is confirmed by the profiles in Fig. 52. This is because particles leaving the tape transfer momentum to those next to the elbow, which in turn collide with higher energy against the elbow.

The comparison with the impact velocity for the standard elbow (Fig. 31c) reveals huge differences. For the standard elbow, the highest impact velocity is in the bend itself, whereas the highest velocities are achieved in the twisted tape body in the case of the inserted elbow, as shown in Fig. 51b and Fig. 51d.

This reduces the impact velocity in the elbow dramatically, even in the four-way calculation, with positive effects for the elbow erosion. The profiles of Fig. 32 and Fig. 52 show, respectively, that for the standard elbow the average impact velocity is about 22

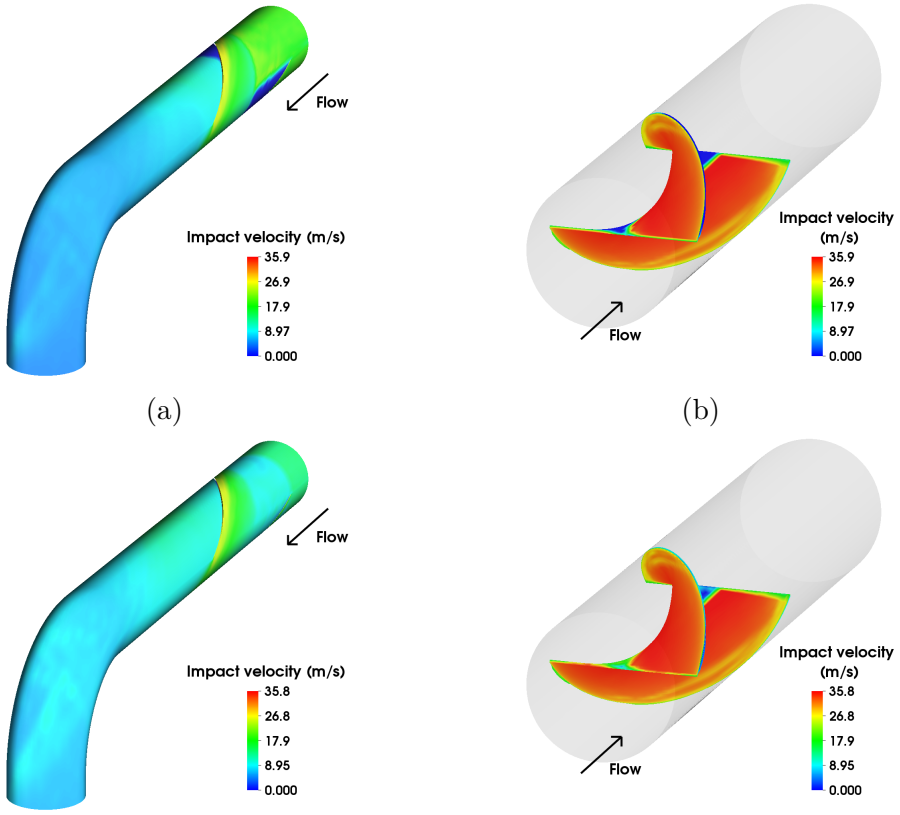

Figure 51 – Impact velocity for the insert at 3D with isolated twisted tape for each case: (a) and (b) One-way coupling; (c) and (d) Four-way coupling.

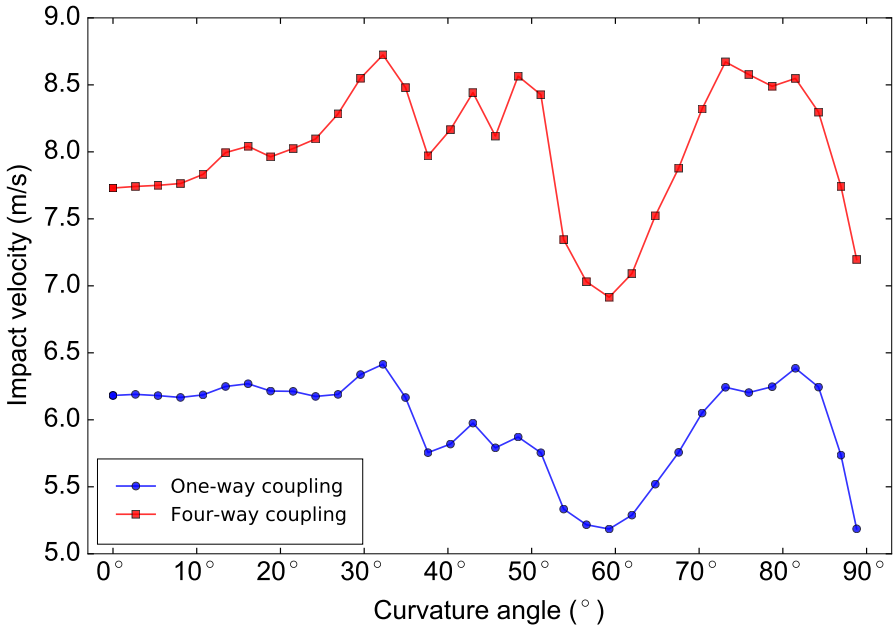

Figure 52 – Impact velocity versus curvature angle for the twisted tape at 3D.

m/s at the main impact region, while for the inserted elbow it is close to 7.5 m/s. Despite the apparent advantage of the twisted tape regarding elbow erosion, it should be born in

mind that the twisted tape itself becomes more prone to erosion. From a very pragmatic point of view, such a device could be regarded as a sacrificial element, particularly useful when the elbow lifetime is to be extended for whatever reasons.

7.4.1.3 Impact angle

The particle impact angle displays similar contours for one and four-way couplings, as Fig. 61a and Fig. 61c indicate. It is possible to observe that, when the interphase momentum exchange is active, there is an increase in the peak impact angle. Furthermore, this peak is located in the tape body, as shown in Fig. 61b and Fig. 61d. Again, the profiles shown in Fig. 54 confirm that the fluid-particle and particle-particle momentum exchange cause the impact angle to increase slightly along the bend curvature. In any event, the values are much lower than those calculated for the standard elbow, Fig. 33. As with the impact velocity, this might mean less elbow erosion for ductile materials.

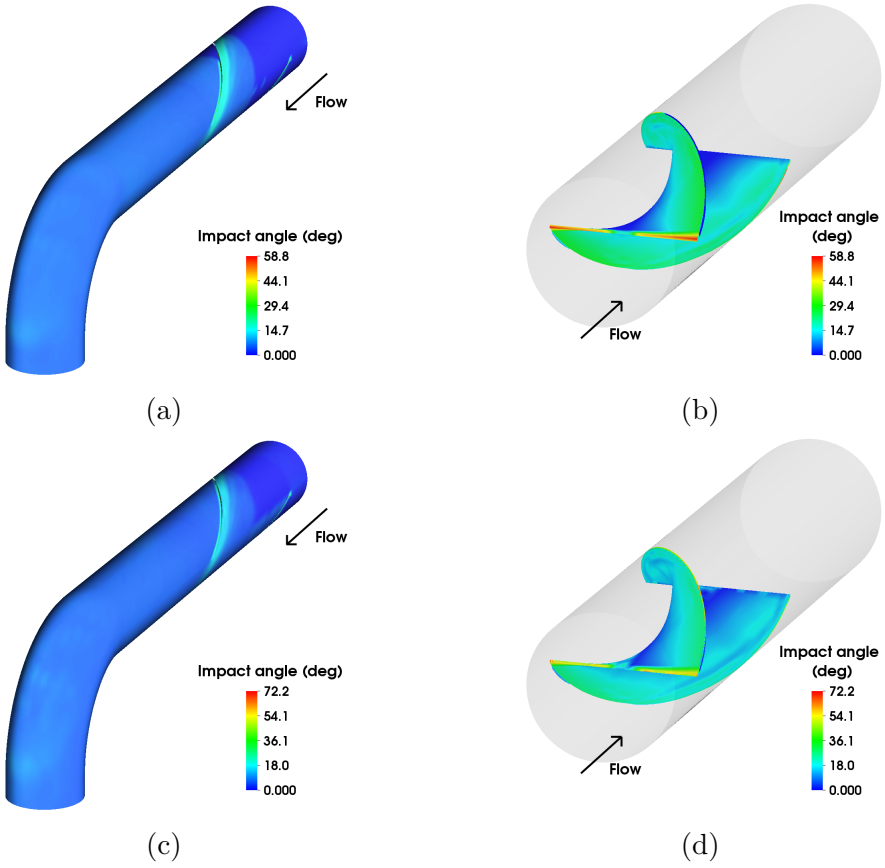

Figure 53 – Impact angle for the insert at 3D with isolated twisted tape for each case: (a) and (b) One-way coupling; (c) and (d) Four-way coupling.

7.4.2 Final considerations

As a summary of this section, it can be stated that the reduction in the penetration ratio brought about by the interphase momentum in the twisted tape case is likely due

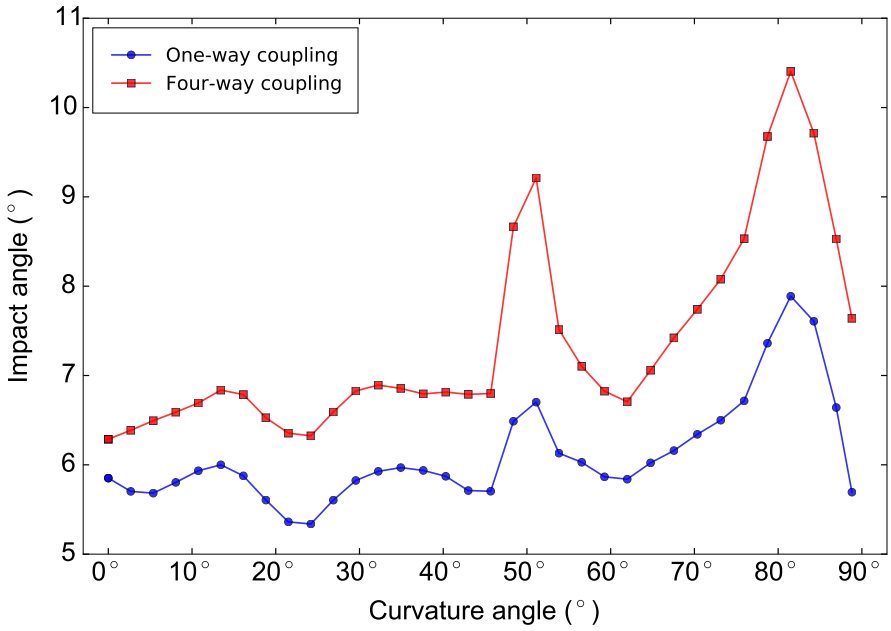

Figure 54 – Impact angle versus curvature angle for the twisted tape at 3D.

to the reduction in the particle-wall impact frequency, although the impact velocity was seen to increase. This phenomenon has already been reported by other researchers and is named "cushioning effect". Basically, particles adjacent to the elbow wall protect it against direct particle impact. Incoming particles shock against those in a film adjacent to the elbow surface, thereby reducing the wall impact frequency. This was observed in the works of Duarte et al. (DUARTE et al., 2015; DUARTE et al., 2016a). Interestingly, the advantages of the twisted tape are potentialized at higher mass loadings, since the cushioning effect will be enhanced because of the more frequent inter-particle collisions.

Although the erosion ratio is most sensitive to the impact velocity, the major role in explaining the penetration patterns is played by the impact frequency, as the results demonstrate. From a practical point of view, the twisted tape might serve as a sacrificial component made of a material more resistant to erosion than the pipe, and therefore, it must be replaceable in order to be useful. One should bear in mind that this is not necessarily an issue, as it is cheaper and easier to install/uninstall the tape in a removable piping section than replace the eroded elbow. The pipeline flow does not necessarily have to be interrupted, as a bypass system, parallel to the tape section can be used.

The numerical results show that particle velocity drops downstream of the tape. However, the fluid velocity will not change and, as demonstrated by Laín and Sommerfeld (LAÍN; SOMMERFELD, 2013) for a rough pipe, the consequence is an additional the system pressure drop to re-accelerate and convey the slower particles. Therefore, there will be a penalty in terms of energy consumption in order to spare the elbow and still convey the particles.

8 Conclusions

The effects of a twisted tape placed at different upstream positions of a bend were investigated numerically. The models used in the simulations were previously validated based on experiments for a standard bend. It has been found that, because of the swirl imparted by the twisted tape, particles will be more uniformly distributed in the flow. This in turn reduces the focusing effect, as observed for the regular bend, thus attenuating the direct collisions against the same spot in the bend wall. Furthermore, the interphase momentum exchange enhances such effect by shielding the elbow surface from direct particle impacts. Thus bend lifetime can be extended, since the damage is more distributed and the penetration ratio along the bend curvature is decreased.

Based on the simulation findings, it can be concluded that even at low mass loadings, the effects of inter-particle collisions on the the variables affecting erosion cannot be disregarded, especially if the flow pattern is complex. It is noteworthy that regarding the particle mechanisms, the impact velocity and impact frequency are the most important parameters affecting the penetration ratio.

Since many industrial processes require the transportation of particle-laden fluid streams, the twisted-tape inserted elbow appears to be an interesting alternative. Its efficiency was observed to grow as the insertion is placed far from the elbow entrance. Notwithstanding, the twisted tape itself can be seen as a sacrificial element, as it will be damaged by the particle collisions. The pipeline upstream of the bend will also be worn, but at a rather lower rate than the standard elbow, for instance.

As a result of the excellent agreement of the numerical computations obtained with the validation phase in combination with all required models for the erosion prediction, it may be concluded that the models presented here are capable for supporting the optimization and the design of pneumatic conveying systems. Furthermore, with the knowledge of the inter-particles collision effects it will be now also possible to predict erosion rates in the different pipe elements.

It is emphasized here that all the simulations presented in this work were made using the serial version of UNSCYFL. In this way, as an extension of the investigation done in this thesis considers the continuation of the study on pipelines, seeking a change in the elbow configuration. However, keeping the swirl effect created by the twisted tape.

Although the research objective is fulfilled, new interesting topics for future research have emerged. The subsequent chapter presents those topics.

9 Future research

In the current research it was only possible to study the erosion process isolated. Although the outcome was satisfying, some topics may be interesting for future research. These topics are listed below:

- change the elbows configuration;
- change fluid and particles properties;
- analyze erosion in others geometries;
- use different turbulence models, such as: RSM and LES.

Bibliography

AHLERT, K. R. Effects of particle impingement angle and surface wetting on solid particle erosion of AISI 1018 Steel. 1994. Cited 2 times on pages 51 and 61.

ASTM International G40-13. Standard Terminology Relating to Wear and Erosion. *ASTM Book of Standards*, i, p. 1–9, 2014. Cited on page 26.

BARDINA, J. E.; FIELD, M.; HUANG, P. G.; COAKLEY, T. J. Turbulence Modeling Validation , Testing , and Development. *Nasa Technical Memorandum*, n. April, 1997. Cited on page 43.

BAYER, R. G. Fundamentals of Wear Failures. In: *ASM Handbook Volume 11, Failure Analysis and Prevention (ASM International)*. [S.l.: s.n.], 2002. p. 901 – 905 (5). Cited on page 26.

BHUIYA, M. M. K.; CHOWDHURY, M. S. U.; SHAHABUDDIN, M.; SAHA, M.; MEMON, L. A. Thermal characteristics in a heat exchanger tube fitted with triple twisted tape inserts. *International Communications in Heat and Mass Transfer*, v. 48, p. 124–132, 2013. ISSN 07351933. Cited on page 38.

BHUSHAN, B. *Introduction to tribology*. [S.l.: s.n.], 2013. ISBN 1118403223. Cited 5 times on pages 13, 29, 30, 31, and 32.

BREUER, M.; ALLETTO, M.; LANGFELDT, F. Sandgrain roughness model for rough walls within Eulerian–Lagrangian predictions of turbulent flows. *International Journal of Multiphase Flow*, v. 43, p. 157–175, jul 2012. ISSN 03019322. Cited on page 48.

C. Crowe, E. Michaelides, J. S. *Multiphase flow handbook*. [S.l.]: Mechanical and Aerospace Engineering Series, 2005. Cited on page 47.

CHEN, X.; MCLAURY, B. S.; SHIRAZI, S. A. Numerical and experimental investigation of the relative erosion severity between plugged tees and elbows in dilute gas/solid two-phase flow. *Wear*, v. 261, n. 7-8, p. 715–729, oct 2006. ISSN 00431648. Cited on page 67.

CROOK. *Practical guide to wear for corrosion engineers*. [S.l.: s.n.], 1991. 64–66 p. Cited on page 26.

CROWE, C. T.; SOMMERFELD, M.; TSUJI, Y. Multiphase Flows with Droplets and Particles. *CRC Press New York*, p. 191–222, 1998. Cited on page 47.

De Souza, F. J.; SILVA, A. L.; UTZIG, J. Four-way coupled simulations of the gas-particle flow in a diffuser. *Powder Technology*, v. 253, p. 496–508, 2014. ISSN 00325910. Cited on page 42.

De Souza, F. J. D.; SALVO, R. D. V.; ALVES, D.; MARTINS, D. M. Large Eddy Simulation of the gas – particle flow in cyclone separators. v. 94, p. 61–70, 2012. Cited 2 times on pages 42 and 45.

DENNIS, B. S. C. R. The steady flow due to a rotating sphere at low and moderate Reynolds numbers. v. 101, 1980. Cited on page 47.

DESHPANDE, N. S.; BARIGOU, M. Flow of gas-liquid foams through pipe fittings. *International Journal of Heat and Fluid Flow*, v. 22, n. 1, p. 94–101, 2001. ISSN 0142727X. Cited on page 37.

DUARTE, C. A. R.; SOUZA, F. J. de; SANTOS, V. F. dos. Numerical investigation of mass loading effects on elbow erosion. *Powder Technology*, v. 283, p. 593–606, 2015. ISSN 00325910. Cited 5 times on pages 41, 51, 73, 87, and 93.

DUARTE, C. A. R.; SOUZA, F. J. de; SANTOS, V. F. dos. Effects of surface roughness and interparticle collisions on elbow erosion. In: *ICMF-2016 – 9th International Conference on Multiphase Flow*. [S.l.: s.n.], 2016. p. 1–6. Cited 4 times on pages 41, 68, 87, and 93.

DUARTE, C. A. R.; SOUZA, F. J. de; SANTOS, V. F. dos. Mitigating elbow erosion with a vortex chamber. *Powder Technology*, v. 288, p. 6–25, 2016. ISSN 1873328X. Cited on page 41.

ELGHOBASHI, S. On predicting particle-laden turbulent flows. *Applied Scientific Research*, Kluwer Academic Publishers, v. 52, n. 4, p. 309–329, 1993. ISSN 0003-6994. Cited 2 times on pages 13 and 63.

EYLER, R. L. Design and Analysis of a Pneumatic Flow Loop. 1987. Cited on page 67.

FERZIGER, J. H.; PERIC, M. *Computational methods for fluid dynamics*. [S.l.]: Springer, 2002. Cited 5 times on pages 55, 57, 59, 60, and 61.

FINNIE, I. Erosion of surfaces by solid particles. *Wear*, v. 3, n. 2, p. 87–103, 1960. ISSN 00431648. Cited on page 76.

FORDER, A.; THEW, M.; HARRISON, D. A numerical investigation of solid particle erosion experienced within oilfield control valves. *Wear*, v. 216, n. 2, p. 184–193, 1998. ISSN 00431648. Disponível em: <http://www.sciencedirect.com/science/article/pii/S0043164897002172>. Cited 2 times on pages 54 and 61.

FROHLICH, J.; TERZI, D. von. Hybrid LES/RANS methods for the simulation of turbulent flows. *Progress in Aerospace Sciences*, v. 44, n. 5, p. 349–377, 2008. ISSN 03760421. Disponível em: <http://dx.doi.org/10.1016/j.paerosci.2008.05.001>. Cited 2 times on pages 13 and 43.

GAHR, K. Z. *Microstructure and Wear of Materials*. [s.n.], 1987. v. 10. v–vi p. ISSN 01678922. ISBN 9780444427540. Disponível em: <http://www.sciencedirect.com/science/article/pii/S0167892208707181>. Cited 4 times on pages 13, 29, 30, and 31.

GRANT, G.; TABAKOFF, W. Erosion Prediction in Turbomachinery Resulting from Environmental Solid Particles. *Journal of Aircraft*, v. 12, n. 5, p. 471–478, 1975. ISSN 0021-8669, 1533-3868. Cited 5 times on pages 51, 53, 54, 61, and 71.

GUIDE, F. *Fluent 6.2 User Guide*. Centerra Resource Park, 10 Cavendish Court, Lebanon, NH 03766, USA, 2005. Cited on page 55.

HASELBACHER, A.; NAJJAR, F. M.; FERRY, J. P. An efficient and robust particle-localization algorithm for unstructured grids. *Journal of Computational Physics*, v. 225, n. 2, p. 2198–2213, 2007. ISSN 00219991. Cited 2 times on pages 49 and 66.

HUMPHREY, J. A. C. Fundamentals of fluid motion in erosion by solid particle impact. *International Journal of Heat and Fluid Flow*, v. 11, n. 3, p. 170–195, 1990. ISSN 0142727X. Cited 2 times on pages 13 and 35.

HUTCHINGS, I. *Triblology: Friction and wear of engineering materials*. [S.l.: s.n.], 1992. 273 p. ISBN 0849377641, 9780849377648. Cited 2 times on pages 29 and 31.

IONESCU, D. Reduction of pipe wall erosion by creating a vortex flow in anthracite powder pneumatic transport for power plants. 2012. Cited on page 38.

KADYIROV, A. Numerical Investigation of Swirl Flow in Curved Tube with Various Curvature Ratio. p. 1–4, 2013. Cited on page 38.

KANIZAWA, F. T.; MOGAJI, T. S.; RIBATSKI, G. A new model for flow boiling heat transfer coefficient inside horizontal tubes with twisted-tape inserts. *International Journal of Refrigeration*, v. 61, p. 55–68, 2016. ISSN 01407007. Cited on page 38.

LAÍN, S.; SOMMERFELD, M. Numerical calculation of pneumatic conveying in horizontal channels and pipes: Detailed analysis of conveying behaviour. *International Journal of Multiphase Flow*, v. 39, p. 105–120, mar 2012. ISSN 03019322. Disponível em: <http://www.sciencedirect.com/science/article/pii/S0301932211002060>. Cited on page 64.

LAÍN, S.; SOMMERFELD, M. Characterisation of pneumatic conveying systems using the Euler/Lagrange approach. *Powder Technology*, v. 235, n. 0, p. 764–782, 2013. ISSN 0032-5910. Cited 4 times on pages 13, 64, 65, and 93.

LEVEQUE, R. J. Finite-volume methods for non-linear elasticity in heterogeneous media. *International Journal for Numerical Methods in Fluids*, John Wiley & Sons, Ltd., v. 40, n. 1-2, p. 93–104, 2002. ISSN 1097-0363. Cited on page 56.

LUN, C. K. K.; LIU, H. Numerical Simulation of Dilute Turbulent Cas-Solid Flows in Horizontal Channels. *Int. J. Multiphase Flow*, v. 23, n. 3, p. 575–605, 1997. Cited on page 47.

MALISKA, C. R. *Transferência De Calor E Mecânica Dos Fluidos Computacional*. [S.l.: s.n.], 2004. Cited on page 56.

MATHUR, S. R.; MURTHY, J. Y. A pressure-based method for unstructured meshes. *Numerical Heat Transfer, Part B: Fundamentals*, v. 31, n. 2, p. 195–215, 1997. Cited 2 times on pages 55 and 59.

MAZUMDER, Q. H.; SHIRAZI, S. a.; MCLAURY, B. Experimental Investigation of the Location of Maximum Erosive Wear Damage in Elbows. *Journal of Pressure Vessel Technology*, v. 130, n. 1, p. 011303, 2008. ISSN 00949930. Cited 2 times on pages 67 and 72.

MEI, R. An approximate expression for the shear lift force on a spherical particle at finite reynolds number. *International Journal of Multiphase Flow*, v. 18, n. 1, p. 145–147, jan 1992. ISSN 03019322. Cited on page 46.

MILLS, D. *Pneumatic conveying design guide*. [S.l.]: Butterworth-Heinemann, 2003. Cited 2 times on pages 26 and 38.

NEILSON, J. H.; GILCHRIST, A. Erosion by a stream of solid particles. *Wear*, v. 11, n. 2, p. 111–122, 1968. ISSN 0043-1648. Cited 2 times on pages 51 and 61.

OESTERLE, B.; PETITJEAN, A. Simulation of particle-to-particle interactions in gas solid flows. *International Journal of Multiphase Flow*, v. 19, n. 1, p. 199–211, 1993. ISSN 03019322. Cited on page 48.

OKA, Y.; OKAMURA, K.; YOSHIDA, T. Practical estimation of erosion damage caused by solid particle impact. *Wear*, v. 259, n. 1-6, p. 95–101, 2005. ISSN 00431648. Cited 4 times on pages 17, 51, 52, and 53.

OKA, Y. I.; OKAMURA, K.; YOSHIDA, T. Practical estimation of erosion damage caused by solid particle impact: Part 1: Effects of impact parameters on a predictive equation. *Wear*, v. 259, n. 1–6, p. 95–101, 2005. ISSN 0043-1648. Cited on page 51.

OKA, Y. I.; YOSHIDA, T. Practical estimation of erosion damage caused by solid particle impact: Part 2: Mechanical properties of materials directly associated with erosion damage. *Wear*, v. 259, n. 1-6, p. 102–109, 2005. ISSN 00431648. Cited 3 times on pages 51, 52, and 61.

PARISHER, R. A.; RHEA, R. A. *Pipe Drafting and Design*. Second edi. [s.n.], 2012. 79–111 p. ISBN 9780123847003. Disponível em: <http://www.sciencedirect.com/science/article/pii/B9780123847003000050>. Cited on page 36.

PATANKAR, S. *Numerical Heat Transfer and Fluid Flow*. [S.l.]: Taylor & Francis, 1980. (Series in computational methods in mechanics and thermal sciences). ISBN 9780891165224. Cited on page 60.

PENG, K.; SHUGUANG, Z.; JIANGHAO, W.; CHUNXIN, Y. An improved known vicinity algorithm based on geometry test for particle localization in arbitrary grid. *Journal of Computational Physics*, v. 228, n. 24, p. 9001–9019, 2009. ISSN 0021-9991. Cited on page 66.

PEREIRA, G. C.; SOUZA, F. J. de; de Moro Martins, D. A. Numerical prediction of the erosion due to particles in elbows. *Powder Technology*, v. 261, p. 105–117, 2014. ISSN 1873328X. Cited 4 times on pages 36, 41, 51, and 54.

RUBINOW, S. I.; KELLER, J. B. The transverse force on a spinning sphere moving in a viscous fluid. *Journal of Fluid Mechanics*, v. 11, n. 1955, p. 447, 1961. ISSN 0022-1120. Cited 2 times on pages 46 and 47.

SAFFMAN, P. G. The lift on a small sphere in a slow shear flow. *Journal of Fluid Mechanics*, v. 22, n. 02, p. 385, 1965. ISSN 0022-1120. Cited on page 46.

SANTOS, V. F. dos; SOUZA, F. J. de; DUARTE, C. A. R. Reducing bend erosion with a twisted tape insert. *Powder Technology*, 2016. ISSN 00325910. Disponível em: <http://linkinghub.elsevier.com/retrieve/pii/S0032591016304144>. Cited 2 times on pages 41 and 51.

SCHILLER, L.; NAUMANN, A. Z. A drag coefficient correlation. *VDI-Zeitschrifft 77*, p. 318–320, 1933. Cited on page 46.

SELMER-OLSEN, S. Medium pressure flow studies of particulated and concurrent annular gas/liquid flow with relevance to material loss in unprocessed hydrocarbon systems. In: *Third International Conference on Multiphase Flow*. [S.l.: s.n.], 1987. v. 253, p. 397–416. Cited on page 67.

SOLNORDAL, C. B.; WONG, C. Y.; BOULANGER, J. An experimental and numerical analysis of erosion caused by sand pneumatically conveyed through a standard pipe elbow. *Wear*, v. 336, p. 43–57, 2015. ISSN 00431648. Cited on page 68.

SOMMERFELD, M. Validation of a stochastic Lagrangian modelling approach for inter-particle collisions in homogeneous isotropic turbulence. *International Journal of Multiphase Flow*, v. 27, n. 10, p. 1829–1858, 2001. ISSN 03019322. Cited on page 48.

SOMMERFELD, M.; HUBER, N. Experimental analysis and modelling of particle-wall collisions. *International Journal of Multiphase Flow*, v. 25, p. 1457–1489, 1999. ISSN 0301-9322. Cited 2 times on pages 54 and 61.

STACHOWIAK, G. W.; BATCHELOR, A. W. *Engineering Tribology*. [s.n.], 2005. v. 10. 769 p. ISSN 1098-6596. ISBN 978-0-7506-7836-0. Disponível em: <http://books.google.de/books?id=otw4UKI631UC>. Cited 7 times on pages 13, 29, 30, 31, 32, 34, and 35.

TOBERGTE, D. R.; CURTIS, S. *No Title No Title*. 2013. 1689–1699 p. Disponível em: <http://www.whatispiping.com/piping-elbows-and-bends>. Cited on page 37.

TORO, E. F. *Riemann Solvers and Numerical Methods for Fluid Dynamics: A Practical Introduction*. [S.l.]: Springer, 2009. ISBN 9783540498346. Cited on page 56.

VERSTEEG, H. K.; MALALASEKERA, W. *An Introduction to Computational Fluid Dynamics: The Finite Volume Method*. [S.l.]: Pearson Education Limited, 2007. ISBN 9780131274983. Cited on page 56.

VIEIRA, R. E.; KESANA, N. R.; MCLAURY, B. S.; SHIRAZI, S. A.; TORRES, C. F.; SCHLEICHER, E.; HAMPEL, U. Experimental investigation of the effect of 90 standard elbow on horizontal gas-liquid stratified and annular flow characteristics using dual wire-mesh sensors. *Experimental Thermal and Fluid Science*, v. 59, p. 72–87, 2014. ISSN 08941777. Cited on page 38.

WOOD, R.; JONES, T.; MILES, N.; GANESHALINGAM, J. Upstream swirl-induction for reduction of erosion damage from slurries in pipeline bends. *Wear*, v. 250, n. 1-12, p. 770–778, oct 2001. ISSN 00431648. Cited on page 38.

ZHANG, C.; WANG, D.; REN, K.; HAN, Y.; ZHU, Y.; PENG, X.; DENG, J.; ZHANG, X. A comparative review of self-rotating and stationary twisted tape inserts in heat exchanger. *Renewable and Sustainable Energy Reviews*, v. 53, p. 433–449, 2016. ISSN 18790690. Cited 2 times on pages 38 and 51.

ZHANG, Y.; REUTERFORS, E.; MCLAURY, B.; SHIRAZI, S.; RYBICKI, E. Comparison of computed and measured particle velocities and erosion in water and air flows. *Wear*, v. 263, n. 1-6, p. 330–338, sep 2007. ISSN 00431648. Cited on page 61.

Appendix

APPENDIX A – Extra graphics

In relation to provide some additional data to help the reader better understand the results. The following graphics listed below were added.

1. Fig. 55, Penetration ratio versus curvature angle for one-way coupling at all twisted tape positions;
2. Fig. 56,Impact velocity versus curvature angle for one-way coupling at all twisted tape positions;
3. Fig. 57,Impact angle versus curvature angle for one-way coupling at all twisted tape positions;
4. Fig. 58,Impact frequency versus curvature angle for one-way coupling at all twisted tape positions;
5. Fig. 59,Particle concentration field along the curve with different cut planes for all twisted tape insert in positions (a) 0D; (b) 1D; (c) 2D and (d) 3D;
6. Fig. 60,Mass loss for four-way coupling at all insert positions: (a) 0D; (b) 1D; (c) 2D and (d) 3D;
7. Fig. 61,Mass loss for four-way coupling at isolated twisted tape for each case positions: (a) 0D; (b) 1D; (c) 2D and (d) 3D.

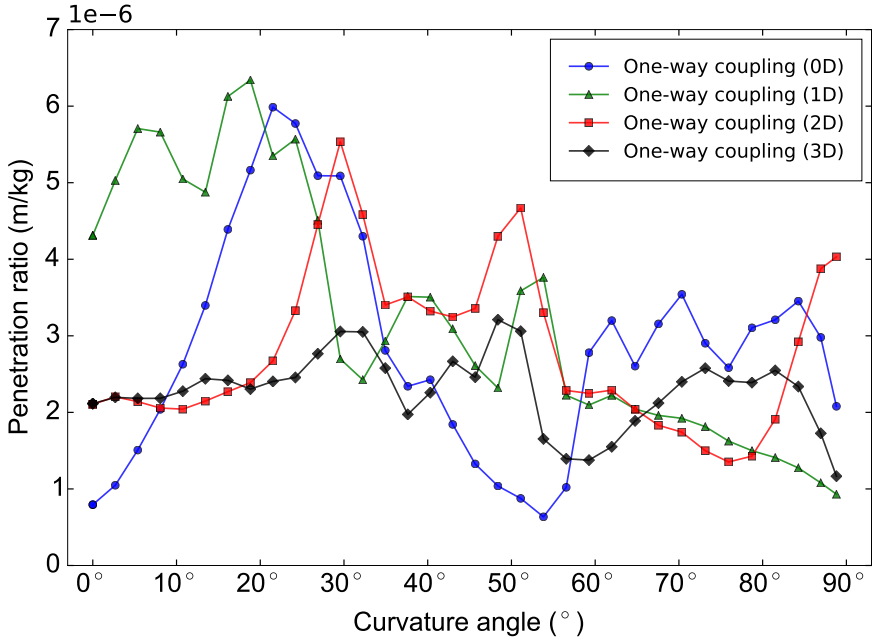

Figure 55 – Penetration ratio versus curvature angle for one-way coupling at all twisted tape positions.

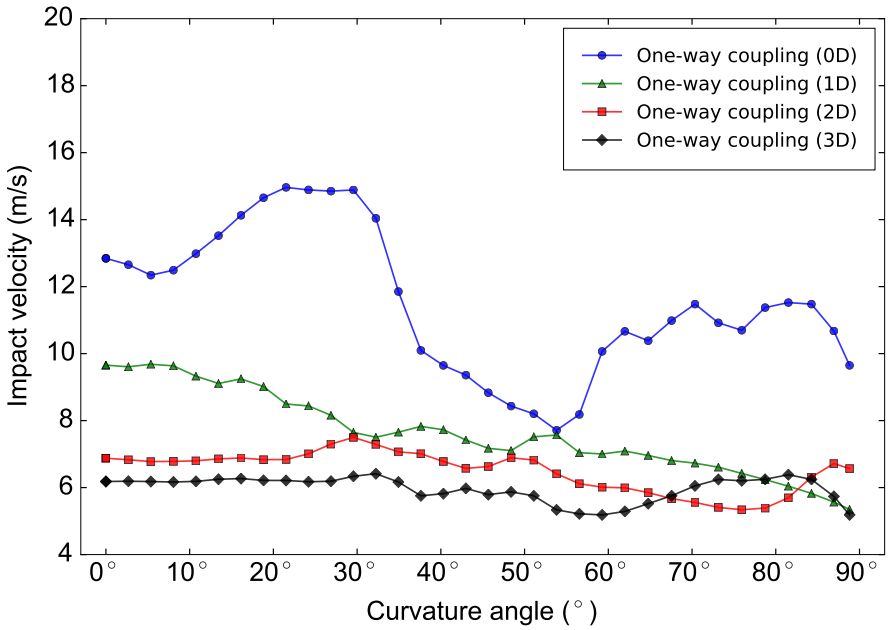

Figure 56 – Impact velocity versus curvature angle for one-way coupling at all twisted tape positions.

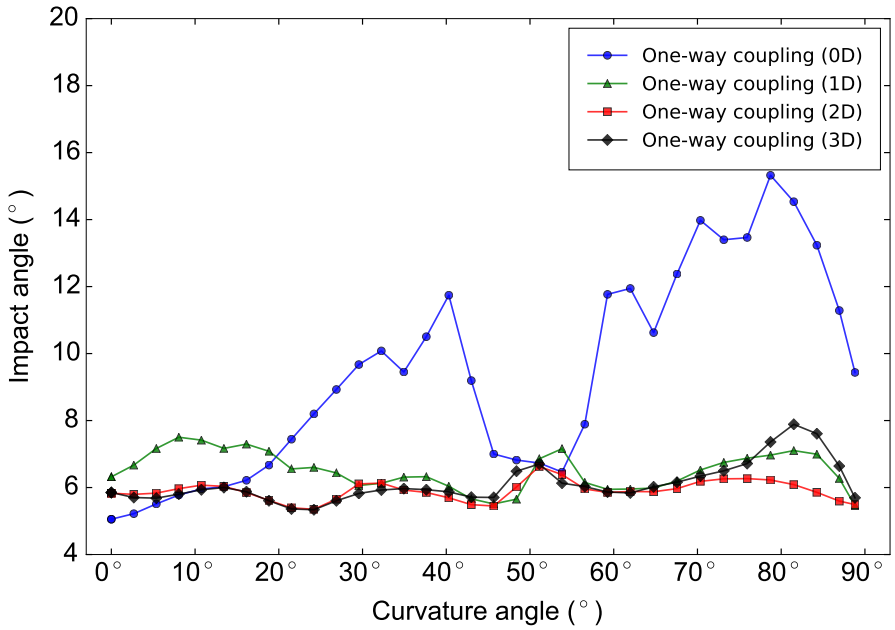

Figure 57 – Impact angle versus curvature angle for one-way coupling at all twisted tape positions.

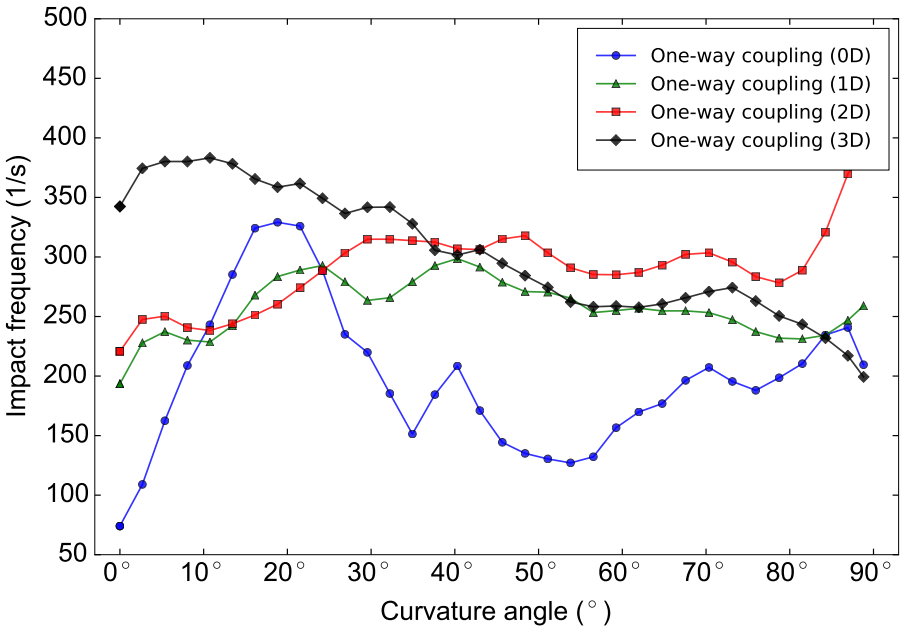

Figure 58 – Impact frequency versus curvature angle for one-way coupling at all twisted tape positions.

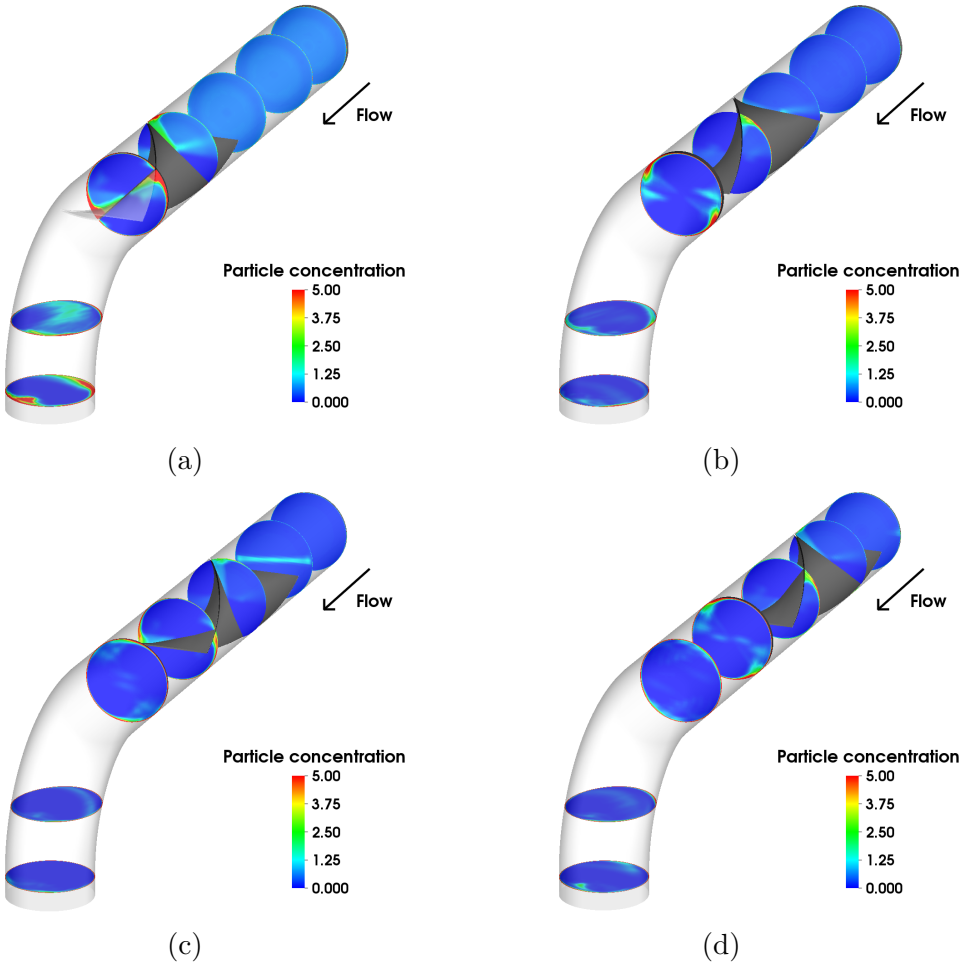

Figure 59 – Particle concentration field along the curve with different cut planes for all twisted tape insert in positions (a) 0D; (b) 1D; (c) 2D and (d) 3D.

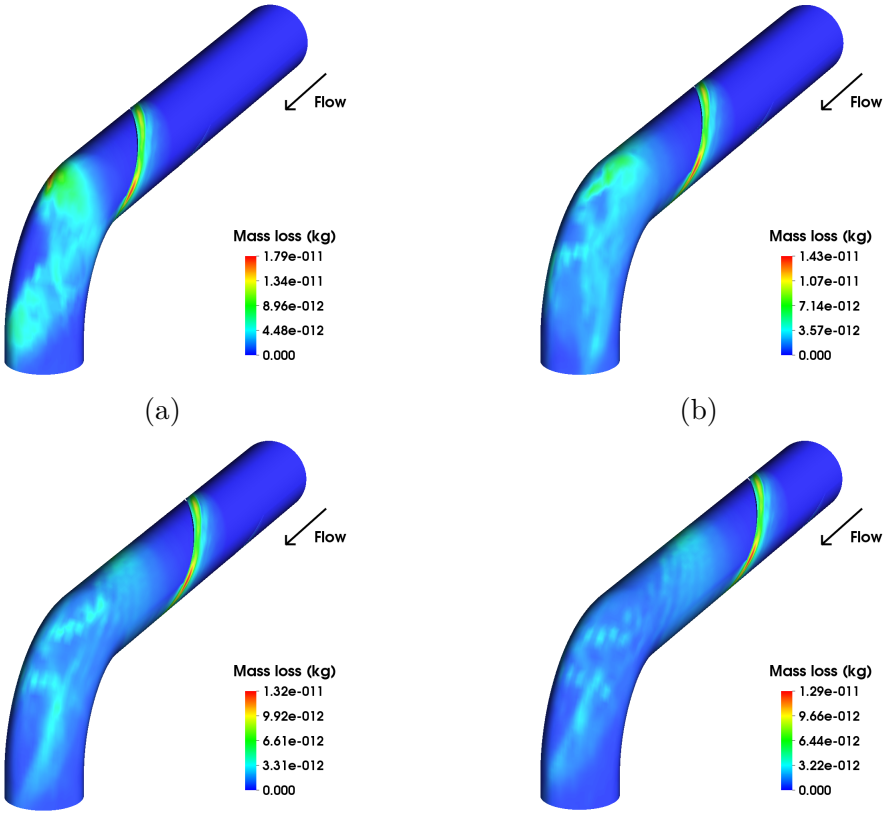

Figure 60 – Mass loss for four-way coupling at all insert positions: (a) 0D; (b) 1D; (c) 2D and (d) 3D.

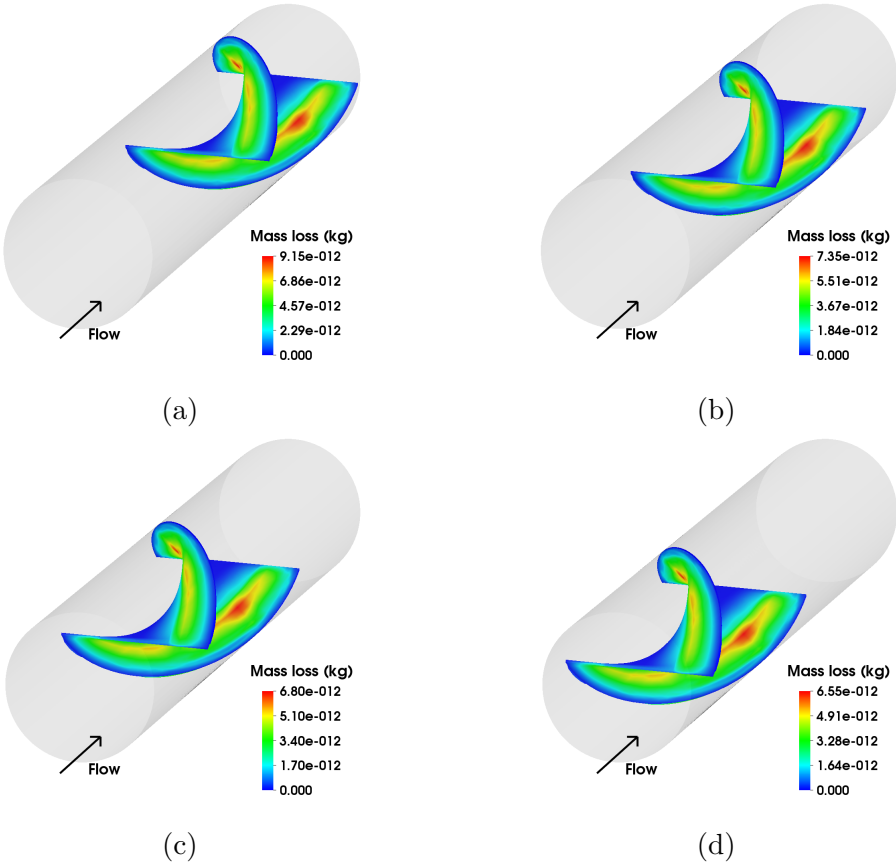

Figure 61 – Mass loss for four-way coupling at isolated twisted tape for each case positions: (a) 0D; (b) 1D; (c) 2D and (d) 3D.